Nanoscale

REVIEW

View Article Online
View Journal | View Issue

Cite this: *Nanoscale*, 2024, **16**, 21619

Photocatalytic applications of covalent organic frameworks: synthesis, characterization, and utility

Jared G. Doremus, Bertha Lotsi, Aadarsh Sharma and Psaras L. McGrier *

Received 3rd August 2024,
Accepted 19th October 2024

DOI: 10.1039/d4nr03204g

rsc.li/nanoscale

Photocatalysis has emerged as an energy efficient and safe method to perform organic transformations, and many semiconductors have been studied for use as photocatalysts. Covalent organic frameworks (COFs) are an established class of crystalline, porous materials constructed from organic units that are easily tunable. COFs importantly display semiconductor properties and respectable photoelectric behaviour, making them a strong prospect as photocatalysts. In this review, we summarize the design, synthetic methods, and characterization techniques for COFs. Strategies to boost photocatalytic performance are also discussed. Then the applications of COFs as photocatalysts in a variety of reactions are detailed. Finally, a summary, challenges, and future opportunities for the development of COFs as efficient photocatalysts are entailed.

1 Introduction

1.1 Principles of photocatalysis

Traditional synthetic methods can be costly, require high temperatures and harsh conditions, and need extensive workups. Thus, there has been a push to perform conventional reactions under more ambient and less energy-intensive means. One method to do this is photocatalysis and the use of light to drive chemical reactions. Total solar irradiation (TSI) provides an average annual solar radiation of 1361 W m^{-2}.[1] Although direct solar radiation at the Earth's surface is less due to absorption of sunlight by atmospheric gases and aerosols, this has the potential to power the world. Solar irradiation mainly has wavelengths around 300–2500 nm which includes ultraviolet (UV), visible, and near infrared (NIR) light. Markedly, solar irradiation is not evenly made up of UV, visible, and NIR light, and the actual composition is 7–8% UV, 42–44% visible, and 48–50% NIR light (Fig. 1).[1,2] This illustrates that there is a clear demand for photocatalysts with high visible and NIR light absorption.[3] Semiconductors are the most extensively studied materials for use as photocatalysts, especially metal-containing semiconductors. The most commonly used are TiO_2, ZnO, WO_3, CdS, $BiVO_4$, and Fe_2O_3; however, organic dyes are proposed as non-metal alternatives.[4]

Since there are discrepancies in the literature, it is important to define photocatalysis and photocatalysts. IUPAC's definition of photocatalysis is the "change in the rate of a chemical reaction or its initiation under the action of ultraviolet, visible or infrared radiation in the presence of a substance—the photocatalyst—that absorbs light and is involved in the chemical transformation of the reaction partners,"[5] and its definition of a photocatalyst is a "catalyst able to produce, upon absorption of light, chemical transformations of the reaction partners…".[5] Thus in a conventional definition of catalysis the thermodynamics is not changed but rather the kinetics through the creation of a new route. Therefore, if a material or substance uses light to drive a downhill thermodynamic process, it is a photocatalyst. On the other hand, when a material or substance uses light to facilitate uphill thermodynamic reactions the reaction should be called photosynthesis instead, and the material or substance is not a photocatalyst. The discrepancy arises from the fact that if the

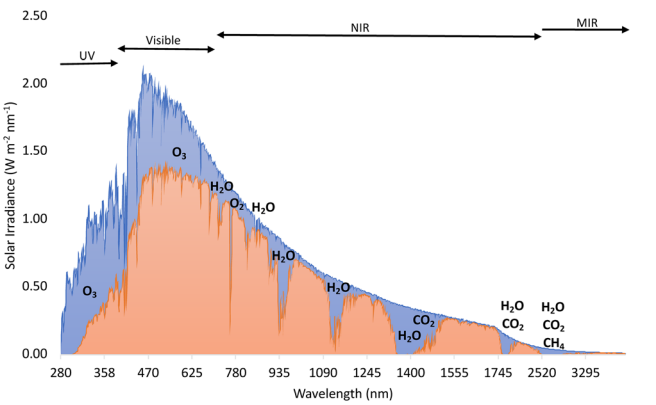

Fig. 1 Total solar irradiance (area in blue) and direct solar irradiance (area in orange) with gases shown that cause the difference between them.[2]

Department of Chemistry and Biochemistry, The Ohio State University, Columbus, Ohio 43210, USA. E-mail: mcgrier.1@osu.edu

photon is considered as a reactant, then the material or substance could be classified as a photocatalyst. Herein, we will use the broader definition of a photocatalyst that can drive either uphill or downhill thermodynamic processes.

Photocatalysis can broadly be depicted in four steps. (1) Light is absorbed. (2) Electron–hole pairs, or excitons, are generated, and the electron–hole pairs are separated by charge. (3) The separated electrons and holes move from the bulk material to the surface. (4) The charges on the surface participate in redox chemical reactions (Fig. 2). However, there are competing events that can occur that limit the photocatalytic process. Foremost, like any substance in an excited state, the photocatalyst can relax and return to the ground state after being excited by light. Due to coulombic interactions, recombination of the separated electrons and holes can occur either in the bulk material or at the surface. Recombination disperses the initial absorbed light energy by emitting heat (non-radiative) or light (radiative). Trapping of the charges in the bulk material can also occur and the trapping states have little to no reactivity, and the charges eventually hop trap-to-trap until they recombine. Notably, materials displaying high crystallinity, and thus few defects, can suppress recombination events as the charges can separate easier and have higher mobility.[6–8] Defect sites can trap electrons and holes and cause recombination. Smaller particle sizes and thickness can also limit recombination, as the charges have shorter distances and require less time to travel to the surface.[6–8]

In semiconductors, there is an energy gap between the valence band and conduction band, called the band gap, and this is crucial in photocatalytic applications (Fig. 3). When a photon has the energy equal to or greater than the band gap of the semiconductor, it will absorb the photon and become excited, which promotes an electron from the valence band to the conduction band and leaves a hole in the valence band, thus creating the electron–hole pair. Again, these electrons and holes participate in oxidation and reduction half reactions, and the potentials are derived from the valence band maximum and conduction band minimum, respectively. The conduction band potential of the photocatalyst must be lower, or more negative, than the potential of the substrate, and likewise the valence band potential must be higher, or more positive, than the substrate's potential. For example, in the reduction of N_2, at pH = 0 *versus* NHE, the conduction band of the photocatalyst needs to be below 0.55 V and the valence band of the photocatalyst needs to be above 1.33 V. In saying this, it is ideal for a photocatalyst to have low valence band and high conduction band potentials to increase the thermodynamic driving force. However, this leads to a large band gap and thus narrow light absorption. Therefore, there is a give-and-take relationship in creating optimal semiconductor photocatalysts.

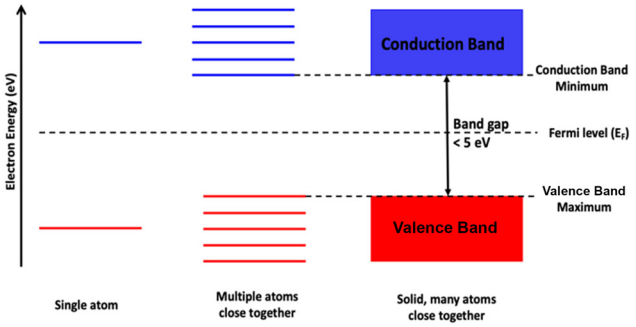

Fig. 3 Energy level and band diagram for semiconductors.

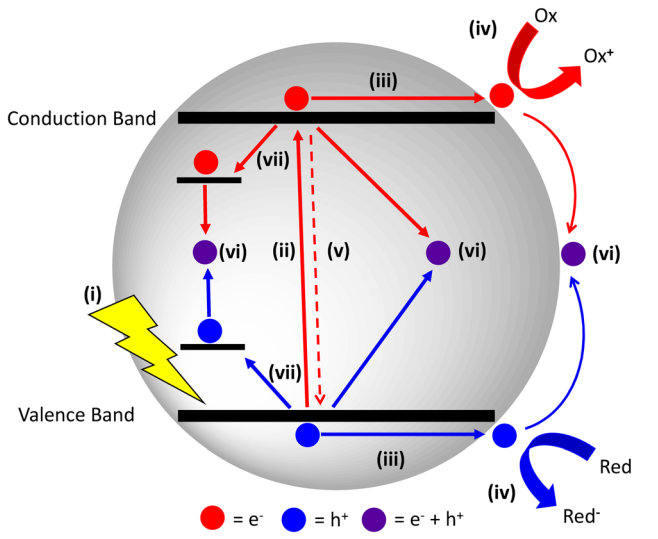

Fig. 2 Photocatalytic process in semiconductors. The (i) light absorption, (ii) generation and separation of electron–hole pairs, (iii) migration of electrons and holes to the surface of the semiconductor, (iv) redox reactions at the surface of the semiconductor, (v) relaxation of the excited electron and recombination with the hole, (vi) recombination of electron–hole pairs in the bulk or on the surface of the semiconductor, (vii) trapping of electrons and holes in the bulk semiconductor.

Photocatalytic activity has been defined in multiple ways in the literature. Experimentally, yields are typically measured by the moles of product per unit mass of photocatalyst per time, such as μmol g^{-1} h^{-1}, though other units can be seen as well, including μmol g^{-1} or μM h^{-1}. This way of defining photocatalytic activity makes it hard to compare various systems because of the difference in the power density and wavelength of light used, the use of any sacrificial reagents, the amount or moles of catalyst used, the overall reaction time, the pH of the solution, and other factors that affect photoactivity. A better method to determine photocatalytic activity is the quantum yield (QY).[9] This is the ratio of the number of electrons consumed in the reaction to the number of absorbed photons in a certain wavelength range. The drawback of this method is the lack of accuracy in determining the actual number of absorbed photons, especially in heterogeneous systems, as photons can scatter, reflect, and not be absorbed, and because of monochromaticity and other experimental design reasons. A way around this is by using only incident light, and this is termed the apparent quantum efficiency (AQE) or apparent quantum yield (AQY). AQY is the number of product molecules multi-

plied by the number of electrons consumed over the total number of incident photons. However, photon scattering still affects this measurement but to a lesser degree, and this method assumes light absorbed is the same in each experiment.[9] Notably, coloured reactants, intermediates, and products can skew these values.

1.2 Photophysical properties of conjugated polymers

Conjugated polymers have widely been used as semiconducting materials due to their photophysical properties.[10–12] π-Conjugated polymers have even been applied as photocatalysts as far back as 1985 by Yanagida *et al.* using poly(*p*-phenylene) for photocatalytic water splitting.[13] A significant reason conjugated polymers have been used as photocatalysts is their heterogeneous nature that allows for easy separation of them from the reaction mixture. Conjugated polymers also have limited photobleaching and avoid bimolecular encounters that homogeneous catalysts experience in solution. Moreover, conjugated polymers that are two-dimensional or three-dimensional display anisotropy, allowing for more tunable properties. For instance, the band gap of common semiconductors increases with decreasing layer thickness.[14] Comparatively to the aforementioned inorganic semiconductor photocatalysts, organic polymer photocatalysts have more tunable characteristics as the molecular backbone can be modified by varying the monomers, changing the ratio of monomers, or by adding functional groups. This affords conjugated polymers the capacity to alter their band gaps along with their photophysical properties and photocatalytic activity. Conjugated polymers with high molecular weights typically display higher photostability than homogeneous systems.[15,16] Even simple two-dimensional organic systems such as graphene, graphene oxide, and g-C_3N_4 are more diverse and tunable than traditional inorganic semiconductors. π-Conjugated polymers are commonly used in photocatalysis because they have wide-ranging light absorption so they can more readily absorb visible light and induce a π–π* transition to generate excitons.[13] Furthermore, these polymers are large π-conjugated systems with low electric resistivities, so charge carriers have high mobilities and protracted lifetimes, which leads to better photocatalytic performance.

1.3 Brief introduction to covalent organic frameworks

Covalent organic frameworks (COFs) are a class of crystalline, porous polymers.[17,18] COFs are constructed from organic building blocks linked through covalent bonds in dynamic and reversible processes through reticular chemistry. COFs feature low density, and good chemical, mechanical and thermal stability which make them a good platform for a myriad of applications.[19–21] Their bottom-up approach also allows for superior tunability and creation of designable structures, topology, morphology, pore shape and size, functionality, and more. Importantly for photocatalysis, COFs exhibit semiconductor behaviour and alterable band structure. COFs share the same advantages in photocatalysis as conjugated polymers as mentioned previously. The tunability of COFs allows for the incorporation of efficient light-absorbing units and certain moieties to increase their photocatalytic performance. A COF's crystallinity helps to create high charge carrier mobility and efficient charge separation of the excitons. Their high porosity enables good exposure to active sites, high diffusion rates, and convective mass transfer. The stability of COFs also provides resistance to photocorrosion, resulting in long photocatalytic lifetimes. Finally, their well-defined structures make it easier to study and understand the structure–property relationship and catalytic mechanism. This will be further discussed in the following sections.

1.4 Summary of review

COFs have been catapulted to the forefront as materials for photocatalytic applications in recent years, yet only a handful of reviews have been reported.[22–29] Since many of these reviews only discuss hydrogen evolution, water splitting, carbon dioxide reduction, or pollution degradation, we aim to present a comprehensive overview of COFs for photocatalysis with an emphasis on the most recent work that has been reported in the field. We begin by exploring the design, linkages, morphologies, and synthesis of COFs. This is followed by the characterization methods of COFs, especially ones pertaining to photocatalytic applications. A brief elucidation about techniques for photocatalytic product testing and mechanistic studies is conducted. The advantages of COFs towards photocatalysis and strategies to improve performance are examined. Lastly, the application of COFs as photocatalysts in a wide array of reactions is discussed along with the current weaknesses, future opportunities, and proposed areas for improvement.

2 COF design and synthesis methods

2.1 Engineering functional design of monomers

COFs are formed through the combination of symmetrical monomers linked by covalent bonds. COFs can be tailored and engineered for a variety of applications by varying the organic monomers and the linkages of the materials. Any conceivable COF can be synthesized using a variety of methods, and they can also be post-synthetically modified to alter their properties.

2.1.1 Monomer design. As their name may suggest, COFs are commonly designed with considerate discernment for the organic monomers being used. The COF building blocks frequently feature rigid monomers with π-backbones. The size of the monomers can also dictate pore size and volume by extending the length or adding substituents to the monomers. These monomer units can also be installed with functional groups to modify or improve the properties of the COF. Furthermore, the organic monomers can be devised to include substituents that can react with alcohols, azides, and terminal alkynes, which will be further discussed later in Section 2.2.9. More importantly, these building blocks are what provides the

COF with its base properties, allowing their utilization for many applications.

While covalent organic frameworks can be made from a plethora of exotic linkers, there are common archetypes. Typical organic linkers are based on benzene, biphenyl, triphenylamine, triphenylbenzene, triphenyltriazine, tetraphenylmethane, phenylethynylbenzene, pyrene, thiophene, porphyrin, and more (Fig. 4). There is also the ability to design the organic monomer to host a metal and incorporate it into the COF whether pre- or post-synthesis.[30] Common metal-binding ligands are based on bipyridine, phenanthroline, pyrazole, catecholate, porphyrin, phthalocyanine, N-heterocyclic carbene (NHC), salen, dehydrobenzoannulene, and triphenylphosphine (Fig. 5). Notably, there is a trade-off between commercial availability and synthetic cost *versus* complexity when designing and obtaining the building blocks.

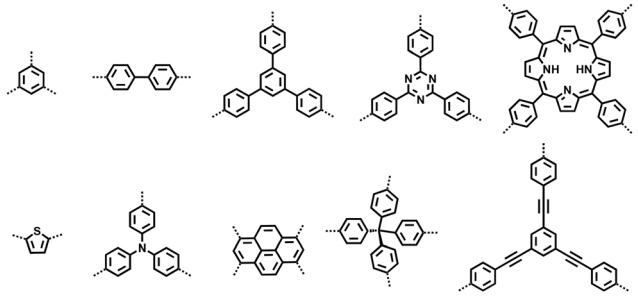

Fig. 4 Typical COF organic building motifs.

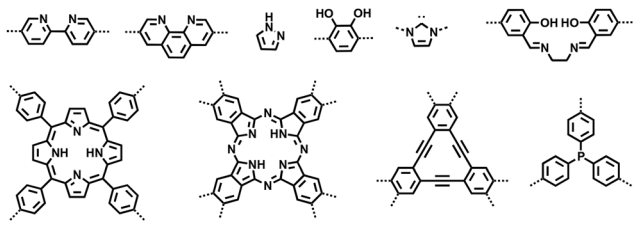

Fig. 5 Common COF units for metalation.

2.1.2 Linkage design. Just as covalent organic framework monomers can be designed, the linkage in which they form in the COF can likewise be formulated. The building blocks can possess boronic acids, diols, amines, and aldehydes among others to form a range of covalent bonds. The linkage formed behaves similarly to that in a small molecule regarding reactivity, stability, and other properties. Consequently, the COF will exhibit the same strengths and weaknesses similar to those of a small molecule analogue. Furthermore, COFs depend on reversible bond formation to fully realize crystallinity and porosity, but highly reversible reactions tend to form less stable bonds and thus a less stable COF.

The first reported COFs by Yaghi, including COF-1 and COF-5, were based on a boroxine and boronate ester linkage, respectively.[31] Other boron-based linkages include borosilicate,[32] borazine,[33] and spiroborate[34] (Fig. 6). These linkages are highly reversible in nature and result in highly crystalline COFs but suffer from instability in humid or protic conditions.

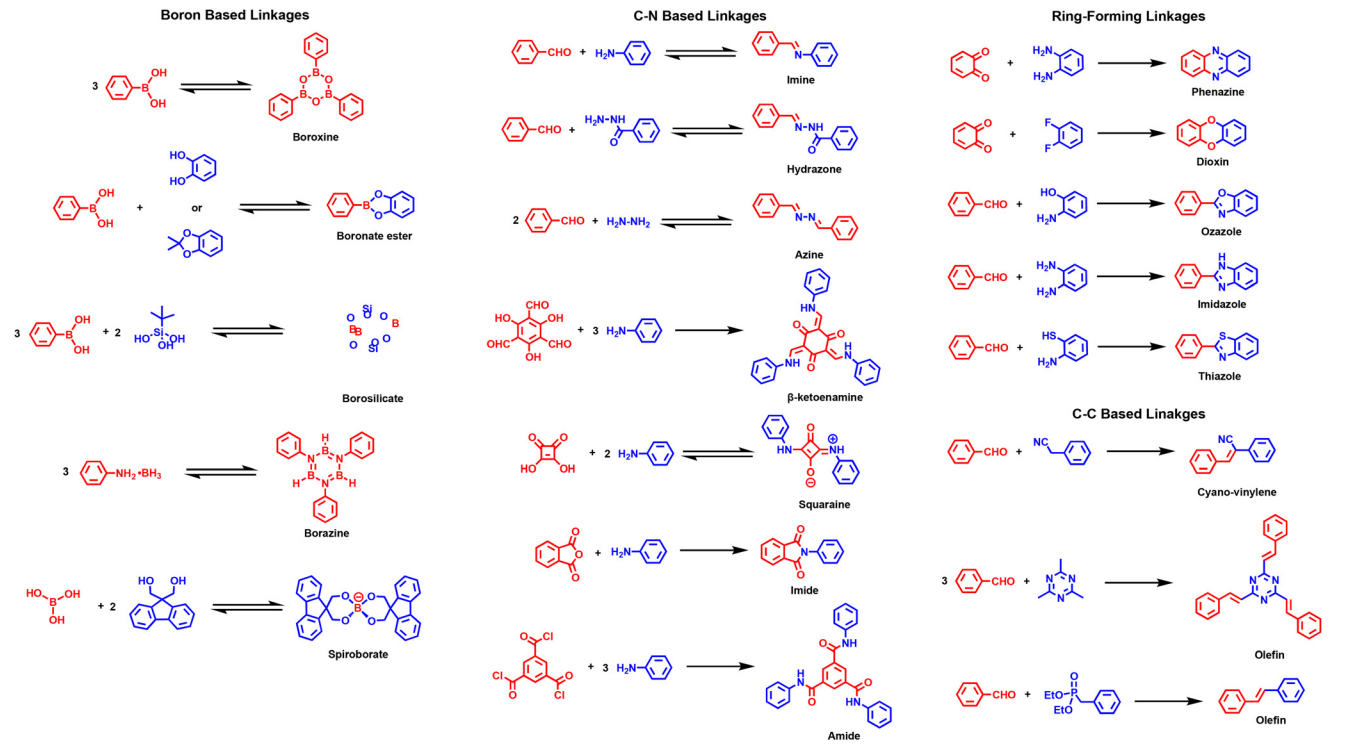

Fig. 6 Various formation of COF linkages.

Therefore, they must be utilized under anhydrous conditions, which limits their use in practical applications.

The most studied linkages in COFs are based on C–N bonds. These include, but are not limited to, imine, hydrazone, azine, β-ketoenamine, squaraine, amide, and imide linkages (Fig. 6). The first C–N-based COF was COF-300 and based on an imine linkage.[35] Although imine bonds are much more stable than their boron-based counterparts, they still suffer from limited stability in highly acidic conditions and in the presence of strong nucleophiles. Imines can also be converted to other linkages such as amide,[36] quinoline,[37] benzoxazole,[38] benzothiazole,[39] and others.[40] The chemical stabilities of boron- and imine-linkages can be improved by incorporating hydrogen bonding interactions[41–43] and alkyl or alkoxy chains.[44,45]

The first hydrazone-based COFs, COF-42 and COF-43, were reported in 2011.[46] Hydrazones have similar properties to imines but are slightly more stable due to additional hydrogen-bonding interactions. Hydrazones are less susceptible to hydrolysis in acidic conditions but are still fragile to nucleophiles. However, azine-linked COFs, first reported in 2013,[47] have superior stability in aqueous solution, acidic or basic conditions, in the presence of nucleophiles and a plethora of polar solvents. The β-ketoenamine linkage has also been used due to its superior chemical stability.[48] By adding hydroxyl groups adjacent to the aldehydes, enol–keto tautomerism is enabled where the crystallinity of the COF is dictated by the initial reversible Schiff-base imine formation followed by the irreversible tautomerism to form the highly stable β-ketoenamine linkage. However, this linkage has limited utility, as 1,3,5-triformylphloroglucinol is the typical monomer of choice due to the synthetic difficulty of installing alcohol substituents in the *ortho* position of aldehydes on most building blocks.

A squaraine-linked COF was synthesized in 2013.[49] The zigzag conformation inhibits the layered COF from sideslip and exhibits high stability in most solvents. Its zwitterionic nature also allows for extended π-conjugation through resonance. Similarly, imide-linked COFs have outstanding stabilities due to the overall irreversibility of the final bond formation. Although the reaction as a whole is considered irreversible, the first step of the nucleophilic attack of the alcohol is reversible, which allows the formation of a crystalline polymer. The first imide-linked COF was reported in 2014, and it required high reaction temperatures of 200–250 °C for 5–7 days for defect healing.[50] The first directly synthesized amide-linked COF was documented in 2017.[51] Since the reaction between acyl chlorides and amines is irreversible, amide-linked COFs are very difficult to synthesize directly and result in lower crystallinities. In the first documented amide COF work, the synthesis involved stirring at 0 °C followed by heating at 250 °C under vacuum to allow for slow reaction time followed by high heat for error correcting. More common routes for amide-linked COFs involve post-synthetic modification, which will be discussed more in Section 2.2.9. The amide linkage produces the COF with exceptional stability in a variety of aqueous and organic solvents and in the presence of many chemical reagents.

In addition to C–N-based COF linkages, C–C-based linkages are also of interest due to their robustness, lack of bond polarization, and ability to delocalize π-electrons permitting COF-based systems with extended conjugation. The two main types of C–C bond linkages consist of cyano-olefin and olefin (Fig. 6). Due to the complete irreversibility of the olefin bond, COFs linked through C=C bonds suffer from low crystallinities. The first cyano-vinylene COF was synthesized in 2016 though Knoevenagel condensation of an aldehyde and a benzyl cyanide.[52] Adjusting the base and temperature, the Knoevenagel condensation can be fairly reversible in the initial steps before the C=C bond is formed resulting in a crystalline material. The presence of the cyano substituent reduces the overall stability of the olefin bond due to its electron-withdrawing nature, and it can also react with harsh nucleophiles such as Grignard and lithium reagents. To remedy this, olefin-linked COFs can be synthesized by an aldol condensation to avoid these issues.[53,54] The initial reversibility of the aldol condensation permits error correcting before the irreversible olefin bond is formed creating a crystalline material. Although the olefin-linkage is highly stable, the design is limited for this type of reaction and typically relies on monomers such as 2,5-dimethylpyrazine, 2,4,6-trimethyltriazine, and 2,4,6-trimethylpyridine. There are also rare reports of making a heteroatom-free olefin-linked COF using the Horner–Wadsworth–Emmons reaction.[55,56]

Ring-forming reactions have also been explored to create COF linkages due to ring systems exhibiting exceptional stability and their capacity to extend conjugation. The first example of a ring-forming linkage was a phenazine-linked COF reported in 2013.[57] In 2018, dioxin-linked COFs were synthesized through a nucleophilic aromatic substitution reaction.[58] It was proposed that the nucleophilic attack is reversible, and the ring closure is irreversible, yielding crystalline materials that were highly stable. Also, benzoxazole-linked COFs were reported in 2018 displaying excellent stability in aqueous, basic, acidic, and other media.[59] The reaction first occurs in a reversible imine bond formation, allowing for error correction, followed by the irreversible oxazole ring cyclization and oxidation/dehydrogenation. In 2019, an imidazole-linked COF was synthesized which exhibited great stability.[60] Thiazole-linked COFs were directly synthesized in 2020 using elemental sulfur and DMSO.[61] A highly crystalline material was made by undergoing a reversible imine condensation followed by an electrophilic attack with sulfur which undergoes irreversible cyclization and oxidative aromatization to give the highly stable COF. Notably, some of these mentioned ring-linked COFs, and others, are commonly made through post-synthetic modification of the imine linkage, which will be discussed further in Section 2.2.9.

2.1.3 Dimensionality and topology. Based on monomer design, one can dictate the dimensionality and topology of COFs. Making a monomer two-dimensional (2D) or three-dimensional (3D) can dictate the overall dimensionality of the

COF. Mainly 2D and 3D COFs are observed in the literature, but there are reports of 1-dimensional (1D) COFs as well. Changing the monomer symmetry and the overall dimensionality of the COF can affect its pore volume and size, topology, and other general properties. COF dimensionality and topology is important for many applications, specifically in photocatalysis, because this can change the COF's diffusion rate, accessibility of the active sites, the HOMO–LUMO gap, photoelectron transfer efficiency, photoluminescence lifetimes, and self-quenching and aggregation-based quenching behaviour. There are several reports of systems that illustrated how the 2D *versus* 3D COF exhibit different photocatalytic activities.[62,63]

1D COFs provide a unique platform for photocatalysis[64,65] and other applications.[66–68] In 2D and 3D COFs the active sites and/or functional moieties typically reside within their pores and channels, which may inhibit access to them or require longer reaction times to allow for diffusion. Comparatively, 1D COFs are extended in a linear fashion by using a C_2 monomer to essentially cap the COF and prevent extension in a second direction (Fig. 7). The one-dimensionality can also facilitate easier exfoliation of layers to reduce aggregation-based quenching while also allowing for exterior functionalization at the lateral positions. Currently, there is a lack of development of 1D COFs for photocatalysis.

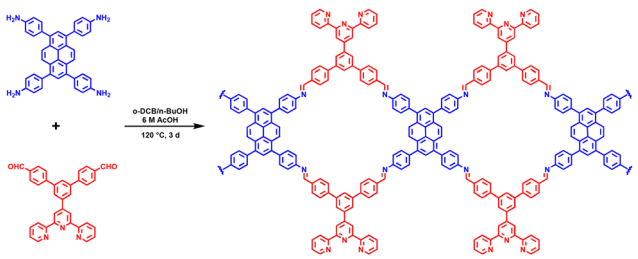

Fig. 7 Synthesis of 1D Tpy-COF.[65]

2D COFs are the most studied and prevalent in the literature due to the reliance of utilizing rigid, planar molecules with π-backbones that induce π–π stacking, and the diversity of monomers. The building blocks can have a variety of symmetries to afford isotropic topologies and anisotropic topologies. Some typical 2D COF topologies are hexagonal, tetragonal, rhombic, kagome, and triangular (Fig. 8). Hexagonal COFs can be made from $C_2 + C_2 + C_2$, $C_2 + C_3$, and $C_3 + C_3$. Tetragonal COFs can be made from $C_2 + C_4$ and $C_4 + C_4$. Rhombic COFs can be made from $C_2 + C_2$. Kagome COFs can be made from $C_2 + C_2$ or $C_2 + C_4$. Triangular COFs can be made from $C_2 + C_6$ or $C_2 + C_3$. These topologies all result from a two-component 1 + 1 strategy (*e.g.* one unique aldehyde monomer combined with one unique amine monomer), but a multicomponent 1 + 2 or 1 + 3 strategy (*e.g.* one unique aldehyde monomer combined with two or three different amine

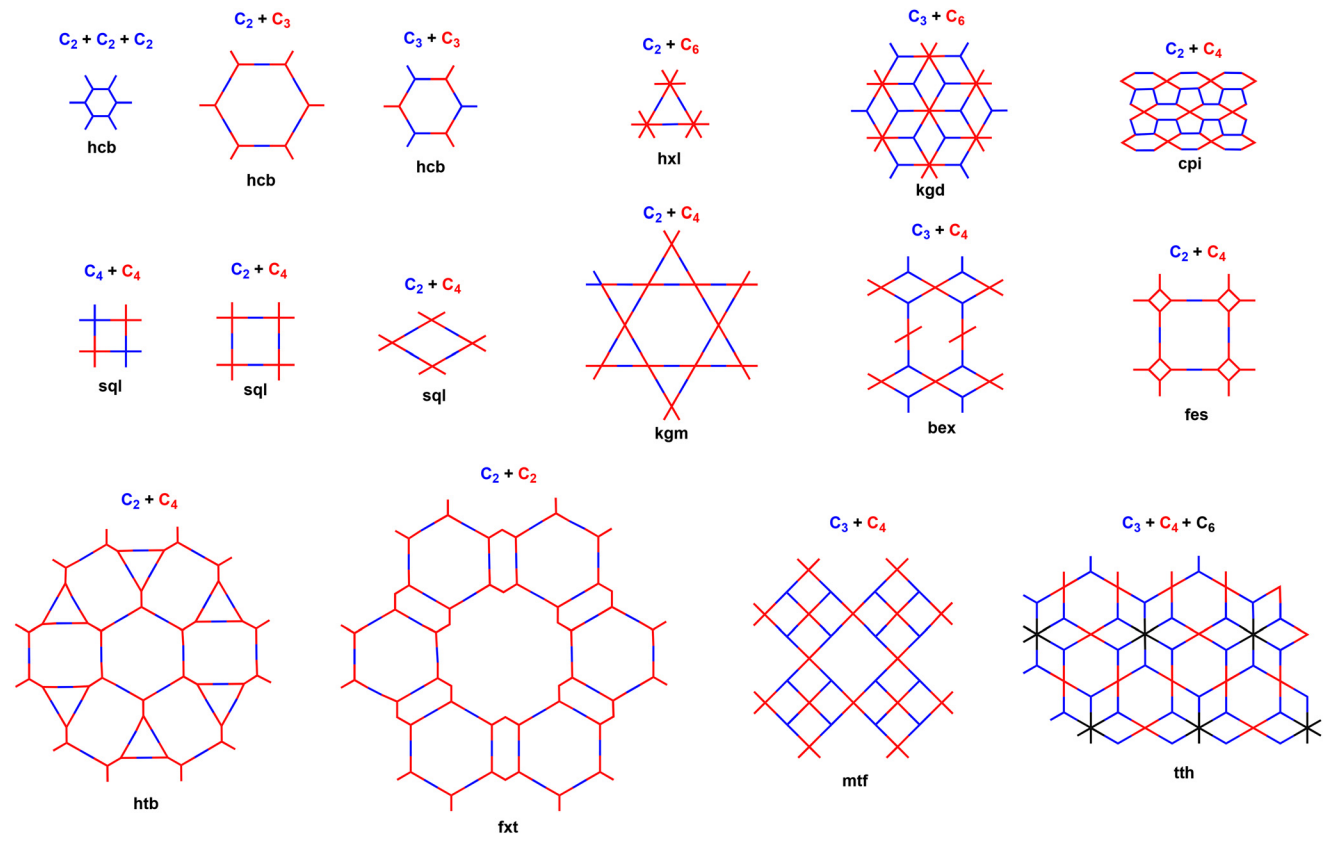

Fig. 8 Reported periodic nets of 2D COFs.

monomers) can result in dozens of asymmetric topologies. Notably, changing the monomers and topologies will affect the pore size and column π-density. Additionally, 2D COFs provide a good platform for making thin films whether through interfacial synthesis, exfoliation methods, or fabrication on a substrate. These methods will be discussed in Section 2.2.7. Concerning photocatalysis, 2D COFs are what is typically used, but again can suffer from aggregation-based quenching due to the strong π–π stacking from the layers.

3D COFs are less prevalent than their 2D counterparts but are important and just as, if not more, catalytically active. To synthesize a 3D COF, there needs to be at least one monomer that has T_d, D_{3h}, or D_{2h} symmetry (tetrahedral, triangular prism, or cubic symmetry, respectively) that extends it out into three dimensions. There are not many examples of T_d monomers in the literature and these monomers are archetypally based on tetraphenylmethane, tetraphenylsilane, or adamantane. The synthetic difficulty of making 3D building units or building units with high connectivity (≥5) has limited the construction of many unique 3D COFs. The first 3D COFs were reported in 2007 by Yaghi.[69] T_d monomers have been used to synthesize 3D COFs with ctn,[69] bor,[69] dia,[35] pts,[70] rra,[71] lon,[72] ljh,[73] and qtz[74] topologies. D_{3h} monomers have been used to make 3D COFs with tbo,[75] stp,[76] ceq,[77] acs,[77] hea,[78] and nia[79] topologies. D_{2h} monomers have been used to synthesize COFs with ffc,[80] fjh,[81] scu,[82] bcu,[83] pcb,[84] the,[85] flu,[86] pto,[87] mhq-z,[87] and crb[88] topologies. Using the linkage design, spiroborate-linked COFs have also taken nbo[89] and rra[71] topologies and a silicate-linked COF making a srs[90] topology. The use of Cu metal complexes as building units has unlocked other "woven" topologies.[91] The soc and spn topologies were also achieved by using a Ti^{IV} complex as a building unit.[92,93] pcu,[94] she,[95] sql-c,[96] tty[97] topologies have also been reported through the use of complex building units. Although new topologies of 3D COFs are reported every year, the number of 3D COF topologies that exist are still limited in comparison with the topologies of other 3D materials and the >3500 topologies that are theoretically plausible.[98] Due to multi-folding and interpenetration, it is difficult to try and pre-design a 3D COF since the parameters that control the folding mechanism are not fully understood.[99] In the same vein, 3D COFs typically result in much lower porosity than theoretically determined due to folding, interpenetration, and the inability to remove unreacted monomer from the pores. Overall, 3D COFs have excellent potential in many applications due to their capacity to achieve high porosities and many topologies. Specifically, for photocatalysis, the three-dimensional nature can also affect the photophysical properties and reduce aggregation-based quenching due to the absence of 2D layers.

2.2 Synthetic methods

The synthesis of COFs is dependent on controlling the rate at which the covalent bonds are formed. If a reaction proceeds too quickly an amorphous material will be produced. Allowing the covalent linkages to error correct enables the construction of a crystalline material. In essence, COF synthesis requires a self-healing period to correct any defects during the nucleation and growth processes. Thus, there are many synthetic methods that have been used and developed in order to prepare highly crystalline COFs.

2.2.1 Solvothermal synthesis. The solvothermal method is the primary technique to synthesize COFs. Some key parameters in solvothermal synthesis include solvents and solvent ratios, monomer concentration, temperature, time, catalyst and catalyst concentration. The solubility of the monomers and their reactivity play a key role in the crystallization process due to the rate of crystal growth, crystal nucleation events, and self-healing capacity. The two ways for solvothermal synthesis to be conducted are the conventional vial, pressure tube, or round bottom method, or the more commonly seen ampoule method. When using the ampoule method, the monomers, catalyst, and solvents are added, sonicated for a short time to homogenize the solution, and then degassed *via* freeze–pump–thaw cycles, and flame-sealed. The ampoule is then placed in an oven at the desired temperature and set time. When the reaction is complete, the ampoule is cooled to room temperature, opened, and the precipitate is collected by filtration or centrifugation. The precipitate is then washed with excess solvents and/or by Soxhlet extraction to remove remaining monomers or oligomers. Lastly, the remaining product is dried under vacuum while heating to fully activate the material. Notably, when washing the COF material post-synthesis, it is customary to go from high boiling point and high surface tension solvents to low boiling point and low surface tension solvents to make activation of the COF easier and reduce the chance of collapsing the framework.[100–102]

2.2.2 Microwave synthesis. Microwave-assisted heating has been explored to synthesize COFs.[103] Solvothermal synthesis typically has long reaction times and high temperatures, so using microwave irradiation can lead to shorter reaction times and better control of the temperatures and pressures. Additionally, microwave synthesis can increase the yield and product quality.[104] For example, Cooper and co-workers synthesized COF-5 *via* microwave synthesis which was completed in 20 min *versus* the 72 hours for the solvothermal method (more than 200 times faster) and achieved higher surface area (2019 $m^2\ g^{-1}$ *versus* 1590 $m^2\ g^{-1}$).[105] Additionally, TpPa-COF was made using this method in 60 min and achieved yields of 83% *versus* 8% using conventional heating.[106]

2.2.3 Sonochemical synthesis. Sonochemical synthesis has also been explored for COF synthesis to improve reaction times and save energy. Here, ultrasound is used to induce cavitation of the solvent, which creates localized spots of extraordinarily high temperatures and pressures promoting the reaction. Markedly, particle sizes are smaller through the sonochemical method. Ahn *et al.* synthesized COF-1 and COF-5 sonochemically in 1–2 hours and with similar or higher surface areas compared with the solvothermal method.[107] Similarly Shim and co-workers synthesized COF-5 on carbon nanotubes and graphene.[108] Cooper and co-workers synthesized COFs sonochemically even in food-grade vinegar and showed photocatalytic activity for hydrogen evolution from water.[109]

2.2.4 Mechanochemical synthesis. Since it does not require the use of solvents and results in fast reaction times, mechanochemical synthesis is considered to be a convenient green approach for making COFs and is performed at room temperature. Furthermore, this method produces exfoliated COF layers compared with the solvothermal method. Here, the monomers are ground finely using a mortar and pestle at room temperature to afford the COF. Banerjee *et al.* synthesized COFs TpPa-1 and TpPa-2 using this method. Interestingly, the colour of the powder changed during the grinding period from yellow to orange to red (Fig. 9).[110] The crystallinity of the COF was slightly less than reported likely due to exfoliation during the synthesis, and similar surface areas were reported. Wang and co-workers used the same method to synthesize TpAzo COF within 20 min.[111] Li and co-workers synthesized six imine-linked COFs *via* liquid-assisted mechanochemical synthesis using a ball-milling machine.[112] The COFs demonstrated high crystallinity and high surface areas. Likewise, the Banerjee group also synthesized TpBpy COF through liquid-assisted mechano-grinding.[113] This method produced a less crystalline product but provided a better performance in fuel cells. Zhao *et al.* synthesized COFs NUS-9 and NUS-10 through mechanochemistry in 45–60 min and in 75–80% yields.[114]

2.2.5 Photochemical synthesis. Just as COFs have been proposed for use in photocatalysis and other photobased applications, the utilization of visible light has also been proposed to construct COFs. Choi and Kim have shown that light can be used for making an imine-linked COF, hcc COF, using 1,2,4,5-benzenetetramine (BTA) and hexaketocyclohexane (HCH) monomers with acetic acid catalyst and irradiating the sample with simulated sunlight at wavelengths ranging from 200 to 2500 nm.[115] Remarkably, the COF was synthesized in 3 hours with about 80% yield and had high crystallinity and surface area of about 600 $m^2\ g^{-1}$. This method of synthesis is also theoretically only available to highly conjugated COFs made from conjugated monomers or monomers that efficiently absorb light.

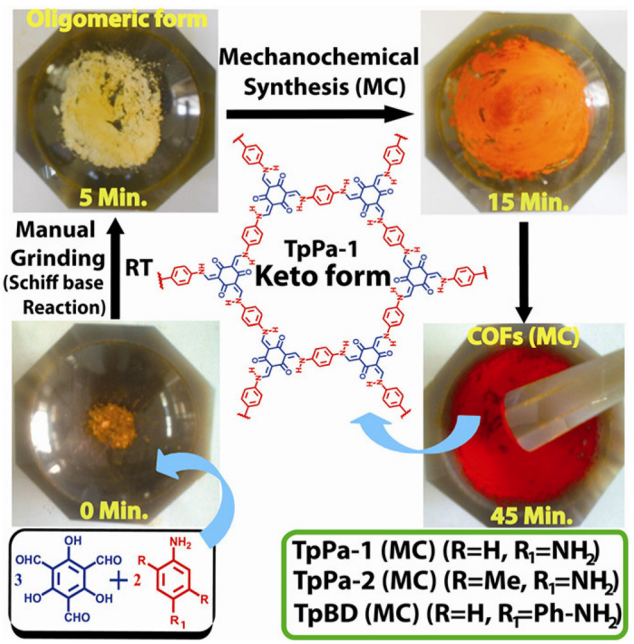

Fig. 9 Schematic representation of the MC synthesis of TpPa-1 (MC), TpPa-2 (MC), and TpBD (MC) through simple Schiff base reactions performed *via* MC grinding using a mortar and pestle.[110] Reproduced with permission from ref. 110. Copyright 2013, American Chemical Society.

2.2.6 Ionothermal synthesis. Ionothermal synthesis has also been presented as a method to make COFs. In ionothermal synthesis, molten salts, such as molten $ZnCl_2$, or ionic liquids are used as the solvent, catalyst, and template, and it is typically done at high temperatures (>300 °C) and pressures. This is the typical method for synthesizing covalent triazine frameworks (CTFs). Not all CTFs are crystalline, but crystalline versions of CTF-1 and CTF-2 have been made using this method.[116] Lotsch and co-workers ionothermally synthesized imide-linked COFs using $ZnCl_2$ in high yields.[117] Recently, Coskun *et al.* used a mixed metal ionothermal synthesis of metallophthalocyanine COFs.[118] Furthermore, Qiu and co-workers synthesized three 3D ionic liquid COFs, 3D-IL-COFs, using this method with 1-butyl-3-methylimidazolium bis((trifluoromethyl)sulfonyl)imide as the ionic liquid solvent, and in 12 hours achieving high crystallinity and surface areas.[119] A disadvantage of this method is the potential decomposition and side reactions due to the very high temperatures that are required for the reaction. Ionothermal synthesis also requires the COF to be stable at such high temperature.

2.2.7 Interfacial synthesis and thin films. Semiconductor thin films have found use in a wide array of applications,[120,121] so the construction of COF thin films has been explored.[122] One way to create a COF thin film is by interfacial synthesis. Here, the monomers react with each other only at the interface, yielding a thin film (Fig. 10).[121] The interface can either be liquid–liquid or liquid–air. For liquid–liquid interfaces it is important that the liquids are not miscible with each other, and that each monomer is soluble in one of the liquids being used. A common pairing is water and an organic solvent such as dichloromethane. Banerjee *et al.* synthesized several β-ketoenamine COFs interfacially, namely Tp-Bpy, Tp-Azo, Tp-Ttba, and Tp-Tta (Fig. 10).[123] First 1,3,5-triformylphloroglucinol was dissolved in dichloromethane, then water was added on top followed by an aqueous solution of amine monomer and *p*-toluenesulfonic acid, then this was left to sit for 72 hours, yielding a crystalline COF with high surface area and ~75 nm thickness. Dichtel and co-workers synthesized TAPB-PDA COF interfacially using tris(4-aminophenyl)benzene and terephthalaldehyde monomers.[124] Wang and co-workers also synthesized COF-TTA-DHTA by dissolving 4,4′,4″-(1,3,5-triazine-2,4,6-triyl)trianiline (TTA), acetic acid, and $Sc(OTf)_3$ catalyst in water which was spread on a hydrogel, and DHTA was dissolved in tridecane, and then this was immersed on the hydrogel under the tridecane layer.[125] By changing the concentration of the monomers a thickness of 4 to 150 nm could be regulated. They also synthesized TpPA COF in a similar

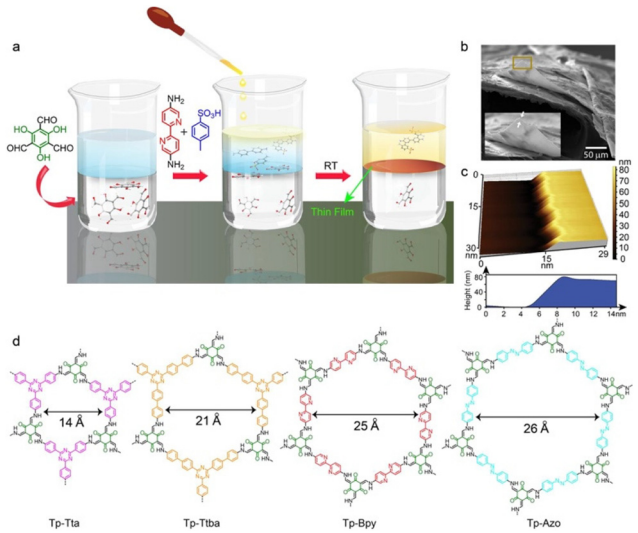

Fig. 10 Synthesis scheme of COF thin films. (a) Schematic representation of the interfacial crystallization process used to synthesize the Tp-Bpy thin film. The bottom colorless layer corresponds to aldehyde in dichloromethane solution, the blue layer contains only water as the spacer solution, and the top yellow layer is the Bpy amine-PTSA aqueous solution. (b and c) SEM and AFM images (with corresponding height profile), respectively, of the Tp-Bpy thin film synthesized as illustrated in (a). (d) Chemdraw structures of all the COFs used for synthesizing the thin films *via* interfacial crystallization process.[123] Reproduced with permission from ref. 123. Copyright 2017, American Chemical Society.

method using 1,3,5-triformylphloroglucinol in the tridecane layer and *p*-phenylenediamine dihydrochloride in the hydrogel. Bao *et al.* synthesized a COF through liquid–air interface using 2,6-dicarbaldehyde-4,8-dioctyloxybenzo[1,2-*b*:3,4-*b*′] dithiophene and tris(4-aminophenyl)amine monomers in DMF and acetic acid solution to give a crystalline COF with thicknesses of 1.8–2.9 nm by varying the concentration and incubation time.[126] Zheng *et al.* synthesized 2D COFs with large single-crystalline domains on the surface of water using a charged polymer.[127] Börjesson and co-workers were also able to make a 3D COF interfacially.[128] Recently, Chen *et al.* were the first to be able to synthesize an olefin-linked COF, TFBP-PDAN, interfacially.[129] Interestingly, Wang and co-workers used table salt as a sacrificial reagent to make COF thin films.[130] The Jia group used a hexane–ionic liquid interfacial system to grow COF thin films.[131] COF thin films can also be created by growth on a substrate, such as graphene or ITO, or indirectly by vapor-assisted conversion, continuous flow conditions, and several methods of exfoliation.[122]

2.2.8 Single-crystalline COFs. In most cases, COFs are produced as polycrystalline powders. While this is suitable for most COFs, it is imperative to make single crystals of COFs to fully understand their crystal structure and stacking. This is because modelling COF structures from powder X-ray diffraction (PXRD) is not perfect, especially in complex 3D systems where interpenetration and nets occur, atomic positions and bond lengths and angles are very difficult to obtain and refine, and guest arrangement in the pores and channels cannot be clearly resolved. Growing single crystals of COFs is difficult due the significant number of covalent and non-covalent interactions, limited solubility of the monomers, and a limited understanding of nucleation and growth processes for most linkages. However, there are reports of single-crystalline COFs.

The first single crystal of a COF was reported by the Yaghi and Wuest groups in 2013.[132,133] Wuest achieved this through the reversible self-addition polymerization of tetranitroso monomers to form a 3D COF. Zhao and co-workers were able to make micron-sized single-crystalline COFs by studying the mechanism of the growth and nucleation through intermediate tracing.[134] Yaghi and co-workers developed a modulation method to grow large single-crystals.[72] Wei *et al.* performed crystallization of COFs using supercritical CO_2 to vastly reduce times to form single-crystalline COFs, and these showed heightened photoconductive properties than the polycrystalline counterpart.[135] Wang *et al.* were the first to synthesize a 3D COF with a high (6-fold) connectivity.[136] This lab also was the first to construct a non-interpenetrated 3D COF single crystal.[137] Loh and co-workers were the first to synthesize single crystals of a 1D COF.[138] Zheng *et al.* were able to grow 2D COF thin films with single-crystalline domains.[127] They also explored the use of amino-acid derivatives to grow gram-scale single-crystalline imine COFs.[139] The authors believe that the amino acid based compounds can self-assemble into micelles and regulate the polymerization and crystallization processes. Dichtel developed a method to grow single-crystalline 2D COFs by slow monomer addition and seeded growth.[140] The Jiang group also performed post-synthetic modification on single crystals of an imine-linked COF, USTB-5, where the imine was reduced or oxidized to yield amine and amide linkages, respectively.[141] Whereas COF single-crystal growth takes weeks to months, Wang *et al.* created a method to grow COF single crystals in only one or two days using trifluoroacetic acid (TFA) as a catalyst and trifluoroethylamine as a modulator.[142] Although a sizable amount of work has been performed to grow single-crystalline COFs, there still is a need to create better, quicker, translatable, and scalable methods that can be widely applied beyond imine- and boronate ester-linked COFs.

2.2.9 Post-synthetic modification. Post-synthetic modification (PSM) is a very powerful tool that is used to tailor the functional properties of COFs and their catalytic activities.[30,143,144] Importantly, some functional groups may not be tolerant to initial synthesis conditions, so adhering them using PSM provides a useful approach for incorporating them into the COF structure. Furthermore, this approach can make monomers easier to synthesize as it may require fewer steps to make the very complex building block. Moreover, PSM of the COF can be easier to perform than monomer synthesis since the COF will be heterogeneous and easier to separate from the reaction mixture. The most common PSM is post-metalation of ligands incorporated into the COF including, but not limited to, porphyrins, bipyridines, salens, and dehydrobenzoannulenes.[30] Pre-metalation of monomers may

prevent crystalline formation or cause the metal to leach during COF synthesis. Metalation of the formed imine,[145–147] β-ketoenamine[148,149] hydrazone,[150,151] and β-ketohydrazone[152] linkages has also been conducted. Furthermore, the linkages themselves have also been post-synthetically modified to form other linkages. Just as seen in metal organic frameworks (MOFs), taking advantage of the dynamic bond formation in COFs researchers have explored linker exchange.[153–155] Common routes for amide-linked COFs involve PSM through monomer exchange by adding in acyl chloride post imine COF formation or by oxidation of the imine bond.[36] Benzoxazole and benzothiazole-linked COFs have also been synthesized through oxidative PSM of the imine bond.[38,39] Imine linkages have also been used as a platform to form a variety of different covalent linkages.[37,40] The COF building units themselves can also undergo PSM to yield alternative functionality. Click reactions have long been used to functionalize COFs by azide–alkyne cycloaddition[156–158] or thiol–ene reaction.[159–161] Post-functionalization of phenolic groups is another common tactic to adhere different moieties to the monomer units.[162–164] Overall, there is a huge library of methods for the PSM of COFs.

3 COF characterization

Characterization techniques are essential for evaluating the structural, compositional, and functional properties of COFs. The choice of techniques depends on the specific properties that researchers aim to investigate. The following are some general techniques and the corresponding broad evaluations for insights into such materials.

3.1 Basic COF characterization methods

Understanding the intricate world of covalent organic frameworks (COFs) hinges on a battery of investigative techniques. These methods act like a key, unlocking the secrets of a COF's structure and properties, which ultimately determine its potential applications. Powder X-ray Diffraction (PXRD) serves as a foundational tool, offering a glimpse into the COF's internal organization and order. Fourier-Transform Infrared Spectroscopy (FTIR) acts as a chemical detective, scrutinizing the building blocks and ensuring the COF is free from unwanted remnants. Visualizing the COF's physical form comes into play with scanning electron microscopy (SEM) and transmission electron microscopy (TEM). SEM provides a surface-level perspective, revealing the COF's external features and size. TEM delves deeper, showcasing the intricate network of pores and the overall framework organization at an incredible nanoscale. For applications like gas storage or catalysis, N_2 sorption analysis is a crucial technique. It assesses the COF's capacity to encapsulate gas molecules, providing vital details about the available surface area, pore size distribution, and total pore volume. Solid-state nuclear magnetic resonance (SS-NMR) spectroscopy, specifically ^{13}C cross-polarization magic angle spinning (^{13}C CPMAS-NMR), acts as an advanced probe, examining the COF's internal chemical environment. By analysing the magnetic fields surrounding specific atoms, researchers can confirm the successful formation of the desired linkages and identify any functionality flaws or impurities within the COF. This suite of characterization methods empowers researchers to unlock the potential of COFs and pave the way for their advancement in various technological fields.

3.1.1 Powder X-ray diffraction (PXRD). Powder X-ray Diffraction (PXRD) has emerged as a powerful tool, acting as a decoder ring for the COF's crystallographic secrets. When X-rays interact with the COF's ordered atomic organization, a unique diffraction pattern emerges. By deciphering this pattern, scientists can glean valuable insights into the dimensions of the fundamental unit cell, the spacing between atomic planes, and the overall crystallographic order within the COF. PXRD serves as a workhorse technique in COF research for several reasons. Primarily, it allows researchers to verify if the targeted COF structure has been successfully formed. Additionally, PXRD acts as a guardian against impurities by identifying any unwanted crystalline phases or nanoparticles present within the COF sample through the presence of extraneous peaks in the diffraction pattern. Furthermore, PXRD can be harnessed to monitor the COF crystallization process in real time, offering a window into the growth and development of the COF crystals. Pawley refinement facilitates the identification of discrepancies between the theoretical and experimentally observed PXRD patterns of COFs. Equally, theoretical simulations can be employed to elucidate the stacking mode (*e.g.*, AA, AB, *etc.*) within the COF structure based on the best match between the simulated and experimental PXRD data. Though PXRD is undeniably a powerful tool, it does have limitations. COFs with a high degree of disorder might generate weak signals and interpreting complex patterns from COFs with intricate structures can be a challenge. Pervasively, PXRD remains an essential technique for COF characterization.

3.1.2 Fourier-transform infrared (FTIR) spectroscopy. Fourier Transform Infrared (FTIR) Spectroscopy is an important technique in characterizing covalent organic frameworks. By analysing the FTIR spectra, researchers can gain valuable insights into the structure and functional groups present in the materials. FTIR spectroscopy helps monitor bond formation during synthesis by comparing the spectra of the starting materials and the final COF. An individual can track the disappearance of starting material peaks and the emergence of new peaks representing bond formation of the COF linkage. Furthermore, FTIR can be used to identify defects in the COF structure by detecting residual functional groups from unreacted materials. FTIR spectroscopy can be used to monitor COF stability under various conditions. Comparing the spectra before and after treatment reveals any changes in the functional groups present, indicating potential degradation of the COF structure. Post modification in COFs can also be analysed using FTIR spectroscopy. Comparing the FTIR of the pristine COF and the modified COF, the appearance of new functional group peaks after the modification or

the disappearance of certain peaks suggests removal or conversion, and a shift in peak position can also hint at a change in the structure. Overall, FTIR spectroscopy provides a broad and non-destructive approach for characterizing COFs, making it an essential tool for researchers in this field.

3.1.3 Solid-state nuclear magnetic resonance (SS-NMR). Unlike the basic characterization techniques such as X-ray diffraction and FTIR which provide general information on the material, solid-state nuclear magnetic resonance (SS-NMR) reveals deeper insights into the synthesized material as it is a powerful approach for characterization at the atomic level. ^{13}C CPMAS-NMR targets the ^{13}C nuclei within a COF structure. By spinning the sample rapidly at the magic angle ($\theta_m \sim 54.74°$), it cancels out interactions that would normally broaden the signal. This allows researchers to analyse the chemical environment surrounding each carbon atom, revealing details about the COF's structure and any post-modifications. Chemical composition and functionality can be analysed by researchers by confirming the peaks leading to successful incorporation of the targeted functional groups within the COF structure. Additionally, connectivity and defects in the structure can be analysed by comparing the spectra of the target final material with a model analogue.

3.1.4 Surface area and pore size analysis. Understanding the surface area and pore size distribution in covalent organic frameworks is important as they have direct correlation in applications such as adsorption, catalysis, and separation due to substrate–material interactions. The Brunauer–Emmett–Teller (BET) method is a key technique for analysing this property; during this analysis gas, commonly N_2, is adsorbed onto the surface of the COF material at variable pressures. By analysing the content of gas adsorbed at each pressure, the surface area of the material is calculated. This information can also be used to get a general idea of the guest–host molecule interaction. Knowing the pore size is important as it could be helpful in specific targeted applications; micropore COFs are helpful in selective capture of small molecules, while macroporous and mesoporous materials are better for catalytic applications, allowing for larger substrates to diffuse. Importantly, the shape of adsorption–desorption isotherm obtained is helpful in predicting the pore size distribution within the COF. A COF can be subcategorized into micropores (less than 2 nm), mesopores (2–50 nm), and macropores (greater than 50 nm), and this can be identified based on the isotherm characteristics. Less commonly, the Langmuir model is also used to analyse the porosity in COF materials. It works on the assumptions of a homogeneous surface with uniform sized pores and describes the process of gas adsorption as a monolayer adsorption on the pore wall; however, this method leads to much higher surface areas calculated than in the BET model. Furthermore, Quenched Solid Density Functional Theory (QSDFT) and Non-Local Density Functional Theory (NLDFT) are computational tools used to analyse the pore size in COF materials. These models help to provide a better picture of pore size compared with other existing models. In conclusion, surface area and pore size analysis are very crucial and an important tool in COF research as they pave the way for these materials for diverse applications.

3.1.5 Scanning electron microscopy (SEM) and transmission electron microscopy (TEM). Surface imaging plays an important role in characterizing COF materials. True insight into the morphology, pore structure and crystalline order can be gained using SEM and TEM analysis. Though complementary information can be gained from these analyses combined, they operate on different principles. In SEM, a beam of electrons is focused on the surface of the COF material; some electrons get back scattered and are detected by a detector that converts this into high-resolution 3D images revealing surface details of the COF. SEM is excellent for revealing the size and shape, particle aggregation, and external surface texture. It can also be used to identify defects by noticing irregularities in the observed images. However, it is limited in providing information related to the surface and not the internal structure. An opening past such limitations is accomplished using TEM analysis. In TEM, a beam of electrons strikes a very thin layer of COF material, and scattered or transmitted electrons are used to generate a 2D image. Regions dense with atoms scatter more electrons, creating darker sites in the image. The internal structure of the pores and the pore size distribution can be studied using High Resolution Transmission Electron Microscopy (HR-TEM). With HR-TEM the crystallographic arrangements of the atoms can be analysed. However, TEM strictly requires ultrathin layers in sample preparations, which can be a challenge for COF materials. In total, SEM and TEM together provide comprehensive detail of the COF surface. Using both in combination, researchers can gain an in-depth understanding of a COF's overall architecture.

3.2 COF characterization for photocatalytic application

The photoelectric potential of COFs can be evaluated using characterization techniques as well. The following are some general techniques and the corresponding photoelectrical evaluations for insights into such materials.

3.2.1 Diffuse reflectance and Tauc plots. For applications in photocatalysis and optoelectronics, understanding the interaction and light absorption properties of COFs becomes very crucial. The amount of light reflected at different wavelengths across the UV and visible region is measured using diffuse reflectance UV-Vis spectroscopy. This technique helps to provide information about the absorptive properties that occur in the material. Also, this technique is well suited for studying the optical properties of powdered materials like COFs. Valuable information can be obtained by analysing the diffuse reflectance using Tauc plots to obtain the band gap of the COF material. A Tauc plot provides a relationship between the photon energy and light energy coefficient of the material. By extrapolating a linear portion of the curve from the plotted data, the energy required to transition an electron from the valence band to the conduction band can be experimentally calculated. The light absorption property of a COF has a direct correlation with this calculated band gap energy. With the help of this basic analysis, the optical potential of COFs can be

understood and can have a direct impact on applications in light-harvesting and photocatalysis.

3.2.2 Photoluminescence lifetimes. Understanding the light emission behaviour of a material significantly becomes important in the development of photocatalysts and optoelectronics. In COFs, photoluminescence lifetime refers to the average time taken for an electron in its excited state to return to its ground state after light absorption. When a COF absorbs light, the excitation of an electron from the valence band to the conduction band takes place. The excited electron in this conduction band is unstable, and eventually the electron relaxes back to the valence band; in this process energy in form of light or heat can be released. The average time required for this energy release is called photoluminescence lifetime. Low photoluminescent intensity often translates to faster charge separation and reduced recombination, promoting a more efficient catalytic cycle. Likewise, longer photoluminescence lifetimes indicate more efficient charge separation and fewer recombination events. If the reaction utilizes the molecule's triplet state, a longer lifetime allows for the crucial intersystem crossing to occur. Additionally, for multicomponent photocatalytic systems, a longer lifetime in one component can facilitate energy transfer to the true catalyst. There are cases where shorter lifetimes may be favourable. In conclusion, the lifetime depends on the specific reaction and the materials involved.

3.2.3 Photocurrent response. Photocurrent response in a COF material indicates the change in observed electric current when it is exposed to electromagnetic radiation. When a COF is exposed to a light source, and the light source energy matches the band gap, an electron transitions from the valence band to the conduction band. These excited electrons are mobile, and this movement of charge in an electrode system results in an electric current, which is measured as photocurrent. Recombination of these electrons with generated holes results in the loss of photocurrent. Analysing a COF's photocurrent response offers valuable clues for photocatalysis. A strong photocurrent signifies efficient light absorption at the relevant wavelength, a key step for initiating the photocatalytic process. Additionally, a high photocurrent compared with light intensity indicates successful separation of excited electrons and holes within the COF. This ensures more electrons reach the reaction site. Conversely, a weak or rapidly decaying photocurrent suggests limitations in light absorption, charge separation, or a high rate of electron–hole recombination, which may hinder photocatalytic activity. Variations in the photocurrent response across samples can also reveal inconsistencies in material quality. Overall, a strong and sustained photocurrent response points towards a promising COF photocatalyst, while a weak or decaying response indicates areas for improvement.

3.2.4 Mott–Schottky analysis and plots. To investigate the electrical properties of a semiconducting material, Mott–Schottky analysis becomes very important, and valuable information about a material's doping density and flat-band potentials can be gained. A semiconductor is dipped in an electrolytic solution, and at the interface a space-charge region arises due to a change in charge carrier concentrations in the semiconductor and the electrolyte. A series of varied voltages is applied, and the capacitance is calculated. A material's electrical charge storage is its capacitance. On varying voltages either an expansion or contraction in this space-charge region is observed, which directly reflects the capacitance of a material. The inverse square of the capacitance obtained is plotted *versus* the applied voltage; such type of plot is called a Mott–Schottky plot. A steep positive slope indicates the semiconducting nature, while a negative slope indicates insulating properties. Based on the nature of the graph, the type of semiconducting nature can also be assessed. Flat band potentials can be extrapolated from this plot, leading to calculations of the conduction bands. Using the equation $[E_{VB} = E_{CB} - E_g]$, the valence band positions of the material can also be calculated. Since COFs are complex materials, complementary available techniques and cautious interpretation are necessary to gain complete depiction.

3.2.5 X-ray photoelectron spectroscopy (XPS) and valance XPS. In order to understand the elemental composition and electronic structure of COF materials, X-ray Photoelectron Spectroscopy (XPS) has become a powerful technique. It involves the bombardment of X-rays on the COF, which results in the ejection of core electrons. Analysing the energy of these emitted electrons, XPS reveals which elements are present and the bonding of elements within the COF material. Importantly, XPS helps to confirm the incorporation of elements present in the framework. XPS can also determine the oxidation state of any metals present in a COF. Valence XPS can determine the position on the valence band, and with the band gap from the Tauc plot, the conduction band can be determined. However, XPS is a technique of surface-sensitivity which limits the analysis within the top few nanometers, which may not be ideal for thick COF materials.

3.2.6 Cyclic voltammetry (CV). In the context of potential applications of COFs, Cyclic Voltammetry (CV) becomes an important characterization tool. The electron transport capability of a material is assessed using this technique. The method involves the dipping of a COF material electrode in a solution and voltage is ramped and a current response is measured. As the voltage is increased, a point is achieved where a COF can gain or lose an electron, which results in an escalating current response. Reversing the voltage and scanning back down can reveal that the electron transfer is reversible. The voltammogram unveils the COF's redox behaviour. CV reveals COFs redox potentials, which are essentially the voltage required to gain or lose electrons. In photocatalysis, these potentials are of the utmost importance as the photogenerated electrons in a COF need sufficient negative potential to reduce the target molecule, whereas the holes need a positive potential to oxidize them. Specifically, CV can also be used to drive the energy of the conduction band. Comparing the redox potential of COFs with those of the target molecules, researchers can gauge the feasibility of the desired photocatalytic reactions. Additionally, it can also provide insights

into the charge transfer efficiency of a material. A sharp peak in the voltammogram suggests efficient electron transfer between the electrode and the COF material, which indirectly indicates efficient charge separation of electron–hole pairs within the COF under light irradiation, a key step for photocatalysis. However, CV is not operated under light irradiation, thus it does not directly measure the photocatalytic activity of the COF material. Therefore, to comprehensively understand the suitability for photocatalytic applications, it is best when used as a complementary technique alongside other optical characterization methods.

3.2.7 Linear sweep voltammetry (LSV). To learn more about the electrochemical behaviour of COFs, linear sweep voltammetry is a valuable technique. The experimental setup involves a three-electrode system: a working, a counter, and a reference electrode. A thin layer of COF material is deposited on the working electrode, and the counter electrode completes the circuit but does not take part in the reaction. The reference electrode acts as a point of reference. The voltage is controlled within a set range, and as the potential change occurs, the current that flows between the working and counter electrode is continuously measured. This current has a direct relationship with the electron transfer that occurs at the COF surface. The current measured is plotted *versus* the potential. A comparative plot with and without light irradiation can be helpful in understanding the charge transfer efficiency of the material. A higher current measured under light irradiation compared with in the absence of light indicates efficient separation and the movement of the photogenerated electrons and holes within the material. This translates to a more efficient photocatalytic process.

3.2.8 Electrochemical impedance spectroscopy (EIS). For materials like COFs, another method to provide electrochemical properties is Electrochemical Impedance Spectroscopy (EIS). It is used to understand how easily an electron moves through the COF material. EIS measures the response to the applied AC voltage; a Nyquist plot takes the complex data obtained into a useful outcome. The *x*-axis represents the real part (Z') of the impedance, which reflects the resistive component. The *y*-axis represents the imaginary part (Z'') of the impedance, which relates to the capacitive and inductive components. Each data point at a specific frequency translates to a single point on the Nyquist plot. As the frequency is swept across a range, a curve is formed, depicting the COF's impedance behaviour across that frequency spectrum. A semicircle at high frequencies often indicates charge transfer resistance, which is the difficulty for electrons to move between the COF and the electrolyte. A smaller semicircle signifies lower resistance and easier electron transfer. This is desirable for photocatalysis because it signifies easier movement of photogenerated electrons within the COF structure. This efficient transport allows the electrons to reach reaction sites and participate in the desired photocatalytic transformations.

3.2.9 Electron paramagnetic resonance (EPR). Electron Paramagnetic Resonance (EPR) spectroscopy is a valuable tool for investigating the electronic structure of COFs. EPR targets an unpaired electron that can be generated by light resulting in an irradiated excited state. By applying a controlled magnetic field and radio waves to the COF sample, EPR detects the absorption of specific radio frequencies by these unpaired electrons. Analysing the signal intensities in the EPR spectrum under light irradiation compared with the absence of light, the efficiency of charge separation within the COF material can be assessed. One of the key applications lies in detecting the production of reactive oxygen species (ROS) like superoxide radicals, singlet oxygen, and hydroxyl radicals. These ROS play a vital role in driving the mechanisms of photocatalytic reactions. To understand mechanisms, EPR employs a technique called spin trapping. This method helps confirm the presence of the suspected ROS species, providing crucial support for the proposed reaction pathway. EPR can also identify any paramagnetic metals in a COF.

4 Product detection and mechanistic studies in photocatalytic experiments

After conducting various photocatalytic reactions, it is crucial to use a range of analytical instruments and techniques to analyse the reaction mixture. Here we present some of the most generally used methods for analyses of product and intermediate formation in photocatalytic reactions and generic tests for mechanistic studies.

4.1 Nuclear magnetic resonance (NMR)

NMR has been widely utilized as an analytical tool for most photocatalytic reactions due to its ability to provide extensive information about a compound's molecular structure, including the chemical environment of specific nuclei and the relative arrangement of atoms.[165–167] Within a molecule, NMR can identify functional groups, allowing for the confirmation of product structure.[168,169] This analytical technique can also detect by-products and impurities in samples.[170,171] NMR is useful for quantitative analysis, enabling the calculation of the relative amounts of different constituents in mixtures.[172,173] NMR provides benefits for investigating molecular dynamics, allowing for real-time monitoring of chemical reactions and improving the comprehension of reaction kinetics and mechanisms.[174,175] It can also be employed for analysing isotopic labelling of compounds, providing more detailed insights into the mechanistic pathways of various reactions.[174,175] LED-NMR has been used to study photocatalytic processes under light irradiation.[176–179] Specifically, in heterogeneous photocatalytic reactions, *operando* NMR can be utilized to monitor proton transfer.[180] As a non-destructive technique, NMR allows the same sample to be reused for other analyses.

4.2 Gas chromatography (*in situ* and *ex situ*)

Gas chromatography (GC) is a high-resolution method to separate complex mixtures, enabling the identification and quantification of various constituents.[181,182] GC efficiently sep-

arates and detects sample components which can enable the determination of by-products, intermediates, and impurities. This unique capability makes it valuable in photocatalytic reactions.[183,184] *In situ* GC is employed for real-time observation and monitoring of reaction mechanisms and kinetics during the reaction process, allowing for the tracking of dynamic changes. *In situ* GC is also invaluable for analysing gaseous products.[185–187] *Ex situ* GC is useful after a reaction is complete, providing thorough details on the composition of the final reaction mixture, including the quantification and identification of products, by-products, intermediates, and impurities, which helps optimize reaction conditions to improve yields.[188] The versatility of GC to be compatible with different detectors, such as a Mass Spectrometer (MS),[189] Flame Ionization Detector (FID),[190] and Electron Capture Detector (ECD),[190,191] gives it an advantage in analysing various types of sample products. Both *in situ* and *ex situ* GC are indispensable for their in-depth characterization of reaction mixtures, especially since small sample amounts are required.

4.3 Diffuse reflectance infrared Fourier transform spectroscopy (DRIFTS)

Diffuse reflectance infrared Fourier transform spectroscopy (DRIFTS) is a crucial analytical tool extensively used in the characterization of polymers, catalysts, and solid samples overall.[192] One of its advantages over general transmission IR techniques is its ability to amplify weak signals for improved detection of solid surfaces. Due to its surface sensitivity, DRIFTS can identify surface functional groups and detect species adsorbed on the surfaces of solid materials.[193,194] It is employed in dynamic studies such as phase transitions, adsorption, and desorption.[192–194] *In situ* and *operando* DRIFTS enables the observation and characterization of the material or catalyst during the reaction process.[195–197] By analysing the multiple output IR spectra, DRIFTS facilitates real-time monitoring of chemical reactions, aiding in developing reaction kinetics and mechanisms. *In situ* DRIFTs has been applied successfully to monitor photocatalytic transformations.[198–202] Additionally, DRIFTS is user-friendly as it allows for the analysis of materials in their solid state, avoiding the use of solvents and possible contamination and requiring only a small sample size for analysis. As a non-destructive technique, it allows the same sample to be used in subsequent analyses by other methods.

4.4 Scavenger tests

Scavenger tests (STs) are vital, particularly in photocatalytic studies, as they provide an in-depth understanding of photocatalytic processes.[203] These tests can verify reactive oxygen species (ROS) such as superoxide radicals ($^{\bullet}O_2^-$), singlet oxygen ($^1O_2$), hydroxyl radicals ($^{\bullet}OH$), hydrogen peroxide (H_2O_2), and others. The scavenging of photogenerated electrons and holes can also be done to verify their use in photocatalytic reactions. By investigating the reactive species involved, scavenger tests help elucidate the mechanisms in photocatalytic processes.[204] By determining the reactive species and mechanism, STs can lead to improved reaction conditions, resulting in higher reaction efficiency. They can also serve as benchmarks for comparing the performance and capabilities of various photocatalysts based on their generation and utilization of reactive species. Additionally, these tests can help explain the degradation pathways of reactions and identify the roles played by all involved species.[203]

Since STs are useful for detecting and identifying reactive species and intermediates formed during a reaction, a mechanistic pathway can be determined by adding scavengers to inhibit various reactive species and observing the impact on the reaction. This is done by adding a specific scavenger to a photocatalytic reaction where the scavenger selectively reacts with the targeted reactive species and efficiently scavenges them if present. Various scavengers are used to inhibit specific reactive species in photocatalytic reactions. For hydroxyl radicals, common scavengers include alcohols (however, the accuracy is questioned),[203,205–207] carboxylic acids,[208,209] or dimethylsulfoxide.[210] *p*-Benzoquinone and its derivatives or superoxide dismutase are primarily used for scavenging superoxide radicals[203,211] and 5,5-dimethyl-1-pyrroline-N-oxide (DMPO) is a good trap for detection.[212,213] Singlet oxygen is typically scavenged by sodium azide or 1,4-diazabicyclo [2.2.2]octane (DABCO),[203,214,215] and 2,2,6,6-tetra-methylpiperidine (TEMP) is a good trap for detection.[216] Ethylenediaminetetraacetic acid (EDTA), oxalic acid, alcohols, thiols, and amines serve as scavengers for holes.[217] Silver nitrate, copper chloride, iodates, and persulfates are used to scavenge electrons.[217] For instance, in a photocatalytic reaction, if the addition of *p*-benzoquinone significantly decreases the product, this indicates that superoxide radicals play a vital role in the reaction. Similarly, if the addition of silver nitrate reduces product formation, it indicates the involvement of photogenerated electrons. Overall, scavenger tests are instrumental in testing hypotheses related to photocatalytic reactions.

4.5 Product, by-product, and intermediate detection tests

Photocatalytic reactions can produce various products, by-products, and intermediates depending on the reaction conditions, the selectivity of the catalyst, and how long the reaction is conducted. Here we detail the products, by-products, and intermediates of common photocatalytic reactions and tests to identify them. For example, in photocatalytic water oxidation, the O_2 product can react with protons and electrons to form hydrogen peroxide.[218,219] Similarly in water splitting reactions, water can react with photogenerated holes to form hydrogen peroxide.[220,221] In photocatalytic CO_2 reduction, the products and intermediates can include carbon monoxide, formate, formaldehyde, alcohols, and hydrocarbons depending on the desired product.[222–224] Additionally, in aqueous conditions the reaction competes with HER.[224] Photocatalytic hydrogen peroxide production may generate water and oxygen from the decomposition of hydrogen peroxide, especially under light irradiation or with a suitable catalyst.[225–227] Photocatalytic aryl boronic acid oxidation generates boric acid,

$(BOH)_3$, as the by-product, and likewise oxidation of boronic esters yields $B(OH)(OR)_2$ as the by-product.[228–230] During photocatalytic sulfide oxidation reactions, sulfoxides and sulfones can be made.[231–233] To afford the sulfone, the sulfoxide is first made and is the intermediate oxidation state; however, sulfoxides are important products so oxidation to the sulfone is not always wanted. Common by-products and intermediates produced from photocatalytic benzyl alcohol oxidation include H_2O_2, which can form during advanced oxidation processes, and benzoic acid from overoxidation which can undergo esterification with benzyl alcohol to form benzyl benzoate.[234–236] In photocatalytic oxidative amine coupling reactions, typical intermediates are the imine and benzaldehyde derivatives, and the by-products include ammonia and H_2O_2, which can form during advanced oxidation processes.[237–239] In the photocatalytic degradation of organic pollutants, various intermediates and by-products are generated, including small organic acids such as acetic acid, oxalic acid, and formic acid, which result from the partial oxidation of larger organic molecules.[240] Additionally, aromatic compounds, including benzene derivatives and phenols, can be produced from the incomplete degradation of more complex aromatic compounds.[240]

With this in mind, it is important to verify these compounds *via* qualitative or quantitative tests to elucidate the reaction mechanism. As discussed in Sections 4.1–4.4, various analytical techniques can be utilized to detect products, by-products, and intermediates resulting from photocatalytic reactions. Another technique to characterize products and by-products in the post-reaction mixture is UV-Vis spectroscopy. Nosaka and Nosaka detail the many methods including UV-Vis, IR, EPR, chemiluminescence reactions, and fluorescence products to detect reactive oxygen species.[241] Additionally, detecting hydrogen peroxide through a coloration method can be done using iodide,[242] Ti^{4+},[243] or *N*,*N*-dimethyl-*p*-phenylenediamine[244] or by fluorescence methods.[241] This can also be done through titration or calibrated UV-Vis to obtain quantitative data, but colorimetric test strips can also be used for qualitative detection.[245] To illustrate, UV-Vis spectroscopy is one of the employed analytical techniques to confirm the formation of H_2O_2 in a photocatalytic reaction, as H_2O_2 can oxidize iodide ions (I^-) to form iodine (I_2), which subsequently generates tri-iodide (I_3^-) in the presence of excess iodide. I_3^- exhibits two characteristic peaks at approximately 300 and 350 nm in UV-Vis spectra.[241] Ammonia can be detected using a coloration method using Nessler's reagent or the indophenol blue method, or by ion chromatography.[246–248] Notably, Nessler's reagent can be used in any conditions but is very toxic and should be avoided if possible. The iodophenol blue method can only be used in neutral or basic conditions, and ion chromatography can only be done in acidic or neutral conditions. These methods all have their advantages and drawbacks, including varying accuracy and interference of other substances, but can easily be used in qualitative detection.[246–248] Safin *et al.* detailed a plethora of tests for analysing different functional groups and compounds including aldehydes, carboxylic acids, amines, esters, and sugars.[249] These simple coloration tests can easily be applied for qualitative detection of compounds post reaction. Boric acid can be detected using Azomethine H as a colorimetric reagent.[250] Undoubtedly, there are other quantitative and qualitative tests for photocatalytic reactions not described here.

5 Gearing COFs for photocatalysis – advantages of COFs and enrichment

5.1 Extending conjugation and UV-visible light absorption

In order for COFs to be eligible for photocatalytic application, they have to be able to absorb light especially in the ultraviolet (UV), visible light, and/or near IR spectrum. This is essential, as the harvesting of light is what initiates the formation of excitons, or electron–hole pairs, due to the excess energy gained. 2D COFs have an advantage with light absorption as the layered sheets stack and afford conjugation though π–π stacking. However, 1D and 3D COFs do not have this capability. Thus, in order to achieve a COF that has good light-absorbing properties, the electronic properties of the monomers and the chemical linkage that is used are imperative. For example, Jiang and co-workers synthesized a COF using triphenylene hexamine and *tert*-butylpyrene tetraone to form a phenazine-linked COF that exhibited extended π-delocalization.[57] This COF also showed utility for high on–off ratio photoswitches and photovoltaic cells. Bromley and Bredas conducted theoretical studies showing the importance of π-conjugation of COFs and the ability of monomer design to realize conjugation.[251,252] De Smet and co-workers even showed that the degree of methylation of monomer units affected the absorption and the band gap of the COF.[253] Van Der Voort and cohort explicitly detailed that extending the π-conjugation, through monomer and linkage, led to more efficient photocatalytic hydrogen peroxide production.[254] Zhang *et al.* illustrated that adding an alkynyl unit in the monomer led to broader visible-light absorption, narrower optical bandgaps, and much higher photocatalytic amine coupling performance than its counterpart without the alkyne.[255]

5.2 Band gap engineering

Beyond the absorption of light, band gap engineering of the COF is just as crucial. The band gap, or the HOMO–LUMO gap, is the energy difference between the valence band and the conduction band of the semiconductor. The band gap is imperative because as the COF is excited using light, an electron in the highest occupied molecular orbital (HOMO) is promoted into the lowest unoccupied molecular orbital (LUMO), which formally creates the hole in the HOMO and a charge is made and separated; this is called the photoexcitation state. Thus, the HOMO and LUMO energy levels of the COF are important, and are derived from the monomer units. In terms of photocatalysis, the HOMO energy level is essential, as the HOMO of the photocatalyst (*i.e.* the COF) must be lower than that of the substrate, so the oxidation reaction can occur at the photocatalyst with the photogenerated holes. Also, the LUMO

of the photocatalyst must be higher than the energy of the substrate, so the reduction reaction occurs at the substrate with the photogenerated electrons. Furthermore, to create the photoexcitation state a photon with equal or greater energy than that of the COF's band gap is needed, so a small band gap is ideal.

For example, Baeg and co-workers performed band gap engineering on imine-linked COFs with various amounts of alcohol substituents that could allow for ketoenamine tautomerization and push–pull effects.[256] This work demonstrated that push–pull effects had a direct effect on the band gap of the COF, illustrating that a lower band gap could yield better photocatalytic efficiency. Chen and cohort showed similar results using the same method for photocatalytic hydrogen evolution from water.[257] Qiu *et al.* synthesized various olefin-linked COFs with an increasing amount of alkynyl units in the aldehyde monomer.[258] They showed that by increasing the amount of alkynyl units, the band gap was reduced and showed superior photodegradation of bacteria and other contaminants. More commonly, band gap engineering is often achieved by using donor–acceptor systems.

5.3 Donor–acceptor systems

One challenge of photocatalysis is the fast recombination of the photogenerated electrons and holes. Donor–acceptor (D–A) systems are a unique way to address this problem. Donor sites localize holes and acceptor sites localize electrons to cause efficient charge separation. One key parameter for D–A systems to create this charge separation is that the HOMO must be centered on the donor and the LUMO must be centered on the acceptor, or a mix of the linkage and the acceptor, otherwise the holes and electrons will not be split across the material. Furthermore, the D–A system is an effective method to tune band gaps. In fact, the utilization of donor units and acceptor units to perform band gap engineering in polymers is not new.[10–12] One strategy to create a D–A system is to add electron-donating and withdrawing substituents, respectively. To increase the electron-withdrawing ability of the monomers, substituents such as nitriles, carbonyls, and nitro groups can be added as acceptors. To increase the electron-donating ability of the monomers, substituents such as amines, thiols, and alkoxy groups can be added as donors. Another strategy to create D–A systems is to construct the material using monomers based on electron-donating and accepting units (Fig. 11). Some donor monomer archetypes include pyrenes, thiophenes, fluorenes, carbazoles, phenothiazines, and triphenylamines. Some acceptor archetypes include triazines, diimides, diketopyrrolopyrroles, quinones, thiadiazoles, and oxadiazoles. The tunability and bottom-up design approach for COFs make them a perfect platform to incorporate these archetypes to make D–A systems.

For example, Liu and cohort synthesized two multicomponent D–A COFs using 1,3,5-tris-(4-formyl-phenyl)triazine (TFPT) and benzo[1,2-*b*:3,4-*b*′:5,6-*b*″]trithiophene-2,5,8-tri-carbaldehyde (BTT) monomers with either 1,4-phenyldiacetonitrile (PDAN) or 1,4-phenylenediamine (PDA) to create an olefin

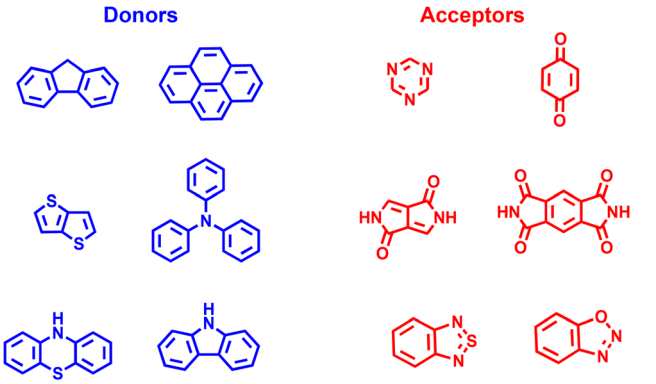

Fig. 11 Donor and acceptor moieties.

and imine-linked version, respectively.[259] They showed the D–A system had a small band gap and good charge separation which enabled high photocatalytic hydrogen evolution. Dong and co-workers synthesized an imine-linked D–A COF with a narrow band gap using benzo[*c*][1,2,5]thiadiazole and pyrene-based monomers for photocatalytic hydrogen evolution from water.[260] Thomas *et al.* exemplified a triphenylamine-linked triazine-based COF for photocatalytic cleavage of C=C bonds.[261] Jiang and co-workers engineered the linkages of D–A COFs using triphenylene donor and benzothiadiazole acceptor units for efficient photocatalytic hydrogen peroxide production from water and air.[262] The authors state that the D–A system allowed for fast photoinduced electron transfer, charge separation, localized oxidation and reduction active sites, and segregated columnar π-arrays for yielding and carrying of photogenerated charges. Thomas *et al.* explored constitutional isomerism in imine-linked D–A COFs based on triphenylamine and triazine units for photocatalytic hydrogen evolution.[263] Notably they showed that the bond polarization in D–A systems is important for the optical properties, band gap, and thus photocatalytic activity.

5.4 Photosensitizers

In photocatalysis and other photobased applications, light absorption is necessary for exciton formation and photocatalytic performance. Some materials do not harvest light efficiently, or have low absorption coefficients, or have competing processes such as fluorescence. Photosensitizers are a solution to a lack of light harvesting as they are compounds that have intense light absorption which can then transform light to energy and transfer this electronic excitation energy to the photocatalyst or a substrate in an antenna effect.[264] Common photosensitizers include organic dyes (*i.e.* methylene blue, Nile Blue, and acridine orange), fluoresceins, rhodamines, azulenes, porphyrins, chlorins, phthalocyanines, ruthenium bipyridine complexes, iridium phenylpyridine complexes, and rhenium bipyridine carbonyl complexes (Fig. 12). Even though COFs have a high degree of π-conjugation and wide-ranging UV-visible light absorption, they can suffer from poor absorption coefficients so photosensitizers can be added to increase

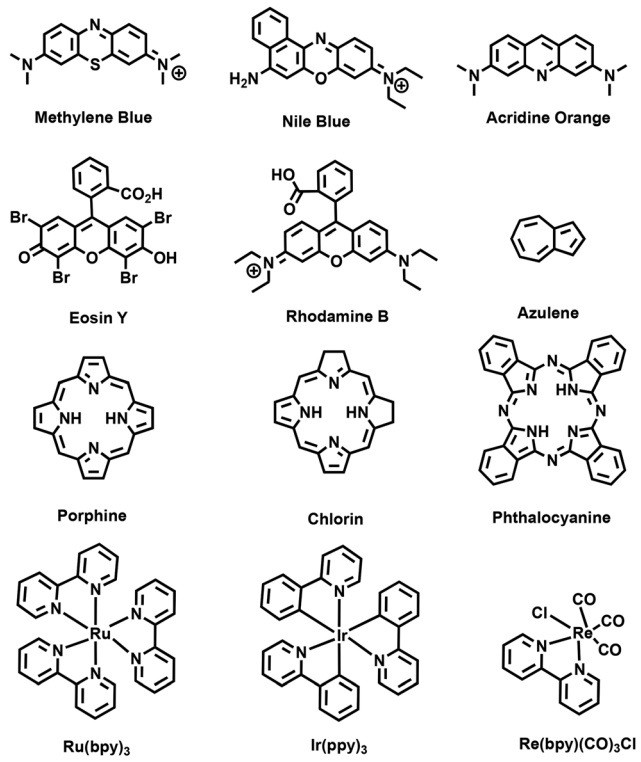

Fig. 12 Common photosensitizers.

the light absorption efficacy and overall efficiency of the system.

For instance, Yuan *et al.* synthesized a boroxine-linked COF and doped it with phthalocyanine-based photosensitizers for effective photodynamic therapy.[265] Liao and Hu constructed a vinylene-linked COF to host a p-type thiophene-based photosensitizer, g2T-T, to perform photocatalytic hydrogen evolution.[266] Lu and co-workers synthesized Pd-doped TpPa-1 COF which was sensitized by Eosin Y dye, which showed 10 times higher photocatalytic hydrogen evolution than that of Pd/C.[267] Wu *et al.* made a porphyrin-bipyridine-based COF that could host $Ru(bpy)_3Cl_2$ photosensitizer for photocoupled electroreduction of carbon dioxide.[268] These represent just a handful of examples of COFs utilizing photosensitizers.

5.5 Sacrificial reagents

Sacrificial reagents are useful in photocatalytic reactions in order to scavenge holes or electrons to prevent recombination and thus achieve high catalytic efficacy.[217] Most commonly used are electron donors, or hole scavengers. A hole scavenger is oxidized irreversibly with the photogenerated holes to destroy them, and importantly should form a by-product that does not interfere with the reaction. This means that electron donors are fully expended during the course of the reaction, and stoichiometric or continuous addition is required to perform the photocatalytic reaction efficiently. Some common electron donors include potassium iodide, triethylamine (TEA), triethanolamine (TEOA), 1,3-dimethyl-2-phenylbenzimidazoline (BIH), 1-benzyl-1,4-dihydronicotinamide (BNAH), ascorbic acid, oxalate, ethylenediaminetetraacetic acid (EDTA), and thiols (Fig. 13). Electron acceptors, or electron scavengers, are used to destroy photogenerated electrons. Electron scavengers are reduced irreversibly and need to be added in stoichiometric amounts or continuously added just like hole scavengers. However, most photocatalytic reactions use the photogenerated electrons to promote the reaction, so electron scavengers are mainly used to study the mechanism and for proof of electron and hole separation. Common electron acceptors include silver nitrate, copper chloride, potassium chromate, sodium persulfate, sodium iodate, potassium iodate, and oxygen.

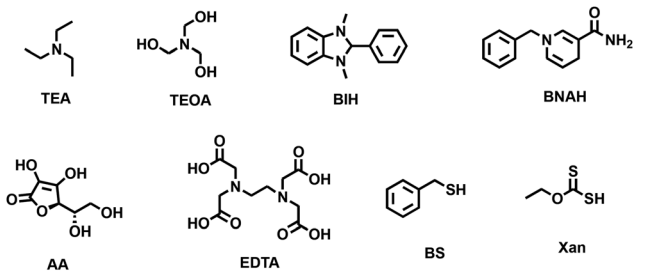

Fig. 13 Common sacrificial electron donors.

5.6 Doping

Doping a material with elements, compounds, or nanoparticles to enhance its optical properties and electronic behaviour is an effective approach for enhancing photocatalytic activity in polymers.[269] For example, Pang and cohort synthesized COFs and embedded them with CuSe[270] or Ag_2Se[271] nanoparticles for phototherapy. Su *et al.* constructed crystalline CTFs and doped them with elemental sulfur for photocatalytic hydrogen evolution using water.[272] They demonstrated that the sulfur-doped CTFs showed both greater photocatalytic performance and stability. Bi *et al.* synthesized a β-ketoenamine COF, TpMa, and combined it with CdS for photocatalytic hydrogen peroxide production.[273] The material showed 2.5 times higher H_2O_2 production than the pristine COF and 4 times higher than CdS alone. Zhang and co-workers synthesized TpPa-2-COF and doped it with α-Fe_2O_3 for photocatalytic hydrogen evolution.[274] The material showed 53 times higher production than the pristine COF, and the authors showed that this was due to the efficient charge separation from transfer of photogenerated electrons from the conduction band of the α-Fe_2O_3 to the valence band of the COF. Zhang *et al.* showed that TpTa-COF could encapsulate $Ti(O^nBu)_4$ and be converted to Fe–TiO_2 nanoparticles (Fig. 14).[275] This Fe–TiO_2@COF material was highly efficient at photocatalytic degradation of methylene blue dye. Islam and co-workers synthesized TP-TAPM COF and doped it with TiO_2 for highly efficient photoreduction of CO_2 to CH_3OH and N_2 to NH_3.[276] These provide just a small assortment of examples to show the utility of doping in COFs for photoenhancement.

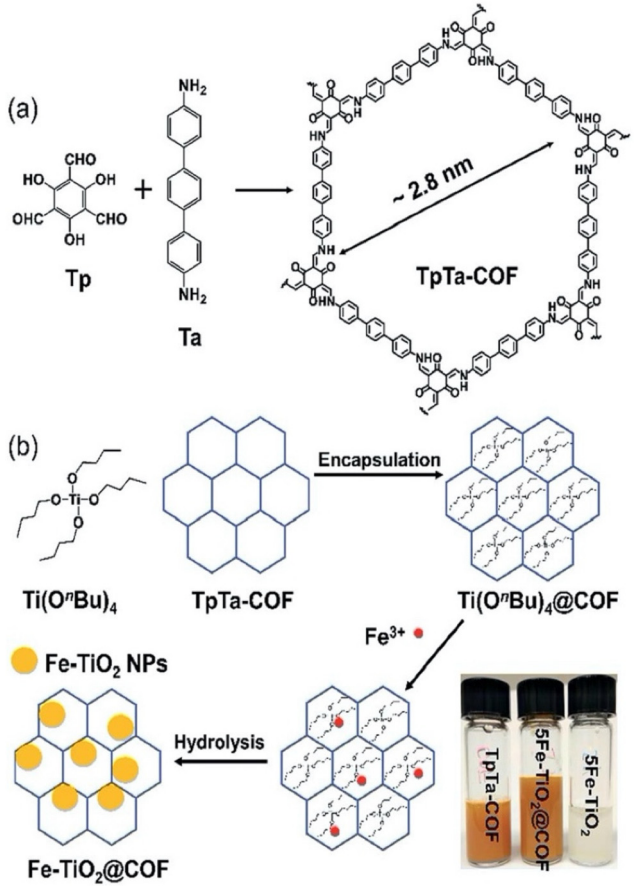

Fig. 14 Schematic presentation of the synthesis of TpTa-COF (a) and Fe–TiO_2@COF (b).[275] Reproduced with permission from ref. 275. Copyright 2019, The Royal Society of Chemistry.

5.7 Polymeric composites and hybrid materials

COFs provide a unique platform for constructing composites or hybrid materials due to their porous nature. By combining two or more materials, the chemical, optical, and electrical properties can be enhanced. Some examples of COF composites include COF@COF, polymer@COF, carbon allotrope nanostructure (CAN)@COF, and metal organic framework (MOF)@COF. For instance, Li *et al.* constructed a triazine-based imine-linked COF (TATF-COF) and combined it with a perylene diimide urea polymer (PUP).[277] The PUP@COF material showed 3.5 times higher photocatalytic hydrogen production than that of the pure TATF-COF due to charge-transfer channels and prolonged exciton lifetimes. Pan and co-workers fabricated a melamine sponge COF hybrid, and the MS@TpTt material exhibited excellent photodegradation of tetracycline antibiotics.[278] Lu and co-workers produced a Co-porphyrin based COF, COF-366-Co, and covalently anchored it on graphene oxide (GO).[279] The GO-COF-366-Co composite was used for photoreduction of carbon dioxide and showed about 4 times higher activity than the pristine COF. This was corroborated by photoelectrical experiments illustrating the higher charge separation and transfer of the composite. Wang and

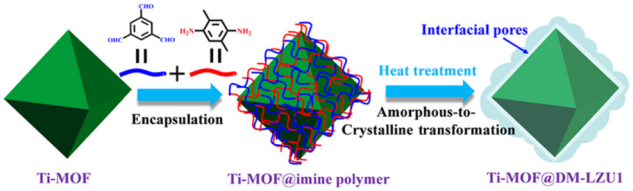

Fig. 15 Two-step method to prepare Ti-MOF@DM-LZU1.[282] Reproduced with permission from ref. 282. Copyright 2020, American Chemical Society.

cohort synthesized a TpBD COF and fabricated it on carbon nanotubes for efficient photodegradation of mordant black 17 dye.[280] Zhang *et al.* synthesized NH_2-MIL-68 and coated it with TPA-COF, and the NH_2-MIL-68@TPA-COF showed high photocatalytic degradation of rhodamine B dye.[281] Kim and Sun constructed NH_2-MIL-125(Ti), or Ti-MOF, encapsulated Pt nanoparticles in it, forming Ti-MOF@Pt, and then drop-cast DMLZU1 COF onto it giving Ti-MOF@Pt@DMLZU1 (Fig. 15).[282] This hybrid material was used for photohydrogenation of olefins and showed quantitative conversion in near perfect selectivity in 40 min using only 1 atm of H_2 for styrene. Zang *et al.* performed similar experiments using a Pd@Ti-MOF@TpTt hybrid for photocatalytic hydrogenation of nitroarenes.[283] Interestingly, Yan *et al.* constructed a MOF@COF@GO composite, UiO-66-NH_2/TAPT-TP-COF/GO, for photocatalytic hydrogen evolution.[284] These examples provide a small demonstration of the ability to construct composite/hybrid materials using COFs to boost photocatalytic performances.

6 Photocatalytic applications

6.1 Hydrogen evolution

High population growth significantly increases energy demand, making energy shortages one of the most pressing global challenges.[285] This issue requires a multifaceted approach for ensuring a sustainable energy supply while minimizing the environmental impact. Hydrogen production under visible-light irradiation, often called photocatalytic hydrogen evolution, is an area of significant interest in renewable energy research.[286–288] COFs are promising materials for photocatalytic hydrogen production due to their porosity, structural designs, visible light harvesting, and chemical stability.[24] COFs synthesized from porphyrins, triazines, and pyrene building blocks with extended π-conjugated planar structures have been extensively studied for photocatalytic hydrogen evolution.[24] Indeed, one of the most fascinating properties of COFs is their structural tunability,[289,290] enabling unique designs. Numerous studies have concentrated on COF-based photocatalysts for H_2 evolution, demonstrating that altering their building blocks,[291,292] functional groups[293,294] and linkages[295–299] can enhance photocatalytic performance. The mechanism of photocatalytic H_2 evolution using COFs has also been well developed.[24]

In 2014, the Lotsch group introduced the first COF photocatalyst, TFPT-COF, for hydrogen evolution.[300] The crystalline hydrazone-based TFPT-COF demonstrated a photocatalytic hydrogen evolution rate of 1970 μmol g^{-1} h^{-1} under visible light irradiation (300 W Xe lamp) with 2.2 wt% Pt as the cocatalyst and 10 vol% TEOA as the electron donor, and a smaller 230 μmol g^{-1} h^{-1} using sodium ascorbate as the electron donor. Under identical standard conditions, TFPT-COF/Pt demonstrated superior performance compared with the results obtained with other highly effective photocatalytic systems, specifically a Pt-modified amorphous melon, g-C_3N_4, synthesized as described in the literature,[301] and crystalline poly (triazineimide). Notably, the TFPT-COF loses crystallinity after photocatalysis but can be reconverted into the crystalline material by resubjecting it to the initial synthesis conditions.

In 2022, the Li group examined a series of COFs synthesized using 2,4,6-tris(4-aminophenyl)-1,3,5-triazine with 1,3,5-triformylbenzene, 2,4,6-triformylphloroglucinol, 2,4,6-triformylphenol, and 2,4,6-triformylresorcinol, respectively. These were denoted as COF-OH-*n* (*n* = 0–3), representing the number of –OH groups.[257] COF-OH-0 and COF-OH-3 were synthesized according to the procedure from the literature.[302,303] The varying degrees of proton tautomerism in COF-OH-*n*, due to the different numbers of β-ketoenamine linkages in their structures, regulated the visible light absorption ability, band gap, and band edge positions. Photocatalytic hydrogen evolution experiments were conducted using visible light (300 W Xe lamp), ascorbic acid as the sacrificial agent, and 1 wt% Pt as the cocatalyst. Among the COF-OH-*n* series, COF-OH-3 exhibited the highest hydrogen evolution rate of 9.89 mmol g^{-1} h^{-1}. This superior performance was attributed to the irreversible proton tautomerism in COF-OH-3, which resulted in the most favourable photoelectronic properties. The apparent quantum yield of COF-OH-3 was 0.15% at 420 nm.

Recently, metalated or metal-associated COFs have been employed as photocatalysts for H_2 evolution.[304,305] Metal ions can influence the charge carrier dynamics within the resulting COF frameworks. Recently, a series of planar porphyrin-based MPor-DETH-COFs (M = H_2, Co, Ni, and Zn) were designed and synthesized through the condensation reaction of metalated porphyrinic aldehydes with 2,5-diethoxyterephthalohydrazide (DETH).[305] The visible-light-driven hydrogen production by these COF photocatalysts was examined under visible light using a 300 W Xe lamp in the presence of Pt and TEOA, with Pt acting as the cocatalyst and TEOA as the sacrificial reagent. Among the MPor-DETH-COFs, ZnPor-DETH-COF exhibited the highest hydrogen production rate of 413 μmol g^{-1} h^{-1}. H_2Por-DETH-COF, CoPor-DETH-COF, and NiPor-DETH-COF had rates of 80, 25, and 211 μmol g^{-1} h^{-1}, respectively. These findings indicated an increasing driving force from charge carrier dynamics, as supported by transient emission decays and photocurrent tests. ZnPorDETH-COF had an apparent quantum yield of 0.32% at 450 nm. Notably, when the incident wavelength was above 500 nm no hydrogen was produced.

COFs with donor–acceptor (D–A) moieties have been widely utilized for photocatalytic H_2 evolution.[306] Recently, the Dong group designed and synthesized a novel imine-linked COF, DABT-Py-COF, by condensing a newly constructed donor–acceptor–donor (D–A–D) type monomer, 4,4′,4″,4‴-(benzo[*c*][1,2,5]thiadiazole-4,7-diylbis(9,9-dimethyl-9,10-dihydroacridine-10,2,7-triyl))tetrabenzaldehyde, with 1,3,6,8-tetrakis(4-aminophenyl)pyrene.[307] By optimizing the reaction conditions using an aqueous medium containing ascorbic acid as the sacrificial electron donor, DABT-Py-COF as the photocatalyst, and Pt as the cocatalyst under visible light irradiation (300 W Xe lamp), they achieved a hydrogen evolution rate of 5458 μmol g^{-1} h^{-1}. Without Pt cocatalyst, a rate of 299 μmol g^{-1} h^{-1} was achieved. The remarkable performance of DABT-Py-COF was attributed to its high crystallinity, permanent porosity, broad light absorption range, and exceptional chemical stability. Notably, after five cycles, the DABT-Py-COF had a decrease in crystallinity.

Thomas and co-workers have recently explored COFs and COF films with uniquely tunable band gaps and optoelectronic properties for photocatalytic hydrogen evolution.[308] They investigated the photocatalytic performance of low band gap COFs constructed by condensing the extended π-conjugated 9,10-bis(4-aminophenylethynyl)anthracene (AntT) with benzene-1,3,5-tricarbaldehydes containing varying numbers of hydroxy groups on the aldehyde units (*n* = 0, 1, 2, 3). This resulted in synthesizing AntTTF, AntTMH, AntTDH, and AntTTH, respectively. The AntT monomer functioned as the photoabsorber, while the β-ketoenamine linkage preserved the planarity of the system through intramolecular hydrogen bonding. AntTTF and AntTTH were synthesized according to the procedure reported in the literature.[309] Additionally, thin films of the powder COFs were synthesized, capitalizing on their numerous advantages in photocatalytic applications, such as low light scattering and reusability. The number of hydroxy groups on the 1,3,5-triformylbenzene linker significantly influenced the properties of the COFs. AntTDH, the COF prepared from the linker with two hydroxy groups, showed the lowest band gap, exhibiting efficient charge separation and migration due to the formation of J-type aggregates. Photocatalytic hydrogen evolution was performed under visible light (λ > 420 nm, 300 W) with 2 wt% Pt cocatalyst and ascorbic acid as the sacrificial electron donor. AntTDH achieved the highest HER of 8.4 ± 0.5 mmol g^{-1} h^{-1} in the powder state. Interestingly, in the COF films, a steady increase in the hydrogen evolution rate was observed with an increasing –OH group. The COF film with the most hydroxy groups, AntTTH, gave the best HER of 1.6 ± 0.2 mmol m^{-2} h^{-1} due to heightened charge carrier mobility (Fig. 16). Notably, post-catalysis, both the COF films and powders displayed a partial loss of crystallinity.

Using saddle-shaped cyclooctatetrathiophene derivatives as building blocks, the Wang group has recently developed fully conjugated 3D COFs for metal-free photocatalytic hydrogen evolution.[310] Through Schiff-base condensation, they synthesized a series of fully conjugated 3D COFs using COThP-CHO, which was synthesized from the literature method,[311] with benzidine (BD), 3,7-diaminodibenzo[*b*,*d*]thio-

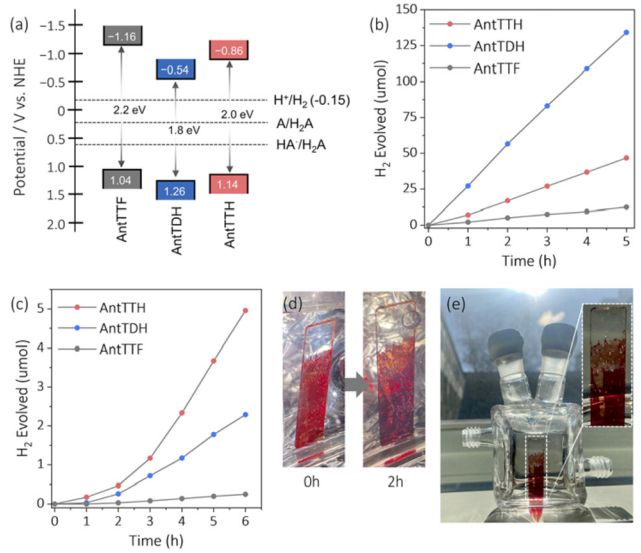

Fig. 16 (a) Calculated band position and band gap of the COF powders *vs.* normal hydrogen electrode (NHE) along with the potential of H^+/H_2 and oxidation potentials of L-ascorbic acid, $HA^{\bullet}/H_2A$ and A/H_2A at pH 2.6. Time course for photocatalytic HER under visible light (≥420 nm) of (b) COF powders (3 mg of COF with 2 wt% Pt) and (c) COF films (with 2 wt% Pt) in 16 mL 0.1 M ascorbic acid aqueous solution at pH 2.6. (d) Photograph of AntTTH film over quartz at different time intervals of photocatalytic reaction showing the formation of H_2 gas bubbles. (e) The image of the AntTTH film is illuminated with diffused sunlight inside a photocatalytic reactor with the corresponding enlarged image showing the formation of H_2 gas bubbles.[308] Reproduced with permission from ref. 308. Copyright 2024, Royal Society of Chemistry.

phene-5,5-dioxide (SA), 2,2′-dimethyl[1,1′-biphenyl]-4,4′-diamine (MBD), and 3,3′-dimethylbiphenyl-4,4′-diamine (DMB), resulting in BUCT-COF-20, -21, -22, and -23, respectively. The photocatalytic reactions for H_2 production were conducted under visible light irradiation (λ > 400 nm, 300 W) using 5 mg of photocatalyst in water, 2.5 μL (8 wt%) H_2PtCl_6 as cocatalyst, and 0.1 M ascorbic acid as an electron donor. BUCT-COF-20 demonstrated the highest HER of 40.36 mmol g^{-1} h^{-1}, approximately three times higher than BUCT-COF-21, which had a HER of 14.11 mmol g^{-1} h^{-1}. BUCT-COF-22 achieved a HER of 18.80 mmol g^{-1} h^{-1}, while BUCT-COF-23 exhibited the lowest performance at 4.33 mmol g^{-1} h^{-1}. Under similar reaction conditions, the performance of BUCT-COF-20 was compared with that of the non-conjugated COF-320. COF-320 produced a significantly lower hydrogen evolution rate of 0.79 mmol g^{-1} h^{-1}. BUCT-COF-20 showed the highest apparent quantum yield of 2.58% at 450 nm, and with lower AQY of 2.34%, 1.88%, 1.14%, and 0.73% at 400 nm, 500 nm, 550 nm, and 600 nm, respectively. The exceptional performance of BUCT-COF-20 can be attributed to its D–A electronic structures, porosity, hydrophobicity, and conjugated structure.

6.2 Water oxidation

Water oxidation for oxygen evolution involves a complex four-electron redox process in the rate-determining step of overall water splitting. This process includes the cleavage of the O–H bond, the formation of the O–O bond, and a large overpotential with slow O–O formation kinetics.[312–314] As a result, there has been limited research on using COFs as photocatalysts for photocatalytic water oxidation. Among the COFs used for oxygen evolution are bipyridine-containing COFs due to their capacity to form chelate complexes with transition metals.

One of the most recent reports of a bipyridine-containing COF for photocatalytic water oxidation is from the Li group.[315] They used a triazine-based COF, TAPT-Bpy-COF, synthesized by a Schiff-base condensation from 2,4,6-tris(4-aminophenyl)-1,3,5-triazine and 2,2′-bipyridyl-5,5′-dialdehyde. TAPT-Bpy-COF was coordinated with Co, Fe, and Ni, resulting in TAPT-Bpy-COF-Co-3, TAPT-Bpy-COF-Fe-3, and TAPT-Bpy-COF-Ni-3, respectively. The photocatalytic water oxidation of these metal-coordinated COFs under light illumination ($\lambda \geq$ 420 nm, 300 W Xe lamp) was carried out in a silver nitrite sacrificial system. Among them, TAPT-Bpy-COF-Co-3 achieved the highest oxygen evolution rate of 483 μmol g^{-1} h^{-1} with an efficient apparent quantum efficiency (AQE) of 7.6% at 420 nm. The performance of TAPT-Bpy-COF-Co-3 is higher than most bipyridine-containing COFs. HR-STEM-HADDF images confirmed cobalt coordination with the bipyridine units within the framework structure. TAPT-Bpy-COF-Co-3 benefits from its broad visible light absorption range, high surface area, well-ordered structure, and improved charge separation.

Studies have demonstrated that crystalline COFs exhibit superior photocatalytic water oxidation performance compared with their amorphous counterparts, owing to their highly ordered arrangement of functional units.[316,317] As a proof of concept, in 2022, Würthner *et al.* successfully integrated Ru(bda)-based (bda = 2,2′-bipyridine-6,6′-dicarboxylate) dialdehyde into a 3D ordered COF.[318] This was achieved through imine condensation between the dialdehyde and tetra-(4-anilyl)methane, forming either crystalline or amorphous 3D imine polymers, depending on the solvents used, referred to as Ru(bda)-COF or Ru(bda)-polymer, respectively. The photocatalytic water oxidation was studied using Ru(bda) polymers, with $[Ru(bpy)_3]Cl_2$ serving as the photosensitizer (PS) and sodium persulfate ($Na_2S_2O_8$) as the sacrificial electron acceptor (SEA). The SEA first oxidizes the photogenerated PS* to PS^+, which further oxidizes the Ru water oxidation catalyst (WOC) until it reaches the crucial Ru^{5+} state. For the photocatalytic water oxidation, measurements were performed at $\lambda \geq$ 380 nm using a 150 W Xe lamp. At a low catalyst loading of 0.1 g L^{-1}, Ru(bda)-COF achieved an initial rate of 10.4 μmol L^{-1} s^{-1}, over 20 times higher than the 0.5 μmol L^{-1} s^{-1} rate of Ru(bda)-polymer. This disparity in performance is attributed to differences in their mechanistic pathways. During the O–O bond formation process, Ru WOCs can follow two primary mechanistic pathways: water nucleophilic attack (WNA) or the interaction of two highly oxidized Ru-oxyl radicals (I2M).[319,320] Ru(bda)-COF photochemical water oxidation follows the I2M pathway and is second order in COF concentration, suggesting that two COF particles are involved in the rate-determining step (RDS). Extensive mechanistic studies, including H/D kinetic isotope

effect (KIE) analysis, indicated that the O–O bond formation in Ru(bda)-polymer follows the WNA pathway. The limited access to the Ru(bda) units at the disoriented polymer surface hinders the efficient dimerization of activated catalysts. Consequently, this restricts the water oxidation catalysis to the less efficient WNA mechanism in Ru(bda)-polymer.

The Wang group has recently examined the effectiveness of boranil COFs (N and O-moiety chelated difluoroboron complexes) in photocatalytic water oxidation reactions.[321] Initially, they synthesized a series of metalated porphyrin-based COFs, M-TAPP-COFs (where M = Ni, Zn, Co, Mn), through the Schiff-base condensation of 5,10,15,20-tetrakis(4-aminophenyl)porphyrin metal[II] (M-TAPP) and 2,5-dihydroxyterephthalaldehyde.[322] Subsequently, they achieved boranil-functionalized fully π-conjugated ordered D–A COFs, M-TAPP-COF-BF_2, by post-synthetic modification of M-TAPP-COFs using an excess of $BF_2{\cdot}Et_2O$.[323] The photocatalytic water oxidation experiments were conducted in aqueous solution with 5 mg of the photocatalyst (Ni-TAPP-COF, Ni-TAPP-COF-BF_2, Zn-TAPP-COF-BF_2, Co-TAPP-COF-BF_2, and Mn-TAPP-COF-BF_2) and $AgNO_3$ as a sacrificial electron acceptor under light irradiation (300 W Xe, AM 1.5G cut-off filter) at 10 °C. The order of photocatalytic oxygen evolution rates was observed as Ni-TAPP-COF-BF_2 > Zn-TAPP-COF-BF_2 > Co-TAPP-COF-BF_2 > Mn-TAPP-COF-BF_2 > Ni-TAPP-COF. Notably, Ni-TAPP-COF-BF_2 exhibited the highest performance with 1404 μmol g^{-1} h^{-1}, significantly surpassing the pristine Ni-TAPP-COF, 123 μmol g^{-1} h^{-1}. Both experimental and theoretical findings indicated that the push/pull (metalloporphyrin/BF_2) mechanism and π-conjugation that is well-regulated are crucial for photoabsorbing properties. The apparent quantum yield of Ni-TAPP-COF-BF_2 was 1.27% at 450 nm.

Yan and co-workers have recently designed a coordinated enamine-based COF using cobalt dichloride for photocatalytic oxygen evolution through water oxidation.[324] Initially, TpBPy was synthesized *via* Schiff base condensation of 2,4,6-trihydroxybenzene-1,3,5-tricarbaldehyde (Tp) and [2,2′-bipyridine]-5,5′-diamine (BPy) under solvothermal conditions. Subsequently, $CoCl_2$ was incorporated at the bipyridine sites in an ethanol solution to form $CoCl_2$–TpBPy. Photocatalytic O_2 evolution analysis was conducted using a closed glass apparatus with 10 mg of photocatalyst mixed in $AgNO_3$ solution (as a sacrificial reagent), under 300 W xenon lamp illumination (λ = 400 nm) at a temperature of 10 °C. After 1 h, $CoCl_2$–TpBPy demonstrated an O_2 evolution rate of 1 mmol g^{-1} h^{-1}, while TpBPy exhibited almost no O_2 evolution. $CoCl_2$–TpBPy had an apparent quantum yield of 1.34% at 425 nm. Using a wavelength of 460 nm yielded about 700 μmol g^{-1} h^{-1}, and at 500 nm yielded about 200 μmol g^{-1} h^{-1}. Interestingly, $MnCl_2$ or $RuCl_3$ versions produced no yield. *In situ* XPS and EPR analyses revealed that high-valence cobalt states were important for water oxidation (Fig. 17). The coordination of $CoCl_2$ into TpBPy maintained the structural integrity and the characteristics of charge recombination. Notably, the COF lost its crystallinity post-catalysis.

The Wang group recently synthesized an ionic-type COF, CoTPP-$CoBpy_3$, which included a tetraphenyl porphyrin co-

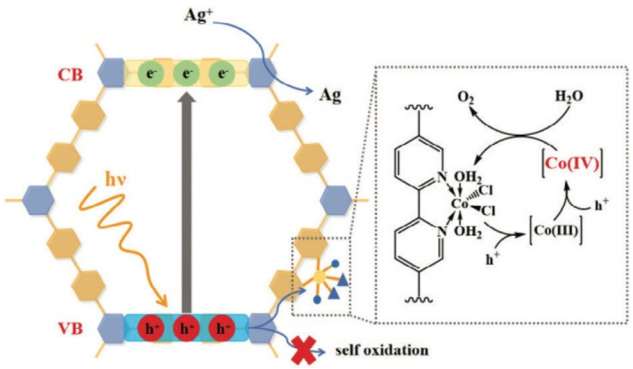

Fig. 17 Proposed mechanism for the photocatalytic water oxidation process facilitated by $CoCl_2$–TpBPy.[324] Reproduced with permission from ref. 324. Copyright 2024, John Wiley and Sons.

ordinated cobalt (CoTPP) and a bipyridine coordinated cobalt complex $\{[Co^{II}(bpy)_3](OAc)_2\}$ for photocatalytic water oxidation.[325] This unique COF was created using a one-pot condensation reaction involving 5,10,15,20-tetrakis(4-aminophenyl)-21*H*,23*H*-porphine, 2,2′-bipyridyl-5,5′-dialdehyde, 2,2′-bipyridine, and $Co(OAc)_2{\cdot}4H_2O$. High-resolution cryo-transmission electron microscopy (cryo-TEM) revealed that CoTPP-$CoBpy_3$ COF had a large-sized morphology of over 2 μm, ultra-thin nanosheets with a thickness of approximately 1.25 nm, and high crystallinity. The photocatalytic water oxidation was tested by dispersing 5 mg of the photocatalyst in aqueous $AgNO_3$ solution and illuminating it with a 300 W xenon lamp with an AM 1.5G cut-off filter. After 1 hour, the photocatalytic oxygen production rate reached 7323 μmol g^{-1} h^{-1}. CoTPP-$CoBpy_3$ COF gave an apparent quantum yield of 4.65% at 450 nm. This performance was attributed to the unique properties of CoTPP-$CoBpy_3$.

6.3 Water splitting

Hydrogen production through water splitting under visible-light irradiation is an area of significant interest in renewable energy research. This method uses solar energy to drive the splitting of water molecules into hydrogen and oxygen, offering a clean and sustainable way to produce hydrogen fuel. This can be challenging due to critical thermodynamics, slow kinetics, dissolved oxygen, reverse and side reactions, *etc.*[326,327] Limited research has been conducted on using COFs for hydrogen production through water splitting under visible-light irradiation.[328] Transition metals are mostly used as cocatalysts in the process. The photocatalytic mechanism of water splitting has been previously explored using COFs.[328]

Interestingly, in 2020, Chen and co-workers explored the impact of halogens on a 2D COF for hydrogen production through water splitting under visible-light irradiation by altering the photoactive unit with halogens.[329] Photoactive benzothiadiazole (BT) units were strong electron acceptors, facilitating efficient intramolecular charge transfer through alternating D–A skeletons. A series of 2D COFs, Py-XTP-BT-COFs (X = H, F, or Cl), was synthesized by polycondensation of 4,4′,4″,4′

″-(pyrene-1,3,6,8-tetrayl)tetrabenzaldehyde (Py-CHO) with terphenyl-based diamines (XTP-BT-NH_2) featuring fluorinated, chlorinated, or non-halogenated BT units under solvothermal conditions. Photocatalytic water-splitting experiments were performed under visible light irradiation (λ > 420 nm) using ascorbic acid as the sacrificial reagent and without a cocatalyst. Py-ClTP-BT-COF, Py-FTP-BT-COF, and Py-HTP-BT-COF achieved HER rates of 44.00, 15.8, and 6.00 μmol h^{-1}, respectively, demonstrating that chlorination and fluorination of the Py-HTP-BT-COF skeleton can enhance photocatalytic activity. Using the same conditions with 5 wt% Pt cocatalyst, Py-ClTP-BT-COF, Py-FTP-BT-COF, and Py-HTPBT-COF showed HER rates of 177.50, 57.50, and 21.56 μmol h^{-1}, respectively. The AQE of Py-ClTP-BT-COF reached 8.45% at 420 nm, one of the highest values reported for COF-based photocatalysts. These findings indicate that halogenation in the BT unit is crucial in modulating the electronic structures of BT-COFs owing to the high electronegativity of chlorine and fluorine atoms. Based on DFT calculations, the adjustment of halogens in the photoactive BT units can effectively inhibit charge recombination and notably lower the energy barrier linked to the creation of H intermediate species (H*) on the polymer surface.

Recently, Zhao and co-workers reviewed functional regulation of COFs for photocatalytic water splitting.[330] A prime example comes from the Li group where they synthesized COF-SCAU-2 using 5′-(4-formylphenyl)-[1,1′:3′,1″-terphenyl]-4,4″-dicarbaldehyde (TB) and 2,7-diamino-9-fluorenone (F), and this was mechanically exfoliated to afford UCOF-SCAU-2.[331] They took these COFs and tested them for photocatalytic water splitting under visible-light irradiation (300 W Xe lamp) with Pt as cocatalyst and ascorbic acid as a sacrificial reagent. The hydrogen evolution rate for COF-SCAU-2 was 3.63 mmol h^{-1} g^{-1}, and 35.61 mmol h^{-1} g^{-1} for UCOF-SCAU-2. The apparent quantum yield of UCOF-SCAU-2 was 10.23% at 420 nm. When tested for overall water splitting COF-SCAU-2 showed no activity, but UCOF-SCAU-2 exhibited hydrogen and oxygen evolution rates of 0.046 and 0.021 mmol h^{-1} g^{-1}, respectively. However, after five recycles the rates fall to almost half.

In 2023, Lan and co-workers explored a series of β-ketoenamine COFs for photocatalytic water splitting.[332] They synthesized TpBD-COF, TpBpy-2-COF, and TpBpy-COF through reversible Schiff base reaction and irreversible enol-to-keto tautomerization. These COFs were then modified and exfoliated through a "top-down" process to create TpBD-NS, TpBpy-2-NS, and TpBpy-NS. To incorporate a cocatalyst, ultra-small Pt nanoparticles (NPs) were generated *in situ* within the pores of the COFs, resulting in the non-bipyridine Pt@TpBD-NS, and the bipyridine (Bpy)-containing Pt@TpBpy-NS and Pt@TpBpy-2-NS photocatalysts. The reactions were conducted in quartz tubes within a sealed system containing 15 mg of catalyst in H_2O and using sodium ascorbate as the sacrificial electron donor. For performance comparison, the non-Bpy Pt@TpBD only performed the H_2 half reaction, whereas the Bpy-containing COFs, Pt@TpBpy-NS and Pt@TpBpy-2-NS, demonstrated overall water splitting, producing both H_2 and O_2. Under visible light, Pt@TpBpy-NS achieved optimal production rates of 9.9 μmol of H_2 and 4.8 μmol of O_2 in 5 hours while Pt@TpBpy-2-NS produced 3.1 μmol of H_2 and 1.4 μmol of O_2. With experimental and theoretical calculations, this work proved that the position of the N-sites within the Bpy (Fig. 18), the nanosheet morphology of the COFs, and the incorporation of ultra-small Pt nanoparticles within the COF pores were crucial factors for enhancing water-splitting activity. An apparent quantum yield of 2.8% was measured at 450 nm for Pt@TpBpy-NS.

Xu and co-workers have recently explored two types of π-conjugated COFs with the same donor–acceptor structure but different linkages for metal-free photocatalytic water splitting.[333] The sp^2c-Py-BT COF and the imine-Py-BT COF were composed of the electron-donating pyrene (Py) unit and the electron-accepting BT unit, formed through Knoevenagel condensation and Schiff base reaction, respectively. The photocatalytic reactions were conducted by mixing the photocatalyst in pure water without any cocatalyst or sacrificial agent, under visible light irradiation (λ > 420 nm, 300 W Xe lamp). The sp^2c-Py-BT COF produced H_2 and O_2 in a near 2 : 1 stoichiometric ratio for overall water splitting, with average production rates of 17.2 and 8.1 μmol h^{-1} g^{-1}, respectively. Under the same conditions, the imine-Py-BT COF could not reach the overall water-splitting reaction. When adding in triethanolamine, the H_2 rate increased to 891.5 μmol h^{-1} g^{-1}, and when adding in $AgNO_3$, the O_2 rate increased to 21.2 μmol h^{-1} g^{-1} for sp^2c-Py-BT COF. Furthermore, when adding Pt and $Co(OH)_2$ cocatalysts, sp^2c-Py-BT COF had increased production rates for H_2 and O_2 to 71.3 and 30.8 μmol h^{-1} g^{-1}, respectively. Mechanistic studies indicated that the cyano-vinylene linkage

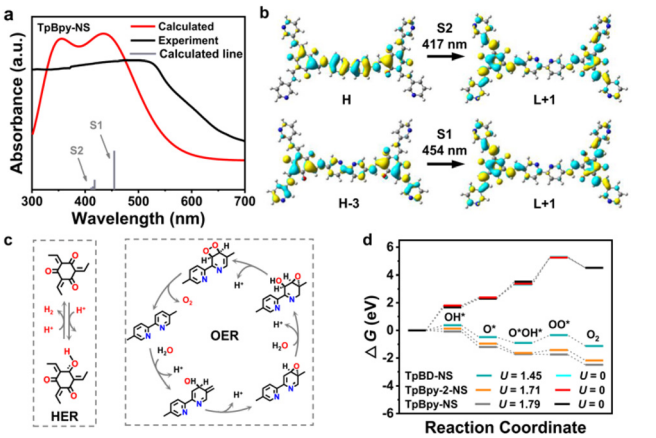

Fig. 18 DFT calculations and proposed schematic mechanism of TpBpy-NS. (a) UV-Vis absorption spectra of TpBpy-NS compared with TD-DFT calculated fragment. (b) The TD-DFT calculated electronic transition of TpBpy-NS. (c) The possible process of HER on Tp segment and OER *via* dual-site process on Bpy segment in TpBpy-NS. (d) The comparison of calculated Gibbs free energy change for C2d paths of OER for TpBD-NS, TpBpy-2-NS and TpBpy-NS at pH = 7.[332] This image is licensed under a Creative Commons Attribution 4.0 International License (https://creativecommons.org/licenses/by/4.0/).

is crucial for adjusting the band structure and enhancing charge separation in COFs, thus enabling overall water splitting. sp^2c-Py-BT COF had an apparent quantum yield of 2.53% at 420 nm. Interestingly, the authors explored the intrinsic relationship between crystallinity and photocatalytic activity and found a sixfold improvement for the highly crystalline COF compared with the amorphous polymer, and they saw a linear relationship of increasing rates from an amorphous polymer to a low-crystalline COF to a medium-crystalline COF to a highly crystalline COF.

6.4 Carbon dioxide reduction

The increasing consumption of fossil fuels has led to uncontrolled carbon dioxide (CO_2) emissions, resulting in serious environmental issues.[334,335] Solutions proposed to address this dilemma include carbon capture utilization and storage (CCUS),[336] amine absorption,[337] and bioenergy with carbon capture and storage (BECCS).[338] Additionally, the photochemical conversion of CO_2 into valuable chemicals like methanol, ethane, formic acid, ethanol, and others presents sustainable and renewable solutions for recycling CO_2 while addressing global issues.[339] Known for their exceptional capacity to adsorb and trap CO_2,[340] COFs are regarded as a promising platform for catalysing the reduction of CO_2 using photocatalysis.[25] Most reported COF-based photocatalysts rely on metalation or transition metals as additive cocatalysts to enhance activity.[25] Ni-,[341] Co-[341–344] or Re-coordinated[345,346] COFs have gained great attention, particularly in CO_2 photoreduction due to their high electron affinity. The mechanism of photocatalytic CO_2 reduction using COFs has also been explicated.[25]

Wang *et al.* have recently reported two Co-coordinated COFs, Co-2,3-DHTA-COF and Co-TP-COF, for photocatalytic CO_2 reduction.[347] TP-COF and 2,3-DHTA-COF were synthesized using 2,4,6-tris(4-aminophenyl)-1,3,5-triazine (TAPT) with 1,3,5-trimethylbenzene (TP) and 2,3-dihydroxybenzene-1,4-dicarboxaldehyde (2,3-DHTA), respectively, in acid-catalysed solvothermal conditions. The COFs were then treated with Co$(NO_3)_2$ in water and ethanol, affording Co-TP-COF and Co-2,3-DHTA-COF. Co-TP-COF created Co–O_3N sites within its frameworks, whereas Co-2,3-DHTA-COF developed Co–O_4 sites. This difference in Co-coordination between the two COFs was due to adjustments to the position of the hydroxyl group in the aldehyde monomer used. The formation of Co–O_4 was identified using spectral characterizations such as X-ray absorption fine structure (FT-EXAFS) spectrum and XPS. The photocatalytic CO_2 reduction to CO was conducted by mixing the photocatalyst with acetonitrile (MeCN)/water solution under simulated visible light irradiation ($\lambda \geq 420$ nm), using [Ru$(bpy)_3$]Cl_2 as the photosensitizer, and TEOA as the electron donor. Under optimized conditions, Co-2,3-DHTA-COF demonstrated a CO production rate of 18 000 μmol g^{-1} h^{-1} and a selectivity of 95.7% (800 μmol g^{-1} h^{-1} H_2), whereas Co-TP-COF showed a lower CO production rate of 11 600 μmol g^{-1} h^{-1} and selectivity of 76.6%. The higher performance with Co-2,3-DHTA-COF was attributed to the Co–O_4 sites. Based on *in situ* and *ex situ* spectral analyses and DFT calculations, the Co–O_4 sites in the COF framework greatly enhanced the charge separation, preventing the recombination of photogenerated electron–hole pairs during the photocatalytic process. The highest apparent quantum yield for Co-2,3-DHTA-COF was 0.47% at 450 nm. Notably, the COF showed a decrease in crystallinity and rate after three cycles.

In 2020, Cooper and co-workers demonstrated the photocatalytic reduction of CO_2 into fuels by tethering the rhenium complex Re(bpy)$(CO)_3Cl$ onto COF materials to create a heterogeneous photocatalyst.[348] They synthesized the 2D sp^2c-COF through the Knoevenagel condensation of 1,3,6,8-tetrakis(4-formylphenyl)pyrene (TFPPy) and 5,5′-bis(cyanomethyl)-2,2′-bipyridine. To produce the metal-coordinated Re-Bpy-sp^2c-COF, they ligated the bipyridine sites in Bpy-sp^2c-COF with Re$(CO)_5Cl$. To demonstrate the strong CO_2 affinity of Re-Bpy-sp^2c-COF, they measured CO_2 uptake, finding that the metalated COF adsorbed 1.7 mmol g^{-1} CO_2 at 273 K and 1.1 mmol g^{-1} at 298 K. Photocatalytic CO_2 reduction experiments were conducted in a quartz flask at 1 atm CO_2 with MeCN as the solvent and TEOA as the proton source and sacrificial electron donor under visible light irradiation ($\lambda > 420$ nm) using a 300 W Xe light source. Re-Bpy-sp^2c-COF produced CO at a rate of 1040 μmol g^{-1} h^{-1} with 81% selectivity *versus* H_2 resulting in a turnover number (TON) of 18.7 for CO over 17.5 hours. Re-Bpy-sp^2c-COF outmatched the homogeneous catalyst Re(bpy)$(CO)_3Cl$ under the same conditions, as the latter deactivated after 3 hours with a TON of 10.3. This superior performance is likely due to the strong visible light absorption and high CO_2 binding affinity of Re-Bpy-sp^2c-COF. The apparent quantum yield was measured at 420 nm, giving 0.5%. When using different wavelengths of light, blue light performed the best (about 400 μmol g^{-1} h^{-1}) followed by green light (about 100 μmol g^{-1} h^{-1}), and then orange light (about 50 μmol g^{-1} h^{-1}). They also compared an amorphous polymer version which demonstrated a lower TON of 2.3 after 12 hours compared with 12.9 for the COF. Notably, after 50 hours of irradiation the COF lost crystallinity.

The photocatalytic reduction of CO_2 using metal-free COFs has also gained a lot of attention.[349–352] For example, in 2021, Liu and co-workers reported metal-free 2D COFs, TpBb-COF and COF-TpPA-1, and graphitic carbon nitride (g-C_3N_4) for visible-light-driven photocatalytic reduction of CO_2.[353] An acid-catalysed Schiff-base reaction was used to synthesize TpBb-COF by the condensation of 2,6-diaminobenzo[1,2-*d*:4,5-d^1] bisthiazole (Bb-NH_2) and 1,3,5-triformylphloroglucinol (Tp-CHO). With minor adjustments, COF-TpPA-1 and g-C_3N_4 were synthesized as described in the literature.[354,355] Photocatalytic reduction of CO_2 was conducted in a glass-sealed reactor under visible light irradiation within a gas–solid system, utilizing the COFs and g-C_3N_4 as the photocatalysts. It should also be noted that no cocatalysts, photosensitizers, or sacrificial reagents were used for these measurements. Both COFs and g-C_3N_4 observed CO as the main product. TpBb-COF demonstrated an optimal average CO production rate of 52.8 μmol g^{-1} h^{-1} at 80 °C with a CO selectivity of 99.0%. This rate was more than double that observed for COF-TpPa-1, 18.3 μmol g^{-1} h^{-1},

and g-C_3N_4, 23.2 μmol g^{-1} h^{-1}. TpBb-COF gave a CO production rate of 89.9 μmol g^{-1} h^{-1} when the CO_2 concentration was changed from pure to 30.0% at 80 °C. The apparent quantum efficiency of TpBb-COF was 0.031% at 420 nm in 30% CO_2 and 0.019% in pure CO_2. This suggests that lower concentrations of CO_2 facilitated the photocatalytic reduction of CO_2. The performance, supported by DFT calculations, can be attributed to the more favourable adsorption of H_2O on TpBb-COF, which enhanced the adsorption and reduction of CO_2. The reaction mechanism was investigated using the rate equation for CO_2 photocatalytic reduction. The rate equation derived correlates the CO_2 concentration with the CO production rate, aligning with the experimental results and theoretical calculations.

In 2023, Jin and co-workers designed hydrophilic, fully conjugated COF materials that utilized H_2O as the hydrogen and electron source for photocatalytic conversion of CO_2 (Fig. 19).[356] This research converted imine-linkages into 4-carboxyl-quinoline linkages in the COFs producing crystalline, porous, polymeric photocatalysts for CO_2 photoreduction. The imine-linked LZU1-COF was synthesized through the Schiff-base reaction by condensing 1,3,5-triformylbenzene and 1,4-diaminobenzene. The quinoline-linked QL-COF was prepared with the one-pot Doebner reaction by reacting 1,3,5-triformylbenzene, 1,4-diaminobenzene, and pyruvic acid. The photocatalytic experiments were conducted using 2 mg of catalyst dispersed in ethanol which was packed onto a glass sheet and placed into a photoreactor containing aqueous solution. This setup was backfilled with pure CO_2 for about 1 h at 1 atm pressure using a 300 W Xe lamp for light illumination. The performances of LZU1-COF and QL-COF were evaluated for CO_2 photoreduction, and both COFs produced CO as the main product along with minor CH_4 production. Compared with LZU1-COF, QL-COF exhibited superior photocatalytic performance, producing CO at a rate of 156 μmol g^{-1} h^{-1}. LZU1-COF produced 25 μmol g^{-1} h^{-1} CO, 6 times less than QL-COF. This high performance is consistent with QL-COF's great H_2O and CO_2 capture capacities and higher carrier transfer efficiency. The inclusion of 4-carboxyl-quinoline in QL-COF improved its light absorption properties and the separation and transfer of photogenerated charge carriers, leading to its excellent performance in CO_2 reduction.

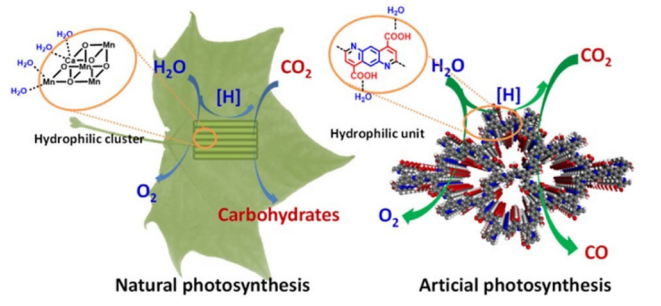

Fig. 19 Natural photosynthesis, and artificial photosynthesis using the hydrophilic 4-carboxyl-quinoline COF (QL-COF).[356] Reproduced with permission from ref. 356. Copyright 2023, Royal Society of Chemistry.[279] Reproduced with permission from ref. 279. Copyright 2020, American Chemical Society.

In 2022, Zhang and colleagues synthesized 3D COFs using an 8-connected porphyrin-based building block arranged in a cubic configuration.[357] These frameworks could be interwoven into an exceptional interpenetrated pcb topology. These distinctive 3D COFs were employed for the photocatalytic reduction of CO_2, resulting in the formation of CO and CH_4. To synthesize the 3D COFs, NUST-5 or NUST-6, 5,10,15,20-tetrayl(tetrakis(([1,1′:3′,1″-terphenyl]-4,4″-dicarbaldehyde)))-porphyrin (TTEP) was reacted with *p*-phenylenediamine (PDA) or dimethyl-*p*-phenylenediamine (PDA-Me) using a Schiff-base reaction under solvothermal conditions, respectively. CO_2 photoreduction experiments were performed with the respective COFs dispersed in a mixture of MeCN, triethanolamine, and H_2O, in a ratio of 3 : 1 : 1 under 1 atm CO_2. The mixture was purged with CO_2 for 30 min while stirring and then illuminated with a 225 W Xe lamp (420 nm cut-off filter). After 10 h, CO production was 54.7 μmol g^{-1} for NUST-5 and 76.2 μmol g^{-1} for NUST-6. Moreover, NUST-5 and NUST-6 displayed low CH_4 production rates of 17.2 μmol g^{-1} and 12.8 μmol g^{-1}, respectively.

6.5 Hydrogen peroxide production

Hydrogen peroxide has become essential in many commercial products such as antiseptics, disinfectants, and as a bleaching agent. Moreover, it is commonly used in synthetic chemistry as a relatively safe oxidant, producing only water and oxygen as by-products. However, at the industrial scale, synthesis of hydrogen peroxide is done through the hydrogenation of anthraquinone using a Pd catalyst followed by oxidation using molecular oxygen.[358] Therefore, new methods to create hydrogen peroxide in less energy-intensive ways have been investigated.[359–362] In recent years, COFs have been expansively used for photocatalytic H_2O_2 production, including the elucidation of the mechanism.[363] Herein, we report on recent cases using COFs to photocatalytically synthesize hydrogen peroxide.

Van Der Voort and Thomas were the first to use COFs for H_2O_2 production.[364] COFs TAPD-$(Me)_2$ and TAPD-$(OMe)_2$ were constructed from *N*,*N*,*N*′,*N*′-tetrakis(4-aminophenyl)-1,4-phenylenediamine and either 2,5-dimethylbenzene-1,4-dicarboxaldehyde or 2,5-dimethoxybenzene-1,4-dicarboxaldehyde (Fig. 20). The COFs were then applied as photocatalysts for H_2O_2 production under visible light from an oxygen-saturated water/ethanol mixture, where ethanol acted as the electron and proton donor. TAPD-$(Me)_2$ and TAPD-$(OMe)_2$ produced 25.3 and 22.6 μmol of H_2O_2, respectively, over 16 hours. When TAPD-$(Me)_2$ COF was used, and the ethanol was increased, the production increased to 57.2 μmol. In a five-hour window, the production of hydrogen peroxide was 97 ± 10 and 91 ± 10 μmol h^{-1} $g_{cat}{}^{-1}$ for TAPD-$(Me)_2$ and TAPD-$(OMe)_2$, respectively.

Van Der Voort *et al.* also synthesized four pyrene COFs from 1,3,6,8-tetrakis(4-formylphenyl)pyrene (Py-CHO) with either 4,4′,4″,4‴-(pyrene-1,3,6,8-tetrayl)tetraaniline (Py-NH_2), 1,4-dia-

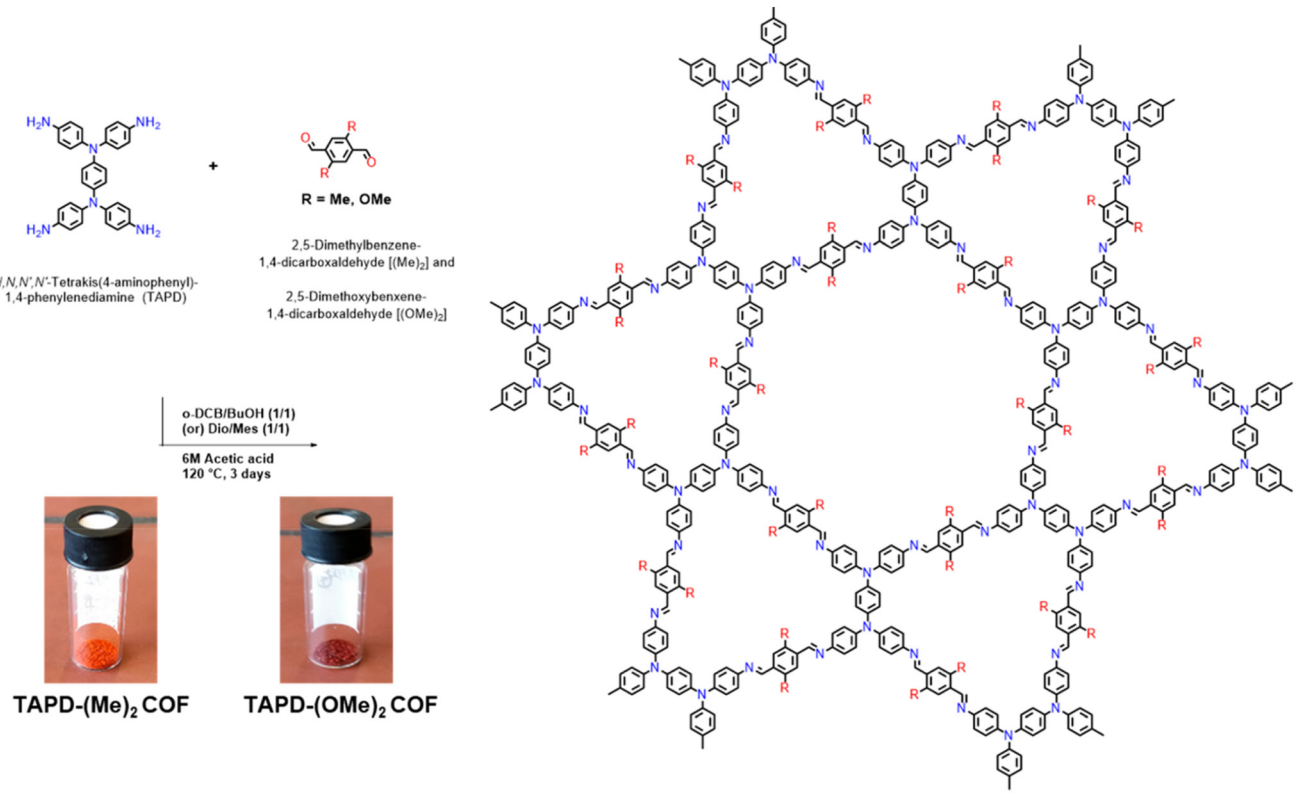

Fig. 20 Synthesis of TAPD-$(Me)_2$ and TAPD-$(OMe)_2$ COFs forming a dual pore kagome lattice.[364] Reproduced with permission from ref. 364. Copyright 2020, American Chemical Society.

minobenzene (Da-NH_2), 2,2′-bipyridine-5,5′-diamine (Bpy-NH_2), or *N*,*N*,*N*′,*N*′-tetrakis(4-aminophenyl)-1,4-phenylenediamine (TAPD) giving Py–Py-COF, Py-Da-COF, Py-Bpy-COF, and Py-TAPD-COF.[365] DFT studies showed that the pyrene unit was the most favoured location for O_2 adsorption comparatively to the N atoms on the bpy or TAPD units. The COFs were tested for hydrogen peroxide production under visible light in O_2 saturated water. Py-Da-COF performed the best at 461 μmol g^{-1} followed by Py-Bpy-COF and Py-TAPD-COF with 241 and 142 μmol g^{-1}, respectively. Interestingly, Py–Py-COF only garnered 47 μmol g^{-1} H_2O_2. When extended to three hours 868, 480, 361, and 85 μmol g^{-1} was produced for Py-Da-COF, Py-Bpy-COF, Py-TAPD-COF, and Py–Py-COF, respectively. When ethanol was added to the mixture, the production of hydrogen peroxide increased for Py-Da-COF and Py-Bpy-COF with a rate of 682 μmol g^{-1} and 452 μmol g^{-1}, respectively. Notably, when benzyl alcohol (BA) was added a two-phase mixture was created that helped to prevent H_2O_2 decomposition and acted as a hole scavenger. The Py-Da-COF rate increased to an astonishing 3670 μmol g^{-1} in a 1 : 1 v/v BA/water mixture. The AQY of Py-Da-COF was measured at 2.4% in water/ethanol and 4.5% in water/BA at 420 nm. Overall, the authors noted that porosity played a key role in the COF activity in addition to O_2 binding sites and reaction conditions.

Wang and co-workers synthesized three benzotrithiophene-based COFs with benzo[1,2-*b*:3,4-*b*′:5,6-*b*″]trithiophene-2,5,8-tricarbaldehyde (Btt) and 4,4,4-triaminotriphenylamine (Tpa), 1,3,5-tris(4-aminophenyl)benzene (Tapb), or 2,4,6-tris(4-aminophenyl)-1,3,5-triazine (Tapt) affording TpaBtt, TapbBtt, and TaptBtt.[366] The COFs were used as photocatalysts for hydrogen peroxide production using a Xe lamp light source in a water solution and under air atmosphere. TaptBtt exhibited the highest production of 31.67 μmol followed by TapbBtt with 12.54 μmol and finally TpaBtt with 5.68 μmol in 90 min. The difference was attributed to the D–A ability of the COFs. When tuning COF loading, 1.5 g L^{-1} gave the best results, increasing hydrogen peroxide production to 1407 μmol g^{-1} h^{-1} using TaptBtt. The authors noted that too much COF material would end up inhibiting light absorption. Furthermore, they synthesized TaptBtt with varying degrees of crystallinity and illustrated that a more crystalline COF gave higher yields. TaptBtt had an AQY of 4.6% at 450 nm. DFT studies revealed the imine linkage was important as a binding site for intermediates. Notably, the COF showed a slight decrease in crystallinity after recycling.

Ni and cohort constructed three β-ketoenamine-linked COFs using 1,3,5-triformylphloroglucinol with melamine, 1,3,5-triphenyltriazine, 4,4′,4″-(1,3,5-triazine-2,4,6-triyl)trianiline, or 4′,4‴,4⁗-(1,3,5-triazine-2,4,6-triyl)tris(([1,1′-biphenyl]-4-amine)) giving COF-N31, COF-N32, and COF-N33.[367] They took these COFs and analysed them for photocatalytic hydrogen peroxide production and how adding phenyl units would

affect the activity. The experiments were conducted in pure water under visible light using a Xe lamp for twelve hours. COF-N32 displayed 7092 μmol g^{-1} (or 605 μmol g^{-1} h^{-1}) followed by COF-N31 with 4316 μmol g^{-1} followed by COF-N33 with 1736 μmol g^{-1}. Notably, COF-N31 exhibited a loss of crystallinity and lowering yields when reused opposed to the other COFs. COF-N32 showed a superior AQY of 6.2% at 459 nm. COF-N32 was also used *ex situ* and *in situ* for disinfection and degradation of diclofenac. Aside from ultrapure water, the photosynthesis of hydrogen peroxide using COF-N32 could also be achieved in tap water, river water, and sea water with rates of 667, 648, and 554 μmol g^{-1} h^{-1} for three hours, respectively. The COFs were also used in membrane filter reactors, garnering about 30 μmol H_2O_2 in two hours for four cycles.

Shen *et al.* synthesized a multi-linker COF, TDB-COF, from 4,4′,4″-(1,3,5-triazine-2,4,6-triyl)tribenzaldehyde (TFPT), 2,5-bis (2-(ethylthio)ethoxy)terephthalohydrazide (BETH), and 2,5-diethoxyterephthalohydrazide (DETH).[368] TDB-COF was used as a photocatalyst for hydrogen peroxide production in water using visible light under air or oxygen atmosphere. In air, 231 μmol g^{-1} h^{-1} was achieved, and under O_2 723.5 μmol g^{-1} h^{-1} was achieved. When adding 10% ethanol as a sacrificial reagent the yield increased to 1000.1 μmol g^{-1} h^{-1}. TDB-COF also performed better in acidic conditions than basic conditions. When TFPT-COF, the analogous COF without any thioether monomer, was used the H_2O_2 production decreased to 79.2 μmol g^{-1} h^{-1}, showing the importance of the thioether moieties. The AQY values of TDB-COF were 1.4% at 365 nm and 1.0% at 400 nm. Notably, TDB-COF lost its crystallinity after recycling.

Wang and co-workers constructed two olefin-linked COFs from benzotrithiophene-2,5,8-tricarbaldehyde (BTT) with 2,4,6-trimethylbenzene-1,3,5-tricarbonitrile (TBTN) or 2,4,6-trimethyl-1,3,5-triazine (TMT) giving TBTN-COF and TMT-COF, respectively.[369] These COFs were then used for the photosynthesis of hydrogen peroxide in water using visible light by a xenon lamp under an oxygen atmosphere. In the first 10 minutes, TBTN-COF exhibited 11 013 μmol g^{-1} h^{-1} H_2O_2 comparatively to TMT-COF with 6392.3 μmol g^{-1} h^{-1}. The authors attributed this difference to the cyano group playing a key role in the catalysis. The AQY of TBTN-COF was 7.59% at 420 nm. Interestingly, when *p*-benzoquinone was added as a scavenger, only TBTN-COF was affected, indicating that *OOH was a mechanistic intermediate for TBTN-COF but not for TMT-COF, which was also supported by DRIFTS. Also, when air was used instead of pure oxygen, the production rates decreased significantly for the COFs. DFT calculations and DRIFTS supported an O_2 Yeager-type binding over Pauling-type binding in TBTN-COF.

Lan *et al.* synthesized two 3D COFs, TAA-CTP-COF and TAB-CTP-COF, with hexa-(4-formyl-phenoxy)-cyclotriphosphazene (CTP) and 2,4,6-tris(4-aminophenyl)-1,3,5-triazine (TAA) or 1,3,5-tris(4-aminophenyl)benzene (TAB) (Fig. 21).[370] The COFs were then studied for their photocatalytic performance in hydrogen peroxide production in water using a Xe lamp

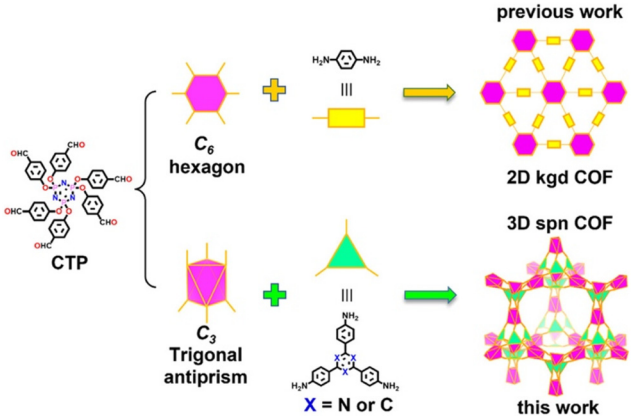

Fig. 21 Schematic representation of COFs with different topological structures synthesized by CTP.[370] Reproduced with permission from ref. 370. Copyright 2024, American Chemical Society.[279] Reproduced with permission from ref. 279. Copyright 2020, American Chemical Society.

under an oxygen-saturated atmosphere. TAA-CTP-COF was able to furnish 1041 μM h^{-1} while TAB-CTP-COF furnished 818 μM h^{-1}. TAA-CTP-COF was explained to perform better as the triazine unit helped increase electron–hole separation. When isopropanol was added as a sacrificial reagent 2221 μM h^{-1} was achieved with TAA-CTP-COF. When pH tests were performed, increasing the acidity or alkalinity decreased the performance.

The Dong group constructed COF-Tfp-BDDA and COF-Tfp-BP by triacetaldehydemesitylphenol (Tfp) and 4,4′-(buta-1,3-diyne-1,4-diyl)diphenylamine (BDDA) or 4,4′-biphenylenediamine (BP).[371] The two COFs were employed as photocatalysts in hydrogen peroxide production using visible light irradiation in pure water under an oxygen atmosphere. COF-Tfp-BDDA showed a hydrogen peroxide yield of 880 μmol g^{-1} h^{-1} while COF-Tfp-BP only furnished 100 μmol g^{-1} h^{-1}. This demonstrated the importance of the diacetylene units. DRIFTS studies revealed an increase in the alkynyl band indicating oxygen binding, and the mechanism proceeded through an oxygen reduction reaction *versus* a water oxidation reaction. Notably, COF-Tfp-BDDA lost almost all crystallinity after 100 h of cycling.

Chen and cohort synthesized DVA-COF and PDA-COF from 1,3,5-tris(4-aminophenyl)benzene (TAPB) with either 2,5-divinylterephthalaldehyde (DVA) or terephthaldehyde (PDA).[372] The COFs were used for the photosynthesis of H_2O_2 using LEDs in a water/benzyl alcohol two-phase mixture. DVA-COF produced 84.5 μmol of hydrogen peroxide after 1 hour, while PDA-COF produced only 8.6 μmol, indicating the importance of the vinyl moieties. The authors proposed that the vinyl groups increased O_2 absorption from Yeager-type absorption. The vinyl groups also enhanced charge separation and transfer efficiency. Notably, benzaldehyde was produced in near equal amounts from the benzyl alcohol additive. The AQY of DVA-COF was 2.84% at 420 nm.

Yu *et al.* constructed six COFs using 1,3,5-triformylphloroglucinol (Tp) with *ortho* or *para* diamines with core benzene (Bda), pyridine (Pda) and pyrazine (Pzda) units, named *o*- or *p*-COF-TpBda, -TpPda and -TpPzda.[373] These COFs were tested for their activity in the photocatalytic production of H_2O_2 under visible light in O_2-saturated water. The production rate for *o*-COF-TpBda was 1030 μmol g^{-1} h^{-1} in one hour, *o*-COF-TpPda was 1947 μmol g^{-1} h^{-1}, and *o*-COF-TpPzda was an astonishing 4396 μmol g^{-1} h^{-1}. This demonstrated that adding pyridinic nitrogen atoms in the linker greatly enhanced the photoactivity. *o*-COF-TpPzda was also used in natural sunlight and air-saturated water and still achieved 1733 μmol g^{-1} h^{-1}. The *p*-COFs were then tested, with rates of 282, 794 and 6434 μmol g^{-1} h^{-1} for *p*-COF-TpBda, *p*-COF-TpPda and *p*-COF-TpPzpa, respectively. Only *p*-COF-TpPzpa performed better than its *o*-COF counterpart; however, it showed severe structural damage by PXRD. DFT and DRIFTS showed that the pyridinic N atoms were important for binding H atoms to help induce the $2e^-$ oxygen reduction reaction (ORR) while the β-ketoenamine linkages were important for the $4e^-$ water oxidation reaction (WOR) process.

Zhu and co-workers synthesized COFs with aliphatic linkers, TAH-COF and BAH-COF, using tartaric acid dihydrazide (TAH) or butanedioic acid dihydrazide (BAH) and 1,3,5-triformylphloroglucinol.[374] These COFs were then applied as photocatalysts for hydrogen peroxide production and hydrogen evolution under visible light using a Xe lamp. For hydrogen peroxide production in pure water, BAH-COF exhibited an impressive 1297 μmol h^{-1} g^{-1} and TAH-COF showed an outstanding 6003 μmol h^{-1} g^{-1}. TAH-COF has the largest reported hydrogen peroxide production rate even with the absence of any cocatalyst, sacrificial reagent, or biphasic solvent mixture. The authors attributed the high rates to the hydroxyl groups allowing for hydrogen bonding. The AQY values of TAH-COF were measured at 7.12% at 475 nm, 7.72% at 500 nm, 7.39% at 520 nm, 3.94% at 550 nm, and 2.22% at 600 nm. TAH-COF was also used for HER, garnering 31.4 mmol h^{-1} g^{-1} with 3 wt% Pt cocatalyst and ascorbic acid as a sacrificial reagent. The authors attributed the success of these systems to the aliphatic linker leading to increased hydrophilicity, high crystallinity, and polarization of the knot which lowers the band gap. This work demonstrates the utility of using aliphatic linkers *versus* the more common rigid π-backbone monomers.

6.6 Aryl boronic acid oxidation

Phenolic compounds are useful for the synthesis of many organic compounds and intermediates in pharmaceuticals.[375,376] Thus their synthesis has become prevalent in research. One route to synthesize these phenolic compounds has been through the oxidation of boronic acids, and performing this through benign means such as photocatalysis has been investigated.[377–381] Herein, we report the use of COFs as photocatalysts for the oxidative conversion of boronic acids to phenols.

Wang *et al.* constructed highly stable benzoxazole-linked COFs, LZU-190, LZU-191, and LZU-192, using 2,5-diamino-1,4-benzenediol dihydrochloride with 1,3,5-triformylbenzene, 2,4,6-tris(4-formylphenyl)-1,3,5-triazine, and 1,3,6,8-tetrakis(4-formylphenyl)pyrene, respectively.[59] These COFs were then used as photocatalysts for the oxidation of boronic acids. The reaction was optimized on 4-carboxyphenylboronic acid where all three COFs showed 99% yield using white LEDs in air over 48 hours. LZU-190 was then applied to a substrate scope of 10 other aryl boronic acids, affording yields of 55–99%. The reaction was also successful in the presence of large substrates such as pyrenyl, naphthyl, and quinolinyl boronic acids with longer reaction times. The authors stated that the photocatalytic activity was derived from the benzoxazole units.

Zhang and co-workers synthesized three olefin-linked COFs using tricyanomesitylene with 4,4″-diformyl-*p*-terphenyl (DFPTP), 4,4′-diformyl-1,1′-biphenyl (DFBP), or 1,3,5-tris-(4-formylphenyl)benzene (TFPB) to give COF-*p*-3Ph, COF-*p*-2Ph, and COF-*m*-3Ph, respectively.[382] These COFs were then applied for the photocatalytic oxidative hydroxylation of boronic acids. The reaction conditions were optimized on 2-naphthylboronic acid, where COF-*p*-3Ph performed the best with 99% yield using a Xe lamp and oxygen with triethylamine as a sacrificial electron donor. The conditions were then used on 8 other boronic acids, garnering yields of 56–99%. The activity was attributed to excellent π-delocalization and great light absorption.

Jiang and co-workers synthesized porphyrin COFs from 2,5-dihydroxyterephthalaldehyde (Dha) and 5,10,15,20-tetrakis(4-aminophenyl)-21*H*,23*H*-porphine to give COFs DhaTph-M (M = Zn or Ni).[383] These COFs were used as photocatalysts in a multitude of oxidation reactions. First, they were tested for the oxidation of α-terpinene using a xenon lamp as the light source under an oxygen atmosphere. The Zn-metalated COF achieved the highest yield and selectivity of ascaridole in 93%, and 7% yield of *p*-cymene, whereas the Ni-metalated version gave 83% yield of ascaridole and 17% *p*-cymene. The difference in yields was attributed to the different mechanistic pathways and reactive oxygen species that were generated. Notably, when using air, instead of pure oxygen, conversion decreased and selectivity towards *p*-cymene increased. DhaTph-M COFs were then applied to the photocatalytic oxidation of phenylboronic acid to phenol using a Xe lamp under an oxygen atmosphere with triethylamine as an electron donor. DhaTph-Ni displayed 99% yield, but DhaTph-Zn only yielded 35%. The authors stated that DhaTph-Ni had higher charge separation leading to higher photocatalytic activity. The authors then used the COFs for the oxidation of thioanisole to form the methyl phenyl sulfoxide product using a Xe lamp under an oxygen atmosphere. DhaTph-Zn afforded 82% yield while DhaTph-Ni afforded only 20% yield. Again, this discrepancy was attributed to varying catalytic pathways. Overall, the authors conducted experiments illustrating that Zn metalation increases triplet oxygen formation and Ni metalation induces exciton dissociation to charge carriers.

Mondal *et al.* constructed two benzothiazole COFs from imine-linked COFs; the imine-linked COFs were synthesized from tris(4-formylphenyl)amine (TPA) and benzene-1,3,5-tri-

carbaldehyde (BCA) with 4,4′,4″-(1,3,5-triazine-2,4,6-triyl)trianiline (Tt), and then using elemental sulfur to form the benzothiazole linkage, making BTZ-BCA-COF and BTZ-TPA-COF.[384] These COFs were then used for the photocatalytic oxidation of phenylboronic acid using oxygen and blue LEDs with triethylamine as a sacrificial reagent. While both COFs exhibited quantitative yields, BTZ-TPA-COF performed the reaction in two-thirds of the time of BTZ-BCA-COF due to its D–A system and smaller band gap. BTZ-TPA-COF was used on five other substrates, furnishing yields of 90–99%. The catalytic performance was due to superior π-delocalization and optoelectronic properties derived from the benzothiazole linkage.

Wen and co-workers prepared COF-JLU25 from 1,3,6,8-tetrakis(4-aminophenyl)pyrene (PyTA) and 4-[4-(4-formylmethyl)-2,5-dimethoxyphenyl]benzaldehyde (TpDA).[385] They took this COF and used it as a photocatalyst for oxidative hydroxylation of aryl boronic acids. The optimized parameters of using white LEDs, air as oxidant, and *N*,*N*-diisopropylethylamine as a sacrificial electron donor were able to achieve a quantitative yield of the 4-(methoxycarbonyl)phenylboronic acid substrate. COF-JLU25 was also used as a photocatalyst using these conditions on 12 other compounds, attaining yields between 25 and 99%. Notably, aryl boronic acids with slightly electron-withdrawing or any kind of electron-donating group gave poor yields, but increasing the reaction times from 12 to 72 hours produced yields ranging from 90 to 99%. The catalytic activity was attributed to connecting boron atoms to electron-poor π-electron systems to increase the tendency of the boron atom to accept an electron. Notably, the COF had a significant decrease in crystallinity after 7 cycles.

The Huo group made a D–A COF, BTT-BTDDA-COF from benzotrithiophene (BTT) and 4,4′-(2,1,3-benzothiadiazole-4,7-diyl)dianiline (BTDDA).[386] Using this COF as a photocatalyst, they were able to convert phenylboronic acid to phenol using blue LEDs, air as the oxidant, and triethylamine as the electron donor in 93% yield. When applying these conditions to a substrate scope of 10 other compounds, high yields of 82–96% were obtained. The photoelectric performance was created by the wide light absorption and narrow band gap energy from efficient intramolecular charge transfer as well as good charge separation. The authors proposed a single-electron transfer mechanism and superoxide radical as the reactive oxygen species (Fig. 22).

Recently, Thomas *et al.* constructed CzDA-TAPT-COF from 4,4-(9-butyl-9*H*-carbazole-2,7-diyl)dibenzaldehyde and tris(4-aminophenyl)benzene.[387] CzDA-TAPT-COF was then employed as a photocatalyst for the oxidative hydroxylation of boronic acids. Using 4-formylphenylboronic acid as a benchmark compound, 92% yield was garnered using blue LEDs, air as the oxidant, and tetramethylethylenediamine (TMEDA) as the sacrificial reagent. Applying this on a broad substrate scope, all substrates gave yields between 53 and 94% with the exception of a triphenylamine-based boronic acid that gave low yield. The high activity was attributed to efficient charge transfer and separation.

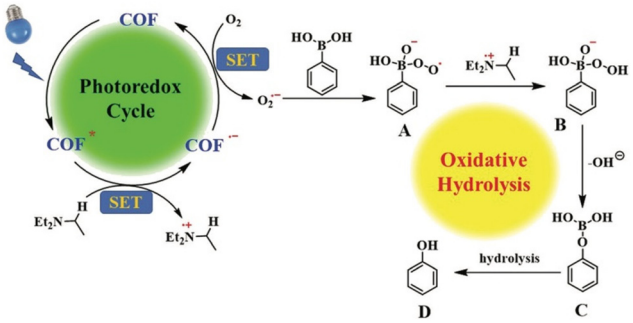

Fig. 22 Possible reaction mechanism.[386] Reproduced with permission from ref. 386. Copyright 2022, Royal Society of Chemistry.[279] Reproduced with permission from ref. 279. Copyright 2020, American Chemical Society.

Recently, Abbaspourrad and co-workers synthesized unique tetrazine-based vinylene-linked COFs from 3,6-dimethyl-tetrazine (DMTAZ) with 1,3,5-tris(4-formylphenyl)benzene (TFPB) and 1,3,5-tris(4-formylbiphenyl)benzene giving TA-COF-1 and TA-COF-2, respectively.[388] These COFs were employed as photocatalysts for the oxidation of arylboronic acids to phenols using blue LEDs, air as the oxidant, and *N*,*N*-diisopropylethylamine as a sacrificial electron donor. Excellent yields of 92–99% were obtained using a wide substrate scope in only three hours. The superior activity was attributed to the tetrazine moiety being the active center, as it can accept an electron to form a radical anion to make a very reactive superoxide radical facilely. The COFs were also shown to be highly active for photocatalytic oxidative coupling of benzylamines, furnishing yields of 90–99% of five different benzylamines substrates. The COFs also were utilized for sunlight-driven photolysis of 5-nitro-1,2,4-triazol-3-one (NTO). Tetrazine is able to be in a stable protonated state, thus also allowing for protonation of TA-COFs (Fig. 23). In fact, TA-COF-1-H^+ and TA-COF-2-H^+ completely degraded NTO within 20 and 25 min, respectively.

6.7 Sulfide oxidation

Sulfoxides have become prevalent in many drug molecules and pesticides.[389–392] Furthermore, the conversion of sulfides to sulfoxides has become a viable method to detoxify harmful sulfur-based warfare agents.[393–395] However, selective oxidation of organic sulfides to sulfoxides can be problematic due to sulfur being easily overoxidized to the sulfone, which has drastically different properties. Conventional methods rely on metals, harsh oxidants and/or thermal conditions, so more environmentally friendly methods such as photocatalysis have been explored to perform this oxidation more easily and selectively.[396–398] Here, we report on using COFs as efficient photocatalysts for sulfide oxidation.

Bai *et al.* synthesized AQ-COF from 2,6-diaminoanthraquinone and 1,3,5-triformylphloroglucinol.[399] They also made AQ-COF_{DMF} which had the same framework but different morphology and structure due to entrapped DMF molecules. These COFs were used as a photocatalyst for the oxidation of

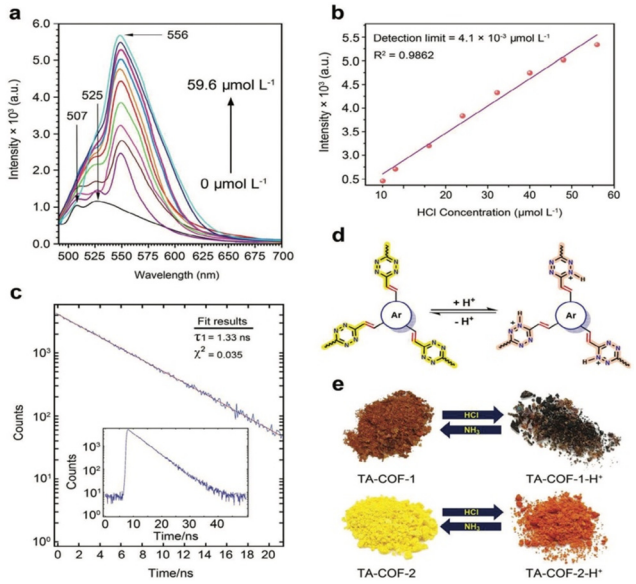

Fig. 23 (a) Fluorescence spectrum of acid-treated TA-COF-1 suspension (0.1 mg mL^{-1}) in 1,4-dioxane under excitation at 465 nm (acid concentration: 0–59.6 mmol L^{-1}). (b) Correlation curve of fluorescence intensity *versus* acid concentration. (c) PL decay spectra of TA-COF-1 monitored upon excitation at 365 nm. (d) Possible protonation and deprotonation sites on TA-COF. (e) Naked-eye photographs of TA-COF powders upon exposure of HCl and NH_3 vapors.[388] Reproduced with permission from ref. 388. Copyright 2024, John Wiley and Sons.[279] Reproduced with permission from ref. 279. Copyright 2020, American Chemical Society.

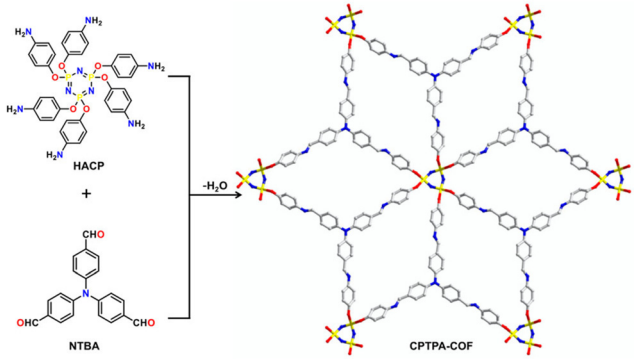

Fig. 24 Schematic diagram for the synthesis of CPTPA-COF.[401] Reproduced with permission from ref. 401. Copyright 2022, American Chemical Society.[279] Reproduced with permission from ref. 279. Copyright 2020, American Chemical Society.

sulfides using oxygen as the oxidant and a Xe lamp as the light source. In the presence of thioanisole, the AQ-COF demonstrated 99% conversion with 97% selectivity for the sulfoxide while AQ-COF$_{DMF}$ only gave 73% conversion with 99% selectivity. The AQY of AQ-COF was 4.34% and 2.70% for AQ-COF$_{DMF}$ at 420 nm. This work demonstrated that the morphology and structure of a COF is important in photocatalytic applications due to a difference in the optical and electronic character. Using AQ-COF, 99% conversion was achieved with selectivity of 94–99% on a variety of aryl sulfides. However, 4-nitrothioanisole and diphenyl sulfide achieved lower yields of 77% and 37%, respectively.

Jin and co-workers constructed crystalline CTFs using *p*-phthalaldehyde and 4-(hydroxymethyl)-benzaldehyde affording CTF-HUST-D1 and CTF-HUST-E1, respectively.[400] The CTFs were then used for photocatalytic oxidation of sulfides using blue LEDs using oxygen in the air as the oxidant. CTF-HUST-D2 achieved conversions of 91–99% and selectivity of 81–96% for the sulfoxide on a variety of sulfide substrates. Notably, ethylphenylsulfide and thiane gave less than 90% selectivity of 81% and 85%, respectively. The authors noted that putting the electron-donating methoxy groups on the CTF backbone enhanced its photoelectron properties.

Zhao and cohort synthesized a unique CPTPA-COF from 4,4′,4″-nitrilotrisbenzaldehyde (NTBA) and hexakis(4-aminophenyl)-cyclotriphosphazene (HACP) (Fig. 24).[401] The CPTPA-COF was then applied as a photocatalyst for the oxidation of sulfides using air as the oxidant and using LED lights. This system was able to quantitatively convert ten various sulfides in four hours with near perfect selectivity for the sulfoxide including 2-chloroethyl ethyl sulfide, a nerve agent simulant. However, 4-bromothioanisole, 2-(methylthio) naphthalene, and ethylphenylsulfide had poor selectivity of around 70%. EPR measurements showed that the COF was an effective photocatalyst for producing $O_2^{\bullet-}$.

Dong and co-workers synthesized a rare chiral COF, (*R*)-DTP-COF-QA, from 2,5-dimethoxyterephthaldehyde (DMTP), 5,10,15,20-tetrakis(4-aminophenyl)porphyrin (TAPP), and *N*,*N*-diethyl-*N*-(4-ethynylbenzyl)ethanaminium bromide (PA-QA) using a Cu catalyst with a chiral ligand.[402] Using LEDs and air as the oxidant, the chiral COF was used as a photocatalyst for the oxidation of thioanisole. Using white LEDs gave appreciable yield of 52% and green LEDs gave a higher 87% yield. When red LED light was used, a high yield of 94% was produced with 99% (*R*) enantiomeric excess (ee). Furthermore, when the (*S*)-DTP-COF-QA was used, a similar yield of 98% and 94% (*S*) ee was afforded. Both chiral COFs were then used to synthesize the drug molecule (*R*/*S*)-modafinil, respectively. A yield of 90% with 88% ee was achieved for (*R*)-modafinil, while (*S*)-modafinil obtained an 88% yield with 86% ee. This work demonstrated a rare example of using red light to efficiently promote a photocatalytic reaction, and the utilization of a chiral COF to directly synthesize a drug molecule in high yield and enantiomeric excess.

Wang and co-workers constructed a nanoparticle-based COF using 1,3,5-tris(4-aminophenyl)benzene (TAPB) and [2,2′-bipyridine]-5,5′-dicarbaldehyde (Bp) and $Co(NO_3)_2$.[403] The $Co(NO_3)_2$/COF was then used to photocatalytically convert thioanisole to the sulfone product under an air atmosphere with a Xe lamp as the light source. Compared with the pristine COF, the nanoparticle-based COF showed 99% yield and 100% selectivity for methyl phenyl sulfone in six hours. The authors attributed this activity to good separation of photogenerated excitons and low charge recombination. This

work illustrated a rare example of making the sulfone *versus* sulfoxide product.

Lang and cohort synthesized a thiazole-linked COF, TTT-COF, from PSM of the imine-linked TTI-COF from 1,3,5-tris(4-aminophenyl)-triazine (TA) and 2,4,6-tris(4-formylphenyl)-1,3,5-triazine (TF).[404] They took these COFs and employed them for the photocatalytic oxidation of aryl sulfides using blue LEDs and oxygen as the oxidant. The imine-linked TTI-COF showed yields lower than 20% while the thiazole-linked TTT-COF afforded yields ranging from 50 to 85% in only 25 min. They also tested the change in photocatalytic activity with varying LEDs. Purple and blue LEDs afforded high yields, green LEDs only afforded 20%, and yellow or red LEDs afforded trace yields. Applying TTT-COF on a larger substrate scope, 17 different sulfides were converted above 90% with near perfect selectivity of the sulfoxide, with the exception of di-^{n}butyl sulfide, in 8–135 min. The authors attributed the photocatalytic performance to the highly photoactive thiazole linkage of the TTT-COF. Notably, the imine-linked TTI-COF lost crystallinity when recycled.

Lang and co-workers designed three olefin-linked COFs from 2,4,6-trimethyl-1,3,5-triazine (TMT) with 1,3,5-triformylbenzene (TFB), 1,3,5-tris(4-formylphenyl)benzene (TFPB), and 1,3,5-tris(4-formylphenylethynyl)benzene (TFPEB) giving TMT-TFB-COF, TMT-TFPB-COF, and TMT-TFPEB-COF, respectively (Fig. 25).[405] These COFs were then used for photocatalytic oxidation of sulfides using blue LEDs under an oxygen atmosphere. TMT-TFPEB-COF possessed much stronger opto-electronic properties compared with the other COFs due to the presence of the alkynyl units. On an initial small substrate scope the TMT-TFPEB-COF performed well, achieving 90% and greater conversion rates, while TMT-TFPB-COF gave much smaller 15–55% conversions, while the TMT-TFB-COF afforded conversions below 10%. The authors also tested the use of green LEDs but only furnished about 15% yield, and yellow or red LEDs resulted in no yield. TMT-TFPEB-COF was employed on ten substrates affording high (>70%) conversion and near perfect selectivity of the sulfoxide products in 30 min. However, 4-nitrothioanisole and diphenylsulfide only gave 13 and 14% conversion, respectively. Overall, the authors illustrated that expanding the π-conjugation with alkynyl units increased the photocatalytic activity of the material. Interestingly, when probing the importance of crystallinity, a highly crystalline TMT-TFPEB-COF performed better than a low crystalline TMT-TFPEB-COF and much better than an amorphous TMT-TFPEB polymer.

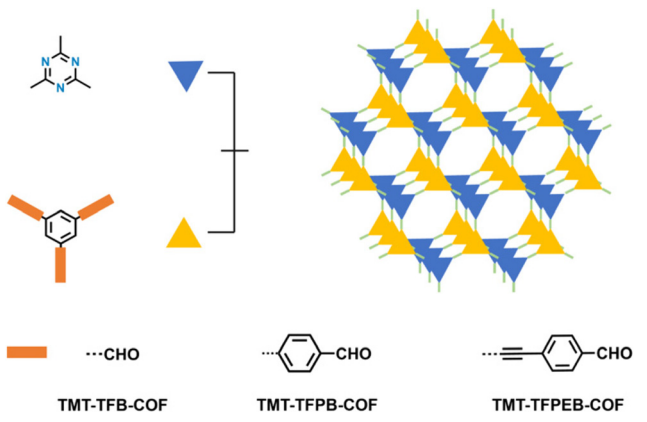

Fig. 25 Schematic illustration of the construction of TMT-TFB-COF, TMT-TFPB-COF, and TMT-TFPEB-COF.[405] Reproduced with permission from ref. 405. Copyright 2024, American Chemical Society.[279] Reproduced with permission from ref. 279. Copyright 2020, American Chemical Society.

6.8 Benzyl alcohol oxidation

The oxidation of aromatic compounds is a critical transformation in organic chemistry with significant applications in pharmaceuticals and the chemical industries.[406–409] Photocatalytic oxidation of alcohols has also been explored as a greener method.[410] COFs have been used as photocatalysts in alcohol oxidation reactions; however, there are a limited number of reports. There has also been a report utilizing a MOF–COF hybrid as a photocatalyst for benzyl alcohol oxidation.[411]

In 2021, Lotsch and co-workers incorporated an alloxazine chromophore unit into a COF framework for metal-free photocatalytic oxidation reactions.[412] FEAx-COF, the first COF featuring an alloxazine unit, was synthesized by condensing 1,3-diethyl-6,9-bis-(4-formylphenyl)alloxazine (FEAx) with 2,4,6-tris(4-aminophenyl)-1,3,5-triazine (TAPT) under solvothermal conditions. The alcohol oxidation reaction was carried out by irradiating a reaction mixture containing 4-methoxybenzyl alcohol (MBA) and FEAx-COF in oxygenated acetonitrile with blue light at a wavelength of 463 nm for 17 hours. Under these reaction conditions, MBA was oxidized to 4-methoxybenzaldehyde (MBAld) with a yield of 70% and a selectivity of 96%. Furthermore, the authors explored the use of other LEDs and observed yields were decreased in green light and there was no yield in orange light. Investigation into the reductive quenching of FEAx-COF, based on the proposed mechanism and quantum chemical calculations of a molecular model representing the COF, demonstrated that MBA was photooxidized by the flavin.

In 2020, Palkovits and colleagues used semi-crystalline thiophene-based covalent triazine frameworks (CTFs) for metal-free photocatalytic oxidation of aromatic alcohols.[413] They synthesized four distinct CTFs, using the solvothermal amidine-aldehyde method, interconnected by a robust Kongming lock.[414] Two of these CTFs contained sulfur. The synthesized CTFs were CTF-Ph (formed from terephthalaldehyde and terephthalamidine), CTF-Th (formed from 2,5-thiophenedicarboxaldehyde and terephthalamidine), CTF-BiPh (formed from 1,4-phthalaldehyde and [1,1′-biphenyl]-4,4′-bis(carboximidamide)), and CTF-PhTh (formed from 2,5-thiophenedicarboxaldehyde and [1,1′-biphenyl]-4,4′-bis(carboximidamide)). The CTFs incorporating thiophene units, enhanced by sulfur, demonstrated a smaller band gap with greater thermal stability in comparison with the phenyl-based CTFs. When the reaction was performed in the conditions of benzyl alcohol, aceto-

nitrile, and CTF photocatalyst under UV light (λ = 365 nm, 0.1 W cm^{-2}) and under O_2 (balloon), all of the CTFs showed benzaldehyde selectivity of 100% after 1 h. CTF-PhTh and CTF-BiPh exhibited high catalytic activity in the photocatalytic oxidation of benzaldehydes, achieving nearly 100% selectivity at or near an 80% conversion rate at a concentration of 1 mg mL^{-1}, 1 h time and a light source of 0.8 W LED UV light (λ = 365 nm). This performance ranks among the most effective metal-free photocatalysts and is comparable to some metal-based counterparts. They also used the CTFs on a small substrate scope of five other aromatic alcohols, showing conversions of 12–100% with selectivity of 42–100%, still showing the need for improved CTF and COF photocatalysts.

In 2020, Huang and co-workers synthesized a series of COF/CdS photocatalysts by varying the cadmium sulfide content ratio and testing these photocatalysts for their photocatalytic activity in the oxidation of aromatic alcohols.[415] This study used terephthalaldehyde and 1,3,5-tris(4-aminophenyl) benzene as precursors with acetic acid as the catalyst to synthesize the COF. COF/CdS composites were obtained by varying the ratio of CdS in the composites. The final products were designated as COF/CdS-1, COF/CdS-2, COF/CdS-3, and COF/CdS-4 with 8.63 wt%, 17.03 wt%, 26.81 wt% and 29.70 wt% CdS, respectively. The reaction was carried out using 20 mg COF catalyst, in trifluorotoluene and acetonitrile using a white light LED lamp of 5.0 W power (λ = 420–780 nm, power density 150 mW cm^{-2}), at 1 atm O_2. The photocatalytic results for selective oxidation of benzyl alcohol to benzaldehyde were formed with no other by-products such as benzoic acid, indicating excellent selectivity. When pure CdS and COF were used separately as photocatalysts, they demonstrated conversion rates of 38.3% and 6.1%, respectively, for benzyl alcohol. For COF/CdS, the conversion of benzyl alcohol rose from 41.3% for COF/CdS-1 to 97.1% for COF/CdS-3, showing high performance for the COF/CdS combination. This demonstrated that depositing an appropriate amount of CdS nanoparticles on a COF can increase their photocatalytic oxidation activity. The authors showed evidence for the use of superoxide radicals to perform this reaction and provided a mechanism (Fig. 26). They also tested COF/CdS-3 on six other aromatic alcohols, achieving conversions of 74–100% with excellent selectivity.

Yang and co-workers recently introduced a COF–COF heterojunction designed to enhance exciton dissociation for visible-light-driven alcohol oxidation.[416] This hybrid structure was composed of two COFs, Tp-TTA COF, synthesized from Tp (1,3,5-triformylphloroglucinol) and TTA (4,4′,4″-(1,3,5-triazine-2,4,6-triyl)trianiline) and QH-COF, created *via* a one-pot Povarov cascade imine formation and cycloaddition reaction. A COF–COF heterojunction was formed by the deposition of nano Tp-TTA colloids onto QH-COF. The reactions were conducted in benzotrifluoride bubbled with oxygen for 20 min before being exposed to light from a Xe lamp equipped with a UV-cut-off filter ($\lambda \geq$ 420 nm). When tested individually, Tp-TTA and QH-COF achieved lower conversions of 29% and 55%, respectively, for the photocatalytic oxidation of benzyl alcohol (BA) to benzaldehyde (BAD) after 6 hours. This could be attributed to their poor charge separation efficiency. Interestingly, the Tp-TTA/QH-10 heterojunction effectively catalysed the oxidation of BA, resulting in a high conversion rate of 92% with a BAD selectivity of 87%. Notably, the Tp-TTA/QH-10 heterojunction showed a decrease in crystallinity when recycled.

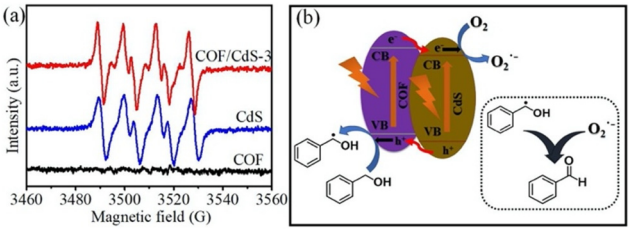

Fig. 26 (a) ESR spectra of benzyl alcohol radicals and $O_2^{\cdot-}$ radical species trapped by DMPO. (b) Proposed catalytic mechanism of the photocatalytic oxidation of benzyl alcohols over COF/CdS-3.[415] Reproduced with permission from ref. 415. Copyright 2021, Elsevier.[279] Reproduced with permission from ref. 279. Copyright 2020, American Chemical Society.

Yang and co-workers also constructed QH-COF@TiO_2 and TiO_2@QH-COF hybrids by doping QH-COF with TiO_2 or growing the COF on TiO_2, respectively.[417] For the photocatalytic oxidation of aromatic alcohols, the reaction was conducted in benzotrifluoride at 1 atm O_2 using a 300 W Xe lamp ($\lambda \geq$ 420 nm). Using benzyl alcohol as a model compound, QH-COF alone achieved 56% conversion and 95% selectivity, and TiO_2 alone showed no conversion. The QH-COF@TiO_2(10%) hybrid showed the best performance at 84% conversion and 93% selectivity for benzaldehyde. This was extended to a substrate scope of aromatic, aliphatic, and cyclic alcohols, garnering conversions of 35–89% and selectivity of 59–95%. However, the QH-COF@TiO_2(10%) hybrid lost crystallinity when recycled.

6.9 Oxidative amine coupling

The utilization of COFs as heterogeneous photocatalysts for oxidative amine coupling has garnered a lot of attention due to their use in synthesizing dyes, pharmaceutical drugs, and agrochemicals.[418,419] This transformation is traditionally done using transition metals or organoboron.[420–422]

In 2022, Tan and colleagues enhanced photogenerated carrier transport and separation efficiency for photocatalytic oxidative amine reactions by utilizing unique donor–acceptor pairs within a COF framework through a push–pull electronic effect.[423] They synthesized the donor–acceptor COF through the polycondensation of electron-donating 1,3,5-triformylphloroglucinol (Tp) and electron-accepting 1,3,5-triazine-2,4,6-triamine (Tt) monomers. The reactions involved the COF photocatalyst in acetonitrile conducted in a cylindrical quartz vessel irradiated with a 35 W halogen lamp (λ > 420 nm) under 1 atm of air. For benzylamine, TpTt-COF displayed complete conversion and excellent selectivity, and in contrast the non-donor–

acceptor TfTa-COF was less efficient, producing only a 33% yield of *N*-benzylidenebenzylamine. The TpTt-COF was also highly effective in the visible-light-driven oxidative coupling of nine other amines with yields ranging from 71 to 99% with great selectivity. DFT calculations confirmed that the internal donor–acceptor pairs in TpTt-COF facilitated high light harvesting and charge separation, leading to superior performance, and the authors proposed a mechanism based on these calculations and UV-Vis data (Fig. 27).

In 2020, Wang and co-workers synthesized fully conjugated D–A COFs for photocatalytic oxidative amine coupling and thioamide cyclization.[424] By incorporating benzothiadiazole units into the frameworks, they achieved high stability and improved charge separation. The Py-BSZ-COF was created through a base-catalysed polycondensation of 1,3,6,8-tetrakis (4-formylphenyl)pyrene and 4,4-(benzothiadiazole-4,7-diyl)diacetonitrile. For the photocatalytic oxidation of amines, the COF photocatalyst was dispersed in acetonitrile at 1 atm air under visible light irradiation with a 15 W 520 nm LED bulb (5 mW cm^{-2}). After 12 hours, *N*-benzyl-1-phenylmethanimine was formed with a 99% conversion rate. The performance of Py-BSZ-COF was compared with sp^2c-COF-3 and COF-JLU22. Under identical reaction conditions, sp^2c-COF-3 achieved a 67% conversion, while COF-JLU22 reached 90%. Py-BSZ-COF was also used on eight other benzylamines, achieving conversions of 52–99% in 98 or 99% selectivity. The superior performance of Py-BSZ-COF was attributed to its production of superoxide radical anions ($O_2^{\bullet-}$).

In 2022, the Wu group developed a series of hydrophilic 2D COFs for photocatalytic oxidative amine reactions in aqueous conditions.[425] The three COFs, TFB-*XX*-DMTH, were synthesized through the polycondensation of 2,5-dimethoxyterephthalohydrazide (DMTH), 1,3,5-triformylbenzene (TFB), and 2-hydroxy-1,3,5-benzenetricarbaldehyde (SOH) under solvothermal conditions. The "*XX*" denotes the different molar ratios of the aldehyde unit (TFB/SOH = 1 : 2, 1 : 1, 2 : 1) used, resulting in TFB-33-DMTH, TFB-50-DMTH, and TFB-66-DMTH, respectively. These COFs were employed for metal-free photocatalytic aerobic oxidative coupling of amines. The reactions were conducted under visible light irradiation from a 30 W blue LED lamp, in air, and at room temperature in water. TFB-33-DMTH, which had the highest number of hydroxyl groups, exhibited the highest conversion rate, selectivity, and excellent recyclability. On nine different benzylamines, conversions were observed at 95–99% with 93–100% selectivity. This performance was attributed to the complementary effect of the extended π-units and the hydroxyl groups, which enhanced the push–pull effect, thereby improving visible-light absorption and the efficiency of charge separation.

Porphyrin-based COFs have been greatly investigated for photocatalytic oxidative amine coupling due to their light absorption capabilities and unique electronic properties.[426–430] In 2022, Jiang and co-workers developed a photoresponsive porphyrin-based COF that converts to its photoisomer under UV irradiation for photocatalytic oxidative amine reactions.[431] This COF incorporated light-harvesting porphyrin photosensitizer units and photochromatic diarylethene with photoswitchable properties, enabling the formation of *o*-COF for the generation of singlet oxygen. The imine-linked photoresponsive ring-opened *o*-COF was synthesized by the reaction between dithienylethene–dialdehyde (*o*-BBTP) and 5,10,15,20-tetra(*p*-aminophenyl)-porphyrin (H_2TAPP) in an acid-catalysed solvothermal reaction. c-COF, the ring-closed photoisomer, was obtained by irradiating *o*-COF with UV light. Photocatalytic oxidation of amines was conducted using COF photocatalyst in acetonitrile with irradiation provided by a 25 W blue LED light under an air atmosphere. *o*-COF exhibited excellent photocatalytic performance, achieving 99% conversion to *N*-benzylidenebenzylamine after 60 min of irradiation in both air and O_2 environments. Interestingly, c-COF showed lower

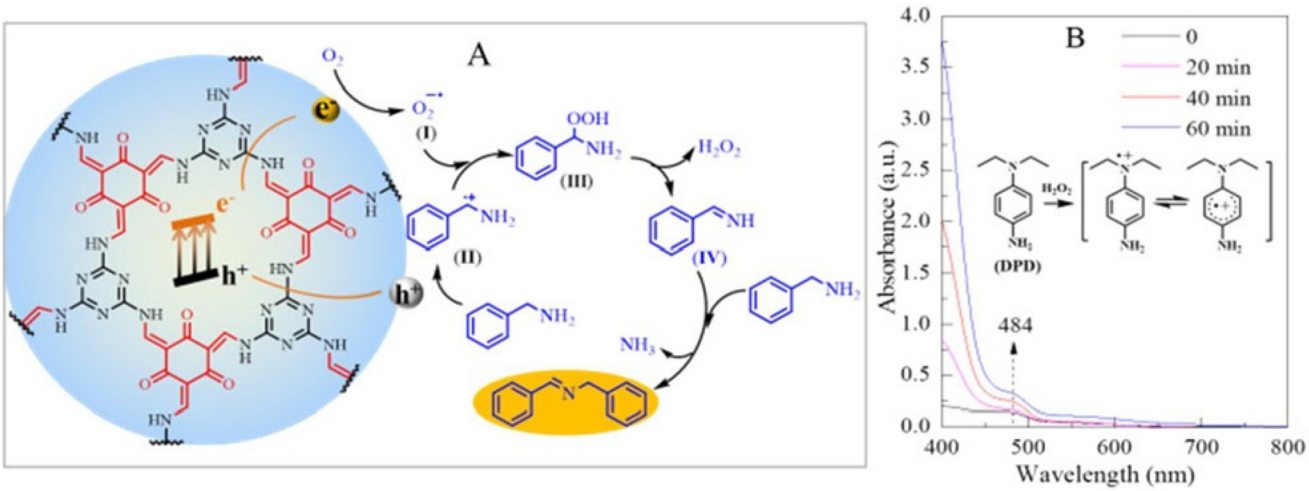

Fig. 27 (A) Proposed mechanism for the visible light-driven oxidative coupling of benzylamine (BA) to *N*-benzylidenebenzylamine with air over TpTt-COF. (B) Changes in the UV-vis spectra of the reaction system upon the addition of DPD.[423] Reproduced with permission from ref. 423. Copyright 2022, Royal Society of Chemistry.

efficiency with only 63% conversion, which was attributed to its reduced capability in generating photoinduced singlet oxygen ($^1O_2$), proving different energy transformations for both COFs. To confirm the involvement of singlet oxygen in the reaction mechanism, triethylenediamine (DABCO), a scavenger for $^1O_2$, was introduced, resulting in a significantly reduced product yield of only 9%. This experiment strongly supports the role played by $^1O_2$ in facilitating the oxidative coupling of benzylamine. *o*-COF was also tested on seven other benzylamines, achieving full conversions in 30–60 min.

β-Ketoenamine COFs have been investigated for their photocatalytic oxidative coupling of amines due to their tunable properties and high stability.[432,433] In 2023, the Lang group synthesized a series of β-ketoenamine COFs, TpPa-COF, TpBD-COF, and TpDT-COF, featuring different linker lengths for photocatalytic oxidative amine coupling.[434] TpPa-COF and TpBD-COF were prepared following slightly modified procedures from the literature.[435] TpDT-COF was synthesized using 1,3,5-triformylphloroglucinol and the diamine, 4,4″-*p*-terphenyldiamine, through a solvothermal condensation reaction. For the photocatalytic oxidation of amine coupling, benzylamine and 5 mg of the photocatalyst were dispersed in acetonitrile in a Pyrex photoreactor, stirred, and irradiated with violet LEDs (3 W × 4). Under the same reaction conditions, TpBD-COF achieved a 78% conversion of benzylamine, while TpPa-COF and TpDT-COF achieved 22% and 61% conversion, respectively. With its moderate linker length, TpBD-COF demonstrated the highest photocatalytic activity for photocatalytic aerobic oxidation of amines, highlighting the significance of linker length in designing more effective COF photocatalysts.

Liu and co-workers constructed diketopyrrolopyrrole-based COFs, TpDPP-Py COF and DPP-Py COF, from 5,5′-(2,5-bis(2-ethylhexyl)-3,6-dioxo-2,3,5,6-tetrahydropyrrolo[3,4-*c*]pyrrole-1,4-diyl)bis(thiophene-2-carbaldehyde) (TpDPP) or (4,4′-(2,5-bis(2-ethylhexyl)-3,6-dioxo-2,3,5,6-tetrahydropyrrolo[3,4-*c*]pyrrole-1,4-diyl)dibenzaldehyde) (DPP) and 1,3,6,8-tetrakis(4-aminophenyl)pyrene (Py).[436] TpDPP-Py COF exhibited a very small band gap of 1.38 eV due to the very strong acceptor and donor units. For the photocatalytic amine coupling, the reaction took place in a sealed Pyrex vessel in acetonitrile that was bubbled with O_2 for 30 min and irradiated by a 300 W Xe lamp with AM 1.5G solar intensity. TpDPP-Py COF exhibited superior catalytic efficacy for the conversion of benzylamine, achieving 100% conversion and 100% selectivity in only 20 min, the best of any reported COF photocatalyst, and most photocatalysts in general. DPP-Py COF took 40 min to achieve the same outcome. TpDPP-Py COF was also used as a photocatalyst on six other aromatic amines, garnering 100% conversion with 100% selectivity in 15–40 min. The authors attribute the success to enhanced absorption capacity and multi-photon absorption effects.

6.10 C–H activation and functionalization

C–H activation and functionalization has become a very important method to target a wide array of compounds from abundant alkane building blocks.[437–439] Directly activating and functionalizing C–H bonds bypasses intermediate functional group installations and conversions, leading to fewer steps in otherwise long synthetic pathways, and increases overall atom economy. However, stoichiometric reagents and directing groups, harsh oxidants, and precious metals are typically required due to the inertness of C–H bonds. In addition, poor selectivity is common due to C–H bonds possessing similar bond dissociation energies and reactivity.[437–439] Performing C–H activation and functionalization photocatalytically has been explored,[440–442] and more recently using heterogeneous photocatalysts.[443] The emergence of COFs as efficient heterogeneous photocatalysts for C–H activation has garnered substantial interest in the scientific community by enabling the selective and sustainable light-driven functionalization of organic molecules.[444–447]

Dong and co-workers synthesized a highly crystalline donor–acceptor (D–A) COF, TPPy-PBT-COF, from 7-(4-formylphenyl)benzo[*c*][1,2,5]thiadiazole-4-carbaldehyde (PBT) and 1,3,6,8-tetrakis(4-aminophenyl)pyrene (TPPy) *via* imine condensation.[448] This COF was used for photocatalytic aerobic cross-dehydrogenative coupling reactions including Mannich and aza-Henry reactions. The reaction was performed in a quartz cell in methanol with L-proline additive under O_2 with LED lights or sunlight. Using *N*-phenyl-1,2,3,4-tetrahydroisoquinoline and acetone as the model reaction, white light, blue light, green light, or sunlight all achieved similar yields between 77 and 84%. Changing either the tetrahydroisoquinoline or the nucleophile, yields of 52–86% were achieved using sunlight. The reaction was also performed on a gram scale using sunlight and still obtained 77% yield. Based on EPR measurements, the authors proposed a mechanism where upon light irradiation TPPy-PBT-COF photogenerates electrons that react with oxygen to form superoxide radicals. The superoxide radicals then abstract a hydrogen from the substrate followed by a second abstraction by the resulting hydroperoxide radical. The imine cation then undergoes nucleophilic addition to form the product with hydrogen peroxide as a by-product.

Yang and co-workers synthesized four imine-linked 2D-COFs and one olefin-linked 2D-COF from previous reports.[444] Specifically, the olefin-linked COF, 2D-COF-2, constructed from 2,4,6-trimethyltriazine and [1,1′-biphenyl]-4,4′-dicarbaldehyde, was used as a photocatalyst for decarboxylative alkylation of heterocycles with *N*-hydroxyphthalimide (NHPI) esters.[449] The reactions were conducted in *N*,*N*-dimethylacetamide, stoichiometric trifluoracetic acid, under blue LED lights and under an argon atmosphere. On the model reaction between isoquinoline with cyclohexyl *N*-hydroxyphthalimide, 2D-COF-2 outperformed its imine counterparts, achieving a yield of 85%, and notably the imine COFs decomposed in the reaction conditions. The reaction was conducted on an impressive 55 substrates obtaining yields from 43 to 97%. They also tested the reaction on the drug molecules lithocholic acid and ibuprofen and achieved yields of 71–78%, and even increased to a 0.5 g scale for lithocholic

acid and still garnered 68% yield. The authors suggested a mechanism where the photoexcited 2D-COF-2 reduces the NHPI ester to give an alkyl radical, with the loss of carbon dioxide, that attacks the TFA-activated quinoline which eventually forms the product after oxidization and deprotonation. Notably, the COF was recyclable but showed decreased crystallinity.

Lin and co-workers constructed an anthraquinone-based 2D COF, DAAQ-COF, from 1,3,5-triformylphloroglucinol (TFP) and 2,6-diaminoanthraquinone (DAAQ).[450] DAAQ-COF was used for photocatalytic C–H functionalization as a direct hydrogen transfer reagent as well as the photocatalyst. The coupling between diethyl azodicarboxylate (DEAD) and tetrahydrofuran (THF) as the model reaction under compact fluorescent light (CFL) irradiation was performed, obtaining 94% yield. The reaction was tested on 15 substrates for C–N coupling with DEAD with yields ranging from 50–98%. The authors proposed the photoexcited COF abstracts hydrogens using the anthraquinone units, which creates a radical that reacts with DEAD to eventually form the product. They also found DAAQ-COF could promote C–H pyridylation using activated pyridines, garnering yields of 53–96% on eight substrates.

Cui and co-workers synthesized COF-1 and COF-2 from 4′,4′′,4′′′,4′′′′-tetraaldehyde (ETBC) and triamine NBC or BADA, respectively, with two-fold interpenetrated ffc networks (Fig. 28).[451] These COFs were used for photocatalytic cross-dehydrogenative coupling (CDC) and the asymmetric α-alkylation of aldehydes. The CDC reactions were conducted under blue LEDs in air at 40 °C in acetonitrile, and α-alkylations were performed under blue LEDs under a nitrogen atmosphere at −10 °C in *N*,*N*′-dimethylformamide with 2,6-lutidine additive and Macmillan chiral co-catalyst. On 8 substituted tetrahydroisoquinoline derivatives, CDC reactions using either COF-1 or COF-2 achieved yields of 50–85%, showing almost identical yields between the two. Interestingly, when comparing the COFs with their amorphous counterparts the COFs performed about 10% better, indicating that crystallinity improved the photocatalytic performance. On 6 aldehydes, α-alkylations using COF-1 or COF 2 obtained yields of 51–88% with 83–94% ee. Interestingly, when white light was used instead of blue light, the reaction suffered, with a yield of 73% with only 36% ee using COF-1. Notably, the COFs lost their crystallinity after these reactions but could be restored by taking the resulting amorphous materials and resubjecting them to the initial synthesis conditions.

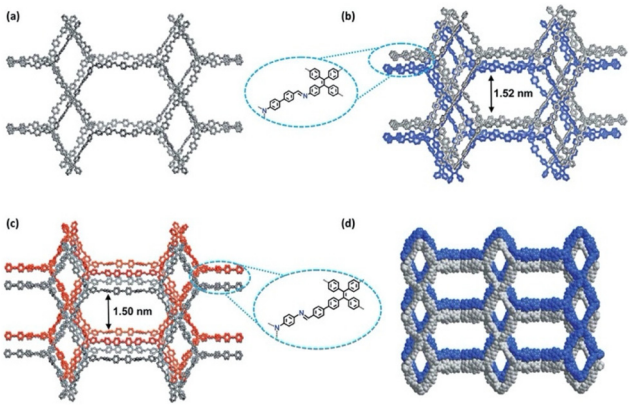

Fig. 28 Structural representations of the COFs. (a) Single ffc network of COF-1; (b) twofold interpenetrated ffc network of COF-1; (c) twofold interpenetrated ffc network of COF-2; (d) space-filling models of the 3D structure of COF-2.[451] Reproduced with permission from ref. 451. Copyright 2020, Royal Society of Chemistry.

In 2023, Xiang and co-workers designed non-substituted quinoline-linked COFs (NQ-COFs).[452] The NQ-COFs were able to be post-synthetically oxidized by *m*-CPBA to yield the quinoline N-oxide form (NQ-COF-O). Specifically, NQ-COF_{E5}-O was used for photocatalytic C–H activation using potassium persulfate as the oxidant, trifluoroacetic acid, and acetonitrile as solvent using blue LEDs under an argon atmosphere. The model reaction of isoquinoline and toluene was first explored, achieving 93% yield using the aforementioned conditions. Low yields were afforded when other oxidants, acids, or solvent mixtures were used, and using a homogeneous analog or the non-oxidized version of the COF provided yields below 15%. This reaction was scaled up to 12 mmol, and with increased reaction time, could still achieve 84% yield. When other substituted quinolines, a benzothiazole, and a benzoxazole were tested, yields ranging from 67 to 93% were obtained. This work demonstrated the utility of embedding hydrogen atom transfer moieties within a COF for photocatalytic C–H activation. The authors proposed a mechanism in which the photogenerated holes oxidize the quinoline N-oxide units of the COF to create *N*-oxy radicals, which abstracts a hydrogen atom from the C–H substrates to afford alkyl radicals that undergo a Minisci-type reaction.

In 2024, Zhang and co-workers constructed four vinylene-linked COFs (V-COFs) based on 2,4,6-trimethyl-1,3,5-triazine (TMTA) with 1,4-diformylbenzene (DFB) (V-COF-1), DFB and anthracene-9,10-dicarbaldehyde (AN) (V-COF-AN), DFB and benzo[*c*][1,2,5]thiadiazole-4,7-dicarbaldehyde (BT) (V-COF-BT), or a combination of DFB, AN, and BT (V-COF-AN-BT).[453] V-COF-1 was used as a control with no oxidation or reduction sites, V-COF-AN was used as a control only bearing oxidation sites, V-COF-BT was used as a control only bearing reductive sites, and V-COF-AN-BT was the main COF containing both oxidative and reductive sites. They then applied these COFs for photocatalytic direct C–H difluoromethylation of heterocycles using $NaSO_2CF_2H$ as the fluorine source, oxygen as the oxidant, and DMSO as the solvent using blue LEDs. Using 1-methylquinoxolin as the model substrate, V-COF-AN-BT performed the best, yielding 91% product, with the other V-COFs yielding 55% or less, showing the importance of the dual-active-center approach. Based on experiments, the authors proposed that upon light irradiation, the photogenerated electrons react with oxygen to form superoxide radicals and photogenerated holes react with $NaSO_2CF_2H$ to produce the CF_2H radical. The CF_2H radical reacts with the substrate, undergoes a 1,2-H shift, and then is oxidized by the superoxide radical to form the product with H_2O_2 as a by-product. They performed a

substrate scope using 12 different substituted quinoxalin-2(1*H*)-ones, heterocycles, and five bioactive molecules, for example xanthine derivatives and uracil, obtaining yields of 53–95%. The model reaction was also conducted on a gram scale, achieving 71% yield.

Banerjee and co-workers synthesized three COFs from 1,3,5-triformylphloroglucinol (Tp) and 4,4′-azodianiline (Azo), 2,8-diamino(6-phenylphenanthridine) (Dpp), or 1,3,5-tris(4-aminophenyl)benzene (Tab) giving TpAzo, TpDpp, and TpTab, respectively.[454] These COFs were used as photocatalysts for C–H borylation using trimethylamine-borane in acetic acid under a nitrogen atmosphere with blue LEDs and using ammonium persulfate as a sacrificial electron acceptor. On the model substrate, 4-methylquinoline, TpAzo obtained 90% yield while TpDpp and TpTab only garnered 21 and 33%, respectively. Notably, the COF lost crystallinity upon five recycles and there was a decrease to 77% yield in the fifth run. On 12 substrates, TpAzo achieved yields ranging from 18 to 96%. The authors proposed that upon light irradiation, the photogenerated electron from the COF reacts with persulfate to form a sulfate radical that abstracts a hydrogen from trimethylamine-borane. The resulting boryl radical reacts with the protonated quinoline in a Minisci addition. Finally, this radical cation formation undergoes rearomatization through oxidation by the photogenerated hole of the COF, and deprotonation to afford the product.

6.11 C–N cross-coupling

C–N cross-coupling has shown prominence in the synthesis of natural products and drug molecules.[455–458] Like most cross-coupling reactions, this is typically mediated by precious metals and researchers have investigated using sustainable ways to promote C–N cross-coupling reactions.[459–463] Here, we summarize some reports of COFs enabling photocatalytic C–N cross-coupling reactions.

Maji and Banerjee synthesized TpBpy COF from 1,3,5-triformylphloroglucinol (Tp) and 5,5′-diamino-2,2′-bipyridine (Bpy).[464] This COF was dual metalated using [Ir$(ppy)_2(CH_3CN)_2]PF_6$ and then $NiCl_2$. The Ir complex acted as a photosensitizer while the Ni acted as the catalytic center. The Ni–Ir@TpBpy COF was used as a photocatalyst for visible-light-mediated C–N bond formation in the presence of 1,1,3,3-tetramethylguanidine (TMG) base in acetonitrile at 40 °C using blue LEDs under an N_2 atmosphere. The Ni–Ir@TpBpy COF was successfully applied as a photocatalyst for C–N coupling on over 60 substrates with yields ranging from 42 to 95%, and this was also used on over 10 drug precursors and bio-active molecules garnering 46–81% yields. The authors attributed the high activity to the short distances between the Ir and Ni centers and the lack of multinuclear deactivation. Furthermore, an amorphous version of the COF showed only 31% yield of the standard reaction, showing the importance of crystallinity.

Thomas *et al.* used 2,6-diaminoacridine (Acr) and 1,3,5-triformylbenzene-based monomers to construct different β-ketoenamine/imine COFs with 0, 1, and 2 imine bonds ratios giving Tp-Acr, DHTA-Acr and HTA-Acr COFs, respectively.[465] These COFs were used for photocatalytic C–N coupling of 4-bromobenzotrifluoride and pyrrolidine with $NiBr_2$ additive in DMA using blue LEDs where Tp-Acr showed the highest activity, 91% yield, due to the larger amount of β-ketoenamine linkages and thus metal binding sites. When using green LEDs instead, only 38% yield was obtained even when tripling the reaction time. They also showed a substrate scope of five other aryl bromides and achieved yields from 66 to 94%. The authors attributed the high catalytic activity of the COF to the broad range light absorption and to high charge carrier separation. Notably, the COF lost crystallinity over recycling, and addition of nickel catalyst was needed in each cycle.

Yang and cohort manufactured an imine COF from 5,5′,5″-(benzene-1,3,5-triyl)tripicolinaldehyde with *p*-phenylenediamine followed by a Povarov reaction to yield a quinoline-linked COF, Q-COF, and metalated it with $NiCl_2$ and either [Ir$(ppy)_2(MeCN)_2]OTf$ or [Ir$(coum)_2(MeCN)_2]OTf$ to give [Ir$(ppy)_2(N^N)$ + $NiCl_2$]@Q-COF or [Ir$(coum)_2(N^N)$ + $NiCl_2$]@Q-COF.[466] The [Ir$(coum)_2(N^N)$ + $NiCl_2$]@Q-COF was employed as a photocatalyst for both C–S and C–N coupling using blue LEDs in acetonitrile with TMG or pyridine as the base, achieving 92 and 90% yields, respectively, while the [Ir$(ppy)_2(N^N)$ + $NiCl_2$]@Q-COF only gave 47 and 44% yield, respectively, showing the importance of the Ir photosensitization ability. They also performed the reaction on 35 C–S substrates and 10 C–N substrates, affording yields of 65–99%. The authors proposed a mechanism going through Ni(I) and Ni(III) based on calculations and CV data (Fig. 29).

Hou and co-workers synthesized an imine-linked COF using 4,4′,4″-(1,3,5-triazine-2,4,6-triyl)trianiline (TTA) and 2,6-diformylpyridine (DFP) and then metalated with $NiCl_2$ giving Ni SAS/TD-COF.[467] This Ni SAS/TD-COF was applied as a photocatalyst for a C–N coupling reaction using 4-bromobenzotrifluoride and pyrrolidine using DABCO as the base in DMA and using blue LEDs, giving 99% yield. The optimized conditions were applied on a large substrate scope of over 30 compounds and afforded yields of 71–99%.

Zhang and co-workers constructed three bipyridine, pyrene-based cyano-vinylene COFs from TFPPY, TFPPY-F, and TFPPY-OCH_3 with BPY-CN and metalated with $NiCl_2$ to make sp^2c-COF_{dpy}-Ni, sp^2c-F-COF_{dpy}-Ni, sp^2c-OCH_3-COF_{dpy}-Ni, respectively.[468] They applied these COFs for both C–N and C–O coupling photocatalytically using blue LEDs. They achieved optimal yields of 99% for both reactions when using the fluorinated version, with drastically reduced yields using the unsubstituted or methoxy versions, illustrating the importance of monomer substitution. The authors attributed this discrepancy to fluorine enhancing the migration of photogenerated electrons. The authors also displayed a substrate scope of C–O coupling on 15 other compounds, obtaining yields of 60–99% and a substrate scope for C–N coupling of 13 other compounds with yields varying between 80 and 99%.

Thomas and co-workers synthesized 8 COFs using a mix of 2,6-acridinediamine (Acr) and 2,2′-bipyridine-5,5′-diamine (Bpy) with benzene-1,3,5-tricarbaldehydes with 0–3 alcohols

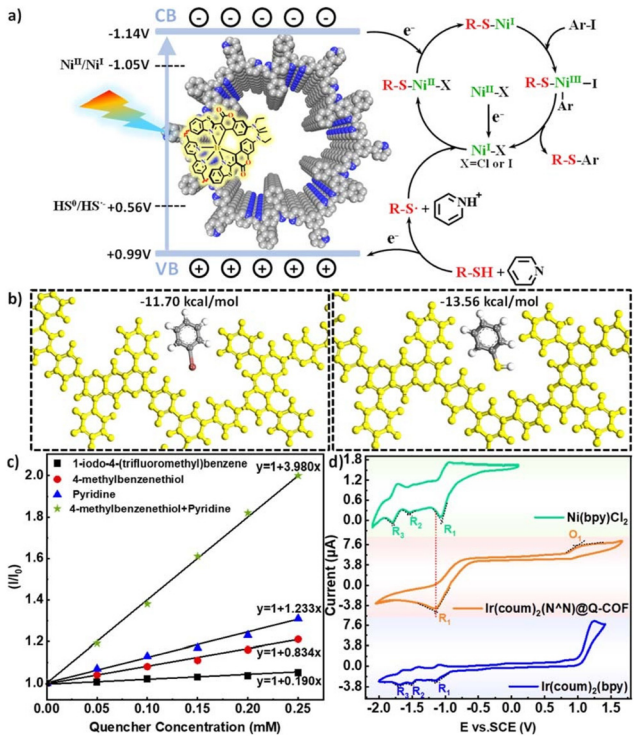

Fig. 29 (a) Proposed mechanism of [Ir(coum)$_2$(N^N) + NiCl$_2$]@Q-COF catalyzed C–S cross-coupling. (b) The binding energies between different substrates (iodobenzene left and thiophenol right) and COF. (c) Comparative Stern–Volmer quenching experiment in C–S cross-coupling. (d) CVs of model complexes.[466] Reproduced with permission from ref. 466. Copyright 2024, Royal Society of Chemistry.[279] Reproduced with permission from ref. 279. Copyright 2020, American Chemical Society.

substituents which were then metallated with NiCl$_2$.[469] Acr^2-Tf-Bpy^1 COF was used as a photocatalyst for the C–S coupling of 4-iodobenzotrifluoride with methyl 3-mercaptopropanoate using blue LEDs and *N*,*N*-*tert*-butylisopropylamine as a base in acetonitrile, achieving a quantitative yield. Using green light gave 74% yield, and a much longer reaction time of 48 hours using red light gave quantitative yield. When the other COFs were applied the authors saw that decreasing the number of hydroxy groups, and thus keto tautomerization, caused an increase in product with yields from 4 to 86%. The COFs were also tested on the coupling of 4-iodobenzotrifluoride and sodium *p*-toluenesulfinate in DMA getting yields of 25–55%. These were then tested on the C–N coupling between pyrrolidine and 4-bromobenzotrifluoride in DMA in which the opposite trend was observed, where increasing the number of hydroxy groups, and thus keto tautomerization, caused an increase in product with yields from 4 to 80%. The authors described the discrepancy as being caused by a mechanistic difference. In the C–S coupling, the catalytic center is the Ni binding at the bipyridine sites and thus is aided from high charge-carrier mobility from imine-based linkages. In the C–N coupling, the active catalyst is Ni(pyrrolidine)$_n$ which is sensitized by the COF that benefits from the linkage which creates good charge separation of excitons and stabilizes electrons on the acridine moiety. Notably, the COF lost crystallinity under these photocatalytic conditions.

6.12 C–O cross-coupling

C–O bonds are highly prevalent in natural products and many drug molecules, making their formation key to obtaining high-value chemicals.[470–472] Furthermore, C–O bonds have been investigated as coupling partners due to their abundance in nature and lesser toxicities. However, C–O bonds have high dissociation energies which require high temperature and catalyst loading, so methods to perform these coupling reactions under more ambient conditions, such as photocatalysis, have been examined.[461,462,473] Here, we present research that has been reported on using COFs as photocatalysts for C–O cross-coupling reactions.

Wang and co-workers synthesized LZU-713@Ni (Fig. 30) using a metalated phenanthroline monomer, Phen-CHO@Ni, and 1,3,6,8-tetrakis(4-aminophenyl)pyrene (PyTTA).[474] They used this COF for photocatalytic C–O cross-coupling of 4-bromobenzonitrile and methanol, obtaining a high yield of 97% using blue light in DMA and triethylamine as the base. They applied the reaction conditions to 20 substrates and achieved yields ranging from 69 to 98%, but the reaction did not work when substituting methanol for water or phenol. The authors also used this COF for C–S cross-coupling of aryl halides and aryl thiols which afforded yields of 80–99% on 20 substrates and using 2,6-lutidine as the base instead. Even more, the COF was applied to C–P cross-coupling of aryl iodides and phosphine oxides which garnered yields of 56–99% on 18 substrates, and using caesium carbonate as the base and methanol as the solvent instead. The authors attributed the catalytic activity to easily accessible catalytic sites in the COF and fast transfer of photogenerated electrons. Notably, the COF had a decrease in crystallinity post-reaction and a total loss of crystallinity after four runs.

Chen and co-workers synthesized sp^2-COF$_{dpy}$ from 1,3,6,8-tetrakis(4-formylphenyl)pyrene (TFPPy) and 2,2′-([2,2′-bipyridine]-5,5′-diyl)diacetonitrile (BPYDAN) which was then metalated using NiCl$_2$ to give sp^2-COF$_{dpy}$-Ni.[475] They used this COF

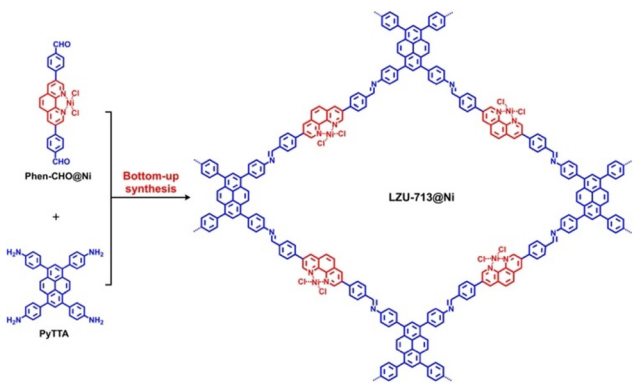

Fig. 30 Bottom-up synthesis of LZU-713@Ni.[474] Reproduced with permission from ref. 474. Copyright 2023, John Wiley and Sons.

for C–O photocatalytic cross-coupling of 4-bromobenzonitrile and methanol using blue LEDs and triethylamine as the base, achieving a yield of 99%. Interestingly, when using green LEDs (520–525 nm) 91% yield was attained, but no yield was obtained while using red LEDs. When adding in $NiCl_2$ *in situ* with the pristine COF *versus* the metalated version 99% yield was also obtained. The optimized conditions were applied to a 25-compound substrate scope, getting yields of 55–99%. The authors also showed that water could be used instead of methanol, but the reaction had to be heated at 50 °C. Furthermore, they showed the reaction could be scaled up to 10 mmol and get 98% yield. The authors believed that the catalytic activity was due to bimolecular photoinduced electron transfer to create the active COF-Ni^{I} species.

Zhang and cohort synthesized two hydrazone-linked COFs using 1,3,5-tris(4-formylbiphenyl)benzene (TFBPB) or 1,3,5-tri(3-hydroxy-4-formyl-ethynylphenyl)-benzene (THFEB) with 1,3,5-benzene tricarbohydrazide (BTH) to make BPh-COF and AC-COF, respectively.[476] They used these COFs as photocatalysts for C–O cross-coupling of 4-chlorobenzonitrile and methanol using blue LEDs with $NiCl_2$ added *in situ* and NaOH as the base. AC-COF achieved 90% yield while BPh-COF only afforded 45% yield. They attributed this difference to the AC-COF having better light absorption than BPh-COF. When using white LEDs instead, only 20% yield was obtained for AC-COF. They then took AC-COF and used it for the C–O coupling on 15 substrates of aryl chlorides and their bromide counterparts, giving 15–99% yields. The aryl chlorides typically performed around a half to two-thirds as well as the bromide versions. They also showed that ethanol and benzyl alcohol could be used instead of methanol. Notably, this system was shown to be not very recyclable, losing about 45% yield over five cycles when adding in more Ni every time, and all the way down to 10% when not adding fresh Ni in. ICP-OES analysis showed large amounts of Ni leaching. The authors believed this was the result of having to use a strong base, NaOH, to perform this reaction, *versus* the typically used triethylamine, which caused the metal to leach off. Additionally, the COF showed a decrease in crystallinity over the recycling process. The COFs were also used for photocatalytic oxidative coupling of amines where AC-COF showed quantitative yields of 8 benzylamines and BPh-COF showed yields of 32–82%, again due to smaller range light absorption.

Zhang *et al.* constructed bpy-COF from 4′,4′,4′-(1,3,5-triazine-2,4,6-triyl)trianiline (TTA) and 5,5′-dialdehyde-2,2′-bipyridine (BPDA) which was metalated using $NiBr_2$ to give Ni(II)-bpy-COF.[477] This COF was used as a photocatalyst for the hydroxylation of aryl chlorides. The reaction was optimized for C–O coupling of 4-chlorobenzonitrile and H_2O in DMF/MeCN with triethylamine as the base and using blue LEDs at 40 °C, achieving 99% yield. This system was applied successfully to 14 other substrates in yields of 47–98%. Interestingly, when applied to a biphenyl-based substrate the yield fell to 27% and when applied to a terphenyl-based substrate no yield was observed, which the authors stated was likely due to poor substrate diffusion into the pores and steric hindrance. Furthermore, the authors found that the COF allowed for efficient transfer of photogenerated electrons to the Ni centers and the photogenerated holes generated highly reactive hydroxyl radicals from their reaction with water.

6.13 C–C cross-coupling

C–C cross-coupling reactions are used to construct many diverse organic molecules for a wide variety of applications.[458,478–481] This includes the use of the widely known Suzuki, Sonogashira, Heck, Hiyama, Stille, Kumada, and Negishi coupling reactions. While these reactions are typically conducted at high temperatures, researchers have investigated performing these reactions photochemically in the presence of a suitable catalyst.[462,482–485] Here, we report the use of COFs as photocatalysts to perform C–C cross-coupling reactions.

Cai and co-workers were the first to report a COF for cross-coupling photocatalytically.[486] They synthesized TTI-COF from 4,4′,4″-(1,3,5-triazine-2,4,6-triyl)trianiline and 4,4′,4″-(1,3,5-triazine-2,4,6-triyl)tribenzaldehyde, and then used sulfur to post-synthetically convert the imine-linkage to a benzothiazole-linkage, making TTT-COF. The TTT-COF was then treated with Na_2PdCl_2 and $NaBH_4$ to form Pd nanoparticles in the COF, namely Pd NPs@TTT-COF (Fig. 31). This hybrid COF was then used as a photocatalyst for the Suzuki coupling of 4-iodotoluene and phenylboronic acid using K_2CO_3 as the base in ethanol and water using a Xe lamp, affording quantitative yield. This was applied to a small substrate scope, garnering yields ranging from 82 to 99%. Moreover, this system was impressively used for Stille, Heck, and Sonogashira couplings with substrate scopes obtaining yields of 39–99%. The authors attributed the success of the reactions to the benzothiazole linkage, which can bind the nanoparticles and provides high conduction efficiency of the photocarriers.

Islam and co-workers mechanochemically made TpPa-1 from phenylenediamine and 2,4,6-triformylphloroglucinol (TFP), and this COF was used as a photocatalyst alongside Ni(dmg)$_2$ for the carboxylation of aryl halides using CO_2.[487] The

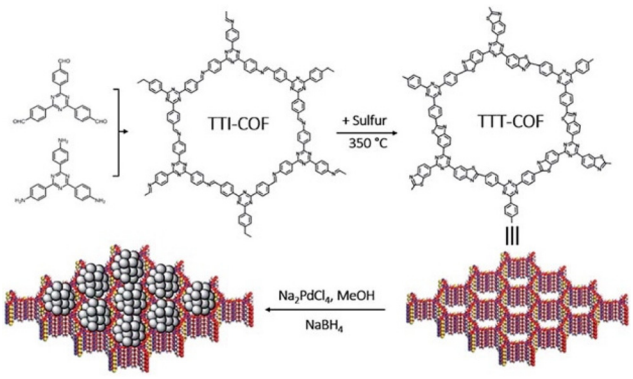

Fig. 31 Graphical representation of the synthesis of Pd NPs@TTT-COF.[486] Reproduced with permission from ref. 486. Copyright 2020, Royal Society of Chemistry.

reaction was optimized on iodobenzene using blue LEDs and triethylamine (TEA) as a sacrificial reagent, achieving a yield of 86%. Interestingly, when *p*-terphenyl was used instead of Ni $(dmg)_2$ a 56% yield was obtained. The optimized conditions were used on 12 substrates including aryl bromides and chlorides, garnering yields of 70–91%. This COF was also used as a photocatalyst for the C–H activation of benzene, nitrobenzene, fluorobenzene, and anisole, obtaining yields of 60–70%.

Mas-Ballesté and co-workers constructed Phen-COF using a phenanthroline monomer and 1,3,5-tris(4-aminophenyl) benzene (TAPB) which was then metalated with $[(dF(CF_3)ppy)_2$-Ir-μ-Cl$]_2$ and $NiCl_2$·glyme to form Ir,Ni@Phen-COF.[488] This COF was employed as a photocatalyst for the cross-coupling of potassium benzyltrifluoroborates and aryl bromides. Optimized conditions were performed using potassium benzyltrifluoroborate and 4-bromotoluene using 2,6-lutidine as the base in acetone/MeOH and blue LEDs, achieving 90% yield. The reaction conditions were applied to 8 other compounds, obtaining yields of 34–99%, with electron-donating substituents markedly giving lower yields. To test the utility of this COF as a photocatalyst, the authors also showed it was active for the cross-couplings of potassium *tert*-butyltrifluoroborate and 4-bromobenzonitrile, organic silicate and 4-bromobenzonitrile, and Boc-protected proline and 4-bromobenzonitrile, obtaining yields of 76, 92, and 86%, respectively. The authors attributed the catalytic activity to the phenanthroline stabilizing the coordination of the metal centers.

Maji and cohort synthesized Bpy-sp^2c-COF from 1,3,6,8-tetrakis(4-formylphenyl)pyrene (TFPPy) and 2,2′-([2,2′-bipyridine]-5,5′-diyl)diacetonitrile (BPDAN) which was then metalated using $NiCl_2$ to give Ni@Bpy-sp^2c-COF.[489] They applied this COF as a photocatalyst in eight C–X (X = B, C, N, O, P, S) coupling reactions, achieving yields ranging from 61 to 99%. The C–C coupling reaction was performed on allyl acetate and 2-naphthaldehyde using blue LEDs at 40 °C, obtaining a yield of 61%. C–O coupling was investigated using methyl 4-iodobenzoate and Boc-protected proline, obtaining 91% yield at 60 °C using compact fluorescence light. The C–O coupling reaction was performed on about 50 compounds, giving yields of 42–86% including drug functionalization and derivatizing naproxen using multiple aryl iodides. C–S coupling was analysed using iodobenzene and thiophenol using blue LEDs at 40 °C and obtained quantitative yield. This was furthered by testing methyl 4-iodobenzoate with sodium benzenesulfonate and getting the sulfonate product in 94% yield but using purple LEDs instead. The C–S coupling reaction was also performed on about 50 substrates, with yields garnering 31–93% including functionalization of bioactive derivatives. C–N coupling was investigated using methyl 4-iodobenzoate and *p*-toluene-benzenesulfonamide or sodium azide, achieving yields of 91 and 89%, respectively, using blue LEDs at 40 °C. However, using azides required the use of triethanolamine as a sacrificial reagent. C–B coupling was studied using 4-iodobenzonitrile with bis(pinacolato)diboron, getting 96% yield with purple LEDs at 40 °C. C–P coupling was investigated using methyl 4-iodobenzoate and diphenylphosphine oxide, obtaining 73% yield using blue LEDs at 40 °C. Notably this is the only reaction where the homogeneous catalyst performed better, garnering 81% yield. The reactions could also be performed on a gram scale.

6.14 Pollution degradation

Water treatment has become a huge field with the development of more pharmaceuticals, pesticides, textile dyes, and other organic pollutants that have been released into water sources around the world.[490–492] Furthermore, water treatment to kill harmful bacteria and viruses such as Salmonella, Campylobacter, and Norovirus is also important.[493] Common methods to treat water include disinfection with chlorine or chloramines, ultraviolet disinfection, ozonation, Fenton reactions, adsorption, coagulation and flocculation, and membrane filtering.[490–493] One of the most promising methods is photocatalytic degradation due to the potential of using visible light under ambient conditions. Here, we summarize some key reports of COFs used as photocatalysts to eliminate contaminants.

Tong and co-workers synthesized two donor–acceptor COFs with β-ketoenamine linkages using 1,3,4-thiadiazole-3,5-diamine (TD1) or 1,2,4-thiadiazole-2,5-diamine (TD2) with 1,3,5-triformylphloroglucinol (Tp) giving COF-TD1 and COF-TD2, respectively.[494] They used these COFs for photodegradation of paracetamol, diclofenac, bisphenol A, naproxen, and tetracycline hydrochloride using a xenon arc lamp with a UV cut-off filter. COF-TD1 showed 98% degradation of paracetamol in 60 min, and 97% within 120 min for the other contaminants. Interestingly, 97% of paracetamol could also be degraded in 60 min using natural sunlight. This process was scaled up using the COF on ITO glass with simulated sunlight, degrading 92% of paracetamol in 4 hours. The authors attributed this activity to both intermolecular charge transfer and proficient electron–hole separation from the push–pull effect of the D–A system.

Bhaumik and co-workers constructed C_6-TRZ-TPA COF from tris(4-formylphenyl)amine (TPA-aldehyde) and 4,4′,4″-(1,3,5-triazine-2,4,6-triyl)trianiline (TRZ-amine).[495] This COF was employed as a photocatalyst to degrade rose bengal (RB) and methylene blue (MB) dyes as well as iodine vapor capture under visible light irradiation. The COF showed 99% degradation of RB in 80 min and even 90% within 30 min of a 250 ppm solution. It also degraded 97% of a 20 ppm MB solution within 120 min. The COF also exhibited high iodine vapor uptake capacity of 4832 mg g^{-1}. The activity of the COF was due to efficient electron–hole charge transfer from the D–A system.

Jiang and co-workers constructed TFPB-TAPT-COF from 1,3,5-tris(*p*-formylphenyl)benzene (TFPB) and 2,4,6-tris(4-aminophenyl)-1,3,5-triazine (TAPT), which was mixed with several emulsifiers including Triton X-100, sodium dodecyl sulfate (SDS), or polyvinyl alcohol type 1788 (PVA).[496] These COF–emulsifier matrixes were used in the photodegradation of 10 ppm solutions of methylene blue (MB) and sodium fluorescein (SF) under simulated natural light conditions. The pris-

tine COF only degraded 26% of MB in 50 min while COF-Triton X-100 degraded 98% in the same amount of time. Furthermore, 72% of SF dye could be degraded in 90 min using the COF and 82% using COF-Triton X-100. The authors credited the emulsifier with increasing the surface area of the COF, and thus creating more oxygen vacancies on the particle surface and therefore more active sites.

Wang and co-workers synthesized HDU-26 from benzo[1,2-*b*:3,4-*b*′:5,6-*b*″]trithiophene-2,5,8-tricarbaldehyde (BTT) and 4,4′-(benzo[*c*][1,2,5]thiadiazole-4,7-diyl)dianiline (BT).[497] HDU-26 was used as a photocatalyst for the reduction of Cr(VI). This was done by exposing the COF and a 10 ppm $K_2Cr_2O_7$ solution to simulated visible light using a Xe lamp. The COF demonstrated 99% reduction after 60 min of irradiation. They also studied the effects of initial pH, catalyst dosage, and Cr(VI) concentration. HDU-26 showcased removal rates of rhodamine B (RhB), methylene blue (MB) and methyl orange (MO) of 82.6, 56.4, and 99.1%, respectively. Notably, when the COF was employed in a one-batch system, including the dyes and Cr(VI), the dye removal rates were increased to 97.2, 62.3, and 99.2%, respectively. The authors attributed this to the COF generating electron–hole pairs for the oxidation of organics with a synergistic effect of Cr(VI) reduction.

Van Der Voort and cohort made three olefin-linked COFs, TMT-TT-COF, TMT-N-COF, and TMT-BT-COF, from 2,4,6-trimethyl-1,3,5-triazine (TMT) and bithiophene (TT), naphthalene (N), and benzothiadiazole (BT) monomers.[498] These COFs were used as photocatalysts for bisphenol A (BPA) degradation and H_2O_2 production. TMT-TT-COF and TMT-N-COF illustrated exceptional BPA degradation of 96% and 94.7% of a 25 ppm solution under visible light within 60 min while TMT-BT-COF only showed 40% degradation. When tested for H_2O_2 production TMT-TT-COF, TMT-N-COF, and TMT-BT-COF generated 1952, 1742, and 748 μmol g^{-1} h^{-1}, respectively, using a Xe lamp under an O_2 atmosphere. Under an Ar atmosphere, they displayed much lower rates of 234, 117, and 13 μmol g^{-1} h^{-1}, respectively. The authors attributed these results to TMT-TT-COF and TMT-N-COF being made from D–A building units that promote efficient charge transfer and separation. Moreover, the thiophene moiety in TMT-TT-COF induces a narrower bandgap, better intramolecular charge carrier transport, and less charge recombination.

Li and co-workers made two isomeric D–A COFs from pyrene (Py) and benzo[*c*][1,2,5]thiadiazole (BT) units containing either aldehyde or amino functional groups to form Py-C-BT-COF and Py-N-BT-COF (Fig. 32).[499] They took these COFs and applied them in rhodamine B degradation and H_2 evolution photocatalytically. Using visible light, 95% of rhodamine B was degraded within 60 min by Py-N-BT-COF, while it was only 70% degraded with Py-C-BT-COF. The opposite activity was seen for H_2 evolution. Under visible light with sodium ascorbate as sacrificial reagent and 5 wt% Pt cocatalyst, Py-C-BT-COF revealed an average H_2 evolution rate of 253.1 mmol g^{-1} h^{-1} while Py-N-BT-COF showed little activity. This work showed that changing the isomerism and atomic positioning in a COF can change the band gap and optical properties of the material, which influences the photocatalytic activity.

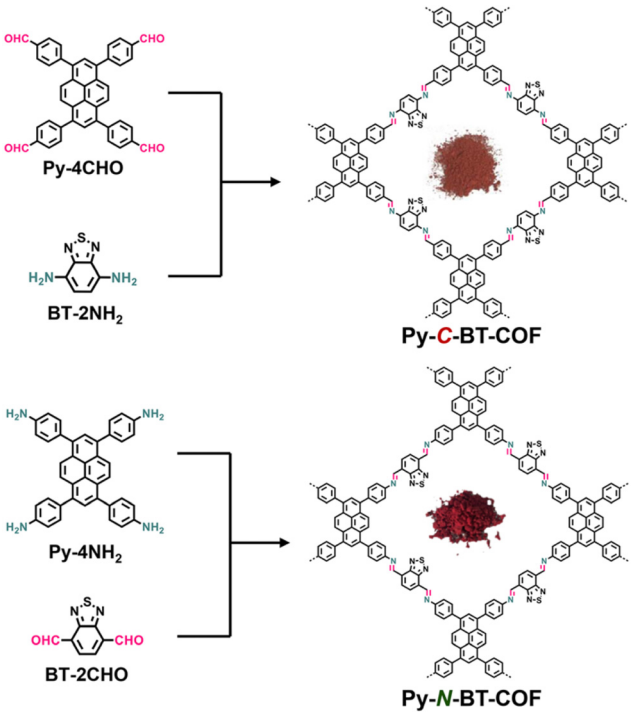

Fig. 32 Schematic representation of the synthesis of the Py-BT-COF isomers.[499] Reproduced with permission from ref. 499. Copyright 2024, Royal Society of Chemistry.

Xi and co-workers constructed three COFs from different combinations of 2,4,6-tris(4-formyl-phenyl)-1,3,5-benzene (TFPB), 2,4,6-tris(4-amino-phenyl)-1,3,5-benzene (TAPB), 2,4,6-tris(4-formyl-phenyl)-1,3,5-triazine (TFPT) and 2,2′-(5′-(4-(cyanomethyl)phenyl)-[1,1′:3′,1″-terphenyl]-4,4″-diyl)diacetonitrile (TCPB) to make TFPB-TCPB COF, TFPT-TCPB COF, and TFPT-TAPB COF.[500] The cyano-olefin linkage of TFPT-TCPB COF was further oxidized to a carboxylic acid to make TFPT-TCPB COF-COOH. These were used as photocatalysts to degrade 200 ppm solutions of rhodamine B (RhB) dye using a Xe lamp. First, they were tested for pure absorption of the dye with no light. TFPT-TCPB COF, TFPB-TCPB COF, and TFPT-TCPB COF-COOH achieved around 35% RhB removal in 90 min; however, TFPT-TAPB COF had about 50% removal in the same time frame, likely due to its much larger surface area according to the authors. In the presence of light 97% of RhB could be removed, but no degradation was shown. When peroxymonosulfate (PMS) was added, the RhB dye could be degraded with light. Using TFPT-TCPB-COF-COOH 62.2% of RhB was mineralized in 50 min due to its activation of PMS.

El-Mahdy and co-workers synthesized 3D, D–A hetero[6]radialene-based COFs from 2,4,6-triformylphloroglucinol and (4,4′,4″,4‴-pyrene-1,3,6,8-tetrayl)tetraaniline (PyTA-$4NH_2$) or 4,4′,4″,4‴-([9,9′-bifluor-enylidene]-3,3′,6,6′-tetrayl)tetraaniline (BFTB-$4NH_2$), giving TFP-Py 3D COF and TFP-BF 3D COF, respectively.[501] They used these COFs for absorption of rhodamine B dye. On an 18 mg L^{-1} sample, complete absorption occurred in 10 minutes for TFP-Py 3D COF and 60 minutes for

TFP-BF 3D COF. They then tested the photodegradation of a 10 mg L^{-1} rhodamine B sample under visible light using the COFs. The TFP-BF 3D COF and TFP-Py 3D COFs achieved complete removal of rhodamine B within 150 minutes and 165 minutes, respectively, with photodegradation efficiencies of 96.60% and 95.90%, respectively. The authors also tested these COFs for photocatalytic hydrogen evolution using a Xe lamp with UV and visible light with or without Pt cocatalyst and ascorbic acid as a sacrificial reagent. TFP-Py and TFP-BF 3D COFs without the inclusion of Pt cocatalyst were 4.96 and 21.04 mmol g^{-1} h^{-1}, respectively. When adding 1 wt% Pt, HER for TFP-BF 3D COF achieved 30.72 mmol g^{-1} h^{-1}. AQYs for TFP-BF 3D COF were 8.70, 10.12, and 15.73% at wavelengths of 420, 450, and 600 nm, and AQYs of 2.54, 4.21, and 0.49% for TFP-Py 3D COF at the same wavelengths, respectively.

6.15 Other applications

Thanks to their tunable photoelectronic properties, COFs have been designed and leveraged to accomplish various transformations. While COFs have been mainly applied as photocatalysts for the reactions previously discussed, they have also been utilized for a plethora of other organic reactions. Herein, recent reports of various non-related photoapplications are detailed that use COFs photocatalytically.

Banerjee *et al.* synthesized a β-ketoenamine-linked COF, TpTt, using melamine, or 1,3,5-triazine-2,4,6-triamine (Tt), and 2,4,6-triformylphloroglucinol (Tp).[502] They took the TpTt COF and used it for *E* to *Z* photoisomerization of olefins. Optimizing conditions, using blue LEDs in DMF, the authors achieved 90% yield of *cis*-stilbene from *trans*-stilbene. They performed this on seven other substrates, garnering yields of 42–71%. The authors also conducted mechanistic studies and DFT calculations and showed the COF absorbs light and is excited, undergoes intersystem crossing to the triplet state, then transfers energy to the substrate (*trans*-stilbene) which transforms into a biradical triplet intermediate state which is converted to the product (*cis*-stilbene).

Gu and co-workers constructed an anionic Ti-based COF, Ti-COF-1, from $Na_2Ti(2,3\text{-DHTA})_3$ (DHTA = 2,3-dihydroxyterephthalaldehyde) and 4,4′,4″,4‴-(pyrene-1,3,6,8-tetrayl)tetraaniline (PyTTA), (Fig. 33).[92] Ti-COF-1 was then used as a photocatalyst for a Meerwein addition reaction using white LEDs. Using different arenediazonium salts and styrenes, yields of 49–75% were achieved with 132–202 turnover number. The authors attribute the success to the anionic skeleton of Ti-COF-1 being an excellent adsorbent for cationic arenediazonium salts which can then easily reduce them by the photogenerated electrons to form reactive aryl radicals.

Zhang and cohort made TPT-COF-Cu from 4,4′,4″-((1,3,5-triazine-2,4,6-triyl)tris(oxy))tribenzaldehyde (TPT-CHO) and [2,2′-bipyridine]-5,5′-diamine (Bpy-NH_2) using a deep eutectic solvent followed by metalation by $CuCl_2$.[503] TPT-COF-Cu was then used as a photocatalyst for phosphorylation of terminal alkynes. Optimized conditions were performed on the model reaction of phenylacetylene and diethyl phosphite. Using blue LEDs, triethylamine base, and 2-MeTHF as solvent 95% yield

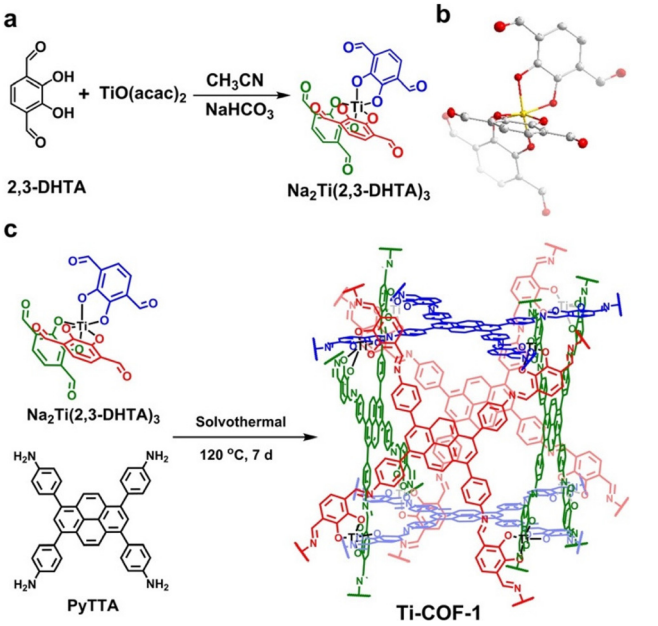

Fig. 33 (a) Synthesis of $Na_2Ti(2,3\text{-DHTA})_3$. (b) X-ray single-crystal structure of $Na_2Ti(2,3\text{-DHTA})_3$. All H atoms, Na^+ and solvent molecules have been omitted for clarity. C – gray, O – red, Ti – yellow. (c) Synthesis of Ti-COF-1.[92] Reproduced with permission from ref. 92. Copyright 2021, John Wiley and Sons.

was obtained. Notably, using white or green light achieved yields of 83 and 90%, respectively. They also used these conditions on an expansive substrate scope, 32 compounds, obtaining yields ranging from 85 to 95%. When increased to a gram scale 92% yield was isolated.

Chen and co-workers mimicked graphitic carbon nitride (g-C_3N_4) by making heptazine COFs from (1,3,3a^1,4,6,7,9-heptaazaphenalene-2,5,8-triyltris(benzene-4,1-diyl))tris(methanetriyl)hexaacetate (HEP-OAc) and 1,3,5-tris(4-aminophenyl)triazine (TAPT-NH_2) or 1,3,5-tris(4-aminophenyl)benzene (TAPB-NH_2), giving HEP-TAPT-COF and HEP-TAPB-COF, respectively.[504] The COFs were then used for photocatalytic oxidations of benzylic C–H bonds and sulfides using O_2 as the oxidant and a xenon lamp as the light source. For the test reaction on isochroman, HEP-TAPT-COF performed better than HEP-TAPB-COF or g-C_3N_4, achieving 100% conversion and 90% selectivity for isochromanone. Notably, smaller yields were obtained when using an amorphous version of the COF or a heptazine-based amorphous polymer, Cy-pip, indicating crystallinity is important for charge separation. Four other isochroman derivatives and three other benzylic hydrocarbons achieved yields of 70–99% of the ketone product. HEP-TAPT-COF was also able to selectively oxidize six sulfides to the corresponding sulfoxides in quantitative yields. The authors believe the heptazine moieties played a crucial role in generating the reactive $^1O_2$ for the oxidations.

Zhao and co-workers synthesized several COFs, COF*X*-Au (*X* = 1–5, based on monomer units), from D_2-symmetric porphyrins (1–4 = proximal H, 5 = proximal pentafluorobenzene) and

benzothiadiazole (1), pyrazine (2), benzene (3), or dimethoxybenzene (4) linkers and metalated with $KAuCl_4$.[505] The COFs were then used for photocatalytic nitrogen fixation using a xenon lamp as the light source and K_2SO_3 as a sacrificial reagent. COF1-Au, the COF with electron-withdrawing benzothiadiazole units, achieved a rate of 333.0 μmol g^{-1} h^{-1}. When using COF4-Au, the COF with electron-donating dimethoxybenzene units, a lower rate of 196.1 μmol g^{-1} h^{-1} was achieved. When COF5-Au, the COF with the pentafluorobenzene-substituted porphyrin, was used the rate increased to 427.9 μmol g^{-1} h^{-1}. N_2H_4 was also tested as a product but only 0.5 μmol g^{-1} h^{-1} was observed. Furthermore, when the reaction was done in basic conditions instead, a small rate of 7.8 μmol g^{-1} h^{-1} was achieved. The authors attributed the success of COF1-Au and COF5-Au to higher charge separation efficiency and lower charge transfer resistance from the electron-withdrawing moieties.

Wang and cohort synthesized a D–A COF, PTZ-TTA-COF (Fig. 34), using *N*-(4-formylphenyl)-phenothiazine-3,7-dicarbaldehyde (PTZ-CHO) and 1,3,5-tris(4-aminophenyl)triazine (TTA-NH_2).[506] They used PTZ-TTA-COF and a control TPA-TTA-COF (TPA = triphenylamine) as photocatalysts for amine homocoupling and cyclization to thioamides using blue LEDs and air as oxidant. On 14 substrates, PTZ-TTA-COF garnered yields of 75–99% for the oxidative amine coupling while the TPA-TTA-COF gave much lower yields of 36–56%. For the cyclization of five different thioamides PTZ-TTA-COF performed well, achieving 60–72% yield, and again TPA-TTA-COF achieving lower yields of 25–37%. The authors illustrated the importance of donor strength for creating efficient D–A systems by reducing the band gap of the photocatalyst.

Li and co-workers constructed an imidazole-linked COF, PyPor-COF, using pyrene-4,5,9,10-tetraone, 5,10,15,20-tetrakis-(4-benzaldehyde)porphyrin, and ammonium acetate.[507] This COF impressively demonstrated light absorption over the entire visible light spectrum and exhibited a super low band gap of 1.75 eV. To test its singlet oxygen generation, PyPor-COF was illuminated with red light in the presence of 9,10-anthracenediyl-bis(methylene)-dimalonic acid (ABDA), which showed a fluorescence quantum yield of 10.3%, and with the addition of rose bengal photosensitiser the quantum yield increased to 77.8%. PyPor-COF was then used as a photocatalyst for the oxidative cleavage of olefins to carbonyls using red light and air as the oxidant. On the model substrate 1,1-diphenylethylene 96% yield of benzophenone was obtained. When using purple, blue, or green LEDs instead, respective yields of 94, 90, and 89% were obtained, showing the great light-absorbing and photocatalytic properties of the COF. This was then tested on nine styrene derivatives, achieving yields of 71–95%. PyPor-COF was also tested for the oxidation of 14 thioanisole derivatives to their corresponding sulfoxides, garnering yields of 73–99%. This work demonstrated a rare example of a COF photocatalyst using red light for organic transformations.

Zhao and co-workers synthesized TFPA-TAPT-COF-Q and TFPA-TPB-COF-Q using tris(4-formylphenyl)amine (TFPA) and 1,3,5-tris-(4-aminophenyl)triazine (TAPT) or 1,3,5-triphenylbenzene (TPB) and converting the imine linkage to a quinoline linkage using phenylacetylene and BF_3.[508] The quinoline-linked versions showed further red light absorption and much lower band gaps by about 0.5 eV. These COFs were then used photocatalytically for the oxidative decarboxylation of arylacetic acids using 1,1,3,3-tetramethylguanidine (TMG) as the cocatalyst and air as the oxidant (Fig. 35). The reaction was optimized using 4-methoxyphenylacetic acid and achieved 100% conversion and 86% selectivity for 4-methoxybenzaldehyde, with 4-methoxybenzyl alcohol as the side product. This was conducted on six other arylacetic acids, garnering conversions of 64–100% with selectivity of 80–92%. The COFs were also

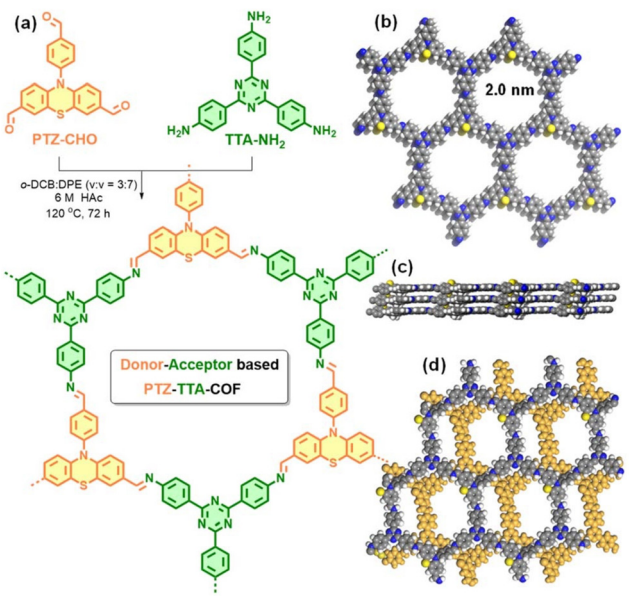

Fig. 34 (a) Synthesis of the donor–acceptor PTZ-TTA-COF. Top (b) and side views (c) of the AA stacking mode as well as the top view (d) of the AB stacking mode for the PTZ-TTA-COF (carbon, gray; nitrogen, blue; sulphur, yellow; hydrogen, white).[506] Reproduced with permission from ref. 506. Copyright 2023, Royal Society of Chemistry.

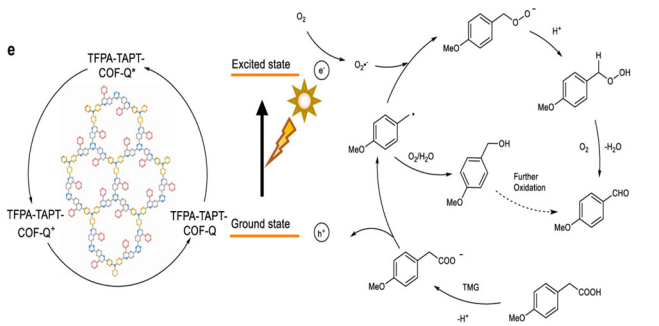

Fig. 35 Proposed mechanism for the decarboxylation of arylacetic acids.[508] This image has been adapted showing only part (e). This image is licensed under a Creative Commons Attribution 4.0 International License (https://creativecommons.org/licenses/by/4.0/).

used for oxidative amine homocoupling, achieving conversions of 65–100% and selectivity of 53–100%. Furthermore, TFPA-TAPT-COF-Q was used to photosynthesize hydrogen peroxide using a Xe lamp as the light source with pure oxygen as the oxidant in a water/benzyl alcohol (10 : 1) solution, obtaining a production of 295 900 μmol g^{-1}. Notably, the imine-linked versions exhibited considerably deceased yields for each of these reactions. This work illustrated the importance of the linkage for enhancing photochemical properties of COFs.

Zeng and cohort constructed bipyridine, ionic bipyridine, and ionic imidazole COFs named PY-BPY-COF, ion-PY-BPY-COF, and im-PY-BPY-COF, respectively, from 4,4′,4″,4″′-(pyrene-1,3,6,8-tetrayl)-tetraaniline (PY) with [2,2′-bipyridine]-5,5′-dicarbaldehyde (BPY).[509] Through PSM of the bipyridine, the ionic bipyridine COF was made through reaction with bromoethane, and the ionic imidazole COF was made through cycloaddition with paraformaldehyde. These COFs were used as photocatalysts for the oxygen reduction reaction (ORR). The im-PY-BPY-COF achieved the highest TOF of 0.0198 s^{-1} at a potential of 0.7 V, which was 5.4 and 3.2 times greater than the values exhibited by PY-BPY-COF (0.0037 s^{-1}) and ion-PY-BPY-COF (0.0061 s^{-1}), respectively. The mass activity for im-PY-BPY-COF was 0.57 A mg^{-1}, which was higher than PY-BPY-COF (0.17 A mg^{-1}) and ion-PY-BPY-COF (0.19 A mg^{-1}). The im-PY-BPY-COF was also the most selective, with only H_2O_2 by-product yields of 10–18% compared with that of PY-BPY-COF of 12–50% and ion-PY-BPY-COF of 20–30%. Using DFT calculations and DRIFTS, the authors showed the important reactive oxygen species was OOH*. This work exhibited a rare example of using a COF photocatalyst for ORR.

7 Conclusions and outlook

Covalent organic frameworks have emerged as a prosperous class of crystalline, porous polymers. The properties of COFs have lent them the ability to be used as effective photocatalysts for a plethora of photoinduced transformations, in addition to other applications. In this review, the design, synthesis, characterization, and photocatalytic application of COFs have been presented. Numerous linkages of COFs were discussed with an emphasis on their effect on stability and structural properties. Furthermore, the dimensionality and morphology of COFs were summarized. The various synthetic methods were also outlined including solvothermal, microwave-assisted, ionothermal, mechanochemical, and more. Instrumentation, techniques and methods to characterize COFs as well as photocatalytic products and intermediates were also broadly explored. Moreover, approaches for enhancing COF photoelectric properties and photocatalytic activity, such as extending light absorption, band gap engineering, doping, composites, and others, were assessed. Finally, the use of COFs as photocatalysts in a myriad of organic reactions was reviewed.

This review has illustrated that COFs are well positioned for photocatalytic applications. Owing to their capacity to integrate countless organic building blocks and diverse covalent bonds they can be tailored to integrate a high degree of functionality. The inherent in-plane conjugation and interlayer π-stacking of COFs enhance their light-absorbing capability. Furthermore, they can host high light-absorbing chromophore units and photosensitizers for superior performance in light-driven processes. COFs also feature high surface areas and porosity, enabling suitable diffusion of reactants and products through the pores and easy access to the active sites. Their rigidity and use of donor–acceptor systems permits for high charge carrier mobility and separation of photogenerated holes and electrons. Furthermore, their heterogeneous nature can reduce or altogether avoid deactivation pathways seen in homogeneous systems such as the formation of inactive nanoparticles or complexes, irreversible oxidation or reduction, excited state side reactions, and collisional and aggregation-based quenching.

However, there are some drawbacks and areas for further improvement in the use of COFs in photocatalytic applications.

(1) Most reports use blue light or white light to perform the catalysis but have not studied what wavelength or range is suitable for the specific catalytic reaction. Studies that have examined the usage of different wavelengths of light illustrated a high dependence on blue light and/or, less often, green light. New COF systems need to be designed to absorb further into the red-light region of the visible spectrum or increase the molar absorption coefficient to perform these transformations using green and longer wavelength light.

(2) A fair amount of COF photocatalysts in the literature require metals to perform the photocatalytic transformation, or at least to perform it efficiently. Strategies to incorporate superior organic units, or a combination of units, need to be addressed to move towards more sustainable practices to accomplish these transformations without the need for metals.

(3) The use of photosensitizers as additives or directly anchored to the COF is common, especially in photocatalytic coupling reactions. These photosensitizers are typically Rh, Ru, or Ir-based and are expensive and toxic. Again, for true metal-free systems these reagents need to be removed. Future work needs to be conducted to enable COFs to be more photoactive or absorb enough light to omit the use of photosensitizers.

(4) While COFs have been designed to lower band gaps by incorporating specific moieties or through the use of D–A systems, precise control over the band gap is not fully realized. Reducing the band gap is simpler in practice, but dictating the precise location of the valence and conduction bands is extremely difficult. The location of the conduction band is of key importance as it can control product distribution in photocatalytic applications. For instance, reducing carbon dioxide can result in many products (*i.e.* CO, HCOOH, MeOH, CH_4, and other hydrocarbons), and positioning the conduction band between the reduction energy levels of various products can limit what products can form, and the COF literature typically shows formation of only CO. Studies need to be per-

formed in order to understand the construction of COFs to precisely control valence band and conduction band energy positions.

(5) Although COFs are constructed through relatively stable covalent bonds and tested in aqueous, acidic, alkaline, and organic solvent conditions, their photochemical stability has not been well established. Most COF materials are not analysed for morphology or crystallinity change when subjected to high-intensity light (more than ambient) and, as discussed, some COFs were reported to lose crystallinity over time. Thus, more research is necessary to determine the long-term photostability of COFs after catalysis for prolonged periods. In the same vein, COFs with boron-based and C–N based linkages are quite dynamic in nature and result in high crystallinities, whereas olefin and ring linkages are more irreversible and typically have a partial or low degree of crystallinity. In saying this, studies need to be conducted to determine the relationship between amorphous, semi-crystalline, poly-crystalline, and single-crystalline COFs in respect to their photocatalytic activity.

(6) Similarly, COFs are lauded for their tunability and capacity to be constructed with different dimensionality and topology and morphology. However, there are limited examples showing a clear link to the structure–property relationship in COFs. As previously mentioned, there have been some studies on 2D *versus* 3D COFs, but more work is needed to look at differences in 3D *versus* 3D topologies (*i.e.* bor *versus* ctn), 2D AA *versus* AB stacking, and overall morphology (*e.g.* rods *versus* spheres *versus* wires, *etc.*) and how it affects the photocatalytic performance of COFs. Furthermore, there is an abundant need to make and prove how pore size, geometry, and chirality can make selective products in photocatalytic applications. For example, chiral COFs have been used in many catalytic applications, but chiral COF use in photocatalysis is rare.

(7) In general, there is a lack of research into the large-scale application of COFs. One reason is that the complex monomer design can make monomer synthesis difficult and low yielding, and therefore limit the monomer available for the COF synthesis. This is also partially due to the fact that the synthesis of COFs is often limited to smaller scale reactions to afford a crystalline material. Designing simpler yet effective systems as well as better synthetic methods can aid in large-scale reactions. Furthermore, when COFs have been employed as photocatalysts they are done on a small laboratory scale, and this needs to be extended to larger scale reactions including the use of larger batch reactors, flow reactors, and membrane reactors in order to make photocatalytic COFs industrially feasible.

Author contributions

J. G. D. developed the concept and structured the paper, screened the literature, made illustrations, and wrote Sections 1, 2, 4, 5, 6.5–6.7, 6.10–6.15, and 7. B. L. co-wrote Section 4 and wrote 6.1–6.4, 6.8 and 6.9. A. S. wrote Section 3. All authors contributed to revising the manuscript.

Data availability

No primary research results, software or code have been included and no new data were generated or analyzed as part of this review.

Conflicts of interest

There are no conflicts to declare.

Acknowledgements

We would like to acknowledge Chenhao Dang for making the generic COF stick structure that is in the TOC graphic.

References

1 Solar Irradiance, **https://sunclimate.gsfc.nasa.gov/article/solar-irradiance**, accessed June 2024.
2 Reference Air Mass 1.5 Spectra, **https://www.nrel.gov/grid/solar-resource/spectra-am1.5.html**, accessed June 2024.
3 J. Yu, T. Zhang and N. Wu, *Sol. RRL*, 2021, **5**, 2100252.
4 N. Serpone and A. V. Emeline, *J. Phys. Chem. Lett.*, 2012, **3**, 673–677.
5 A. D. McNaught, A. Wilkinson and A. D. Jenkins, *IUPAC Compendium of Chemical Terminology: The Gold Book*, International Union of Pure and Applied Chemistry, Research Triangle Park, NC, USA, 2006.
6 S. Zhu and D. Wang, *Adv. Energy Mater.*, 2017, **7**, 1700841.
7 X. Yang and D. Wang, *ACS Appl. Energy Mater.*, 2018, **1**, 6657–6693.
8 L. Wang and J. Yu, in *S-scheme Heterojunction Photocatalysts Fundamentals and Applications*, ed. J. Yu, L. Zhang, L. Wang and B. Zhu, Interface Science and Technology, Elsevier, Amsterdam, 1st edn, 2023, ch. 1, vol. 35, pp. 1–35.
9 H. Kisch and D. Bahnemann, *J. Phys. Chem. Lett.*, 2015, **6**, 1907–1910.
10 H. M. Chua, Q. Zhu, T. Tang, K. W. Shah and J. Xu, *Sol. Energy Mater. Sol. Cells*, 2019, **197**, 32–75.
11 C. Dai and B. Liu, *Energy Environ. Sci.*, 2020, **13**, 24–52.
12 T. Banerjee, F. Podjaski, J. Kröger, B. P. Biswal and B. V. Lotsch, *Nat. Rev. Mater.*, 2021, **6**, 168–190.
13 S. Yanagida, A. Kabumoto, K. Mizumoto, C. Pac and K. Yoshino, *J. Chem. Soc., Chem. Commun.*, 1985, **8**, 474–475.
14 A. Chaves, J. G. Azadani, H. Alsalman, D. R. da Costa, R. Frisenda, A. J. Chaves, S. H. Song, Y. D. Kim, D. He, J. Zhou, A. Castellanos-Gomez, F. M. Peeters, Z. Liu, C. L. Hinkle, S.-H. Oh, P. D. Ye, S. J. Koester, Y. H. Lee, P. Avouris, X. Wang and T. Low, *npj 2D Mater. Appl.*, 2020, **4**, 29.
15 E. Yousif and R. Haddad, *SpringerPlus*, 2013, **2**, 398.

16 M. Thangamuthu, Q. Ruan, P. O. Ohemeng, B. Luo, D. Jing, R. Godin and J. Tang, *Chem. Rev.*, 2022, **122**, 11778–11829.
17 N. Huang, P. Wang and D. Jiang, *Nat. Rev. Mater.*, 2016, **1**, 16068.
18 K. T. Tan, S. Ghosh, Z. Wang, F. Wen, D. Rodríguez-San-Miguel, J. Feng, N. Huang, W. Wang, F. Zamora, X. Feng, A. Thomas and D. Jiang, *Nat. Rev. Methods Primers*, 2023, **3**, 1.
19 M. S. Lohse and T. Bein, *Adv. Funct. Mater.*, 2018, **28**, 1705553.
20 K. Geng, T. He, R. Liu, S. Dalapati, K. T. Tan, Z. Li, S. Tao, Y. Gong, Q. Jiang and D. Jiang, *Chem. Rev.*, 2020, **120**, 8814–8933.
21 R. Liu, K. T. Tan, Y. Gong, Y. Chen, Z. Li, S. Xie, T. He, Z. Lu, H. Yanga and D. Jiang, *Chem. Soc. Rev.*, 2021, **50**, 120–242.
22 H. Wang, H. Wang, Z. Wang, L. Tang, G. Zeng, P. Xu, M. Chen, T. Xiong, C. Zhou, X. Li, D. Huang, Y. Zhu, Z. Wang and J. Tang, *Chem. Soc. Rev.*, 2020, **49**, 4135–4165.
23 C. Xia, K. O. Kirlikovali, T. H. C. Nguyen, X. C. Nguyen, Q. B. Tran, M. K. Duong, M. T. N. Dinh, D. L. T. Nguyen, P. Singh, P. Raizada, V.-H. Nguyen, S. Y. Kim, L. Singh, C. C. Nguyen, M. Shokouhimehr and Q. V. Le, *Coord. Chem. Rev.*, 2021, **446**, 214117.
24 T. Banerjee, K. Gottschlin, G. Savasci, C. Ochsenfeld and B. V. Lotsch, *ACS Energy Lett.*, 2018, **3**, 400–409.
25 B. B. Rath, S. Krause and B. V. Lotsch, *Adv. Funct. Mater.*, 2023, 2309060.
26 Z. Zhou, Y. Xiao, J. Tian, N. Nan, R. Song and J. Li, *J. Mater. Chem. A*, 2023, **11**, 3245–3261.
27 Y.-N. Gong, X. Guan and H.-L. Jiang, *Coord. Chem. Rev.*, 2023, **475**, 214889.
28 A. López-Magano, S. Daliran, A. R. Oveisi, R. Mas-Ballesté, A. Dhakshinamoorthy, J. Alemán, H. Garcia and R. Luque, *Adv. Mater.*, 2023, **35**, 2209475.
29 L. Qin, C. Ma, J. Zhang and T. Zhou, *Adv. Funct. Mater.*, 2024, 2401562.
30 Q. Guan, L.-L. Zhou and Y.-B. Dong, *Chem. Soc. Rev.*, 2022, **51**, 6307–6416.
31 A. P. Côté, A. I. Benin, N. W. Ockwig, M. O'Keeffe, A. J. Matzger and O. M. Yaghi, *Science*, 2005, **310**, 1166–1170.
32 J. R. Hunt, C. J. Doonan, J. D. LeVangie, A. P. Côté and O. M. Yaghi, *J. Am. Chem. Soc.*, 2008, **130**, 11872–11873.
33 K. T. Jackson, T. E. Reich and H. M. El-Kaderi, *Chem. Commun.*, 2012, **48**, 8823.
34 Y. Du, H. Yang, J. M. Whiteley, S. Wan, Y. Jin, S.-H. Lee and W. Zhang, *Angew. Chem., Int. Ed.*, 2016, **55**, 1737–1741.
35 F. J. Uribe-Romo, J. R. Hunt, H. Furukawa, C. Klöck, M. O'Keeffe and O. M. Yaghi, *J. Am. Chem. Soc.*, 2009, **131**, 4570–4571.
36 Z.-B. Zhou, X.-H. Han, Q.-Y. Qi, S.-X. Gan, D.-L. Ma and X. Zhao, *J. Am. Chem. Soc.*, 2022, **144**, 1138–1143.
37 X. Li, C. Zhang, S. Cai, X. Lei, V. Altoe, F. Hong, J. J. Urban, J. Ciston, E. M. Chan and Y. Liu, *Nat. Commun.*, 2018, **9**, 2998.
38 Y. Zhu, D. Huang, W. Wang, G. Liu, C. Ding and Y. Xiang, *Angew. Chem., Int. Ed.*, 2024, **63**, e202319909.
39 F. Haase, E. Troschke, G. Savasci, T. Banerjee, V. Duppel, S. Dörfler, M. M. J. Grundei, A. M. Burow, C. Ochsenfeld, S. Kaskel and B. V. Lotsch, *Nat. Commun.*, 2018, **9**, 2600.
40 C. Qian, L. Feng, W. L. Teo, J. Liu, W. Zhou, D. Wang and Y. Zhao, *Nat. Rev. Chem.*, 2022, **6**, 881–898.
41 S. Kandambeth, D. B. Shinde, M. K. Panda, B. Lukose, T. Heine and R. Banerjee, *Angew. Chem., Int. Ed.*, 2013, **52**, 13052–13056.
42 A. Halder, S. Karak, M. Addicoat, S. Bera, A. Chakraborty, S. H. Kunjattu, P. Pachfule, T. Heine and R. Banerjee, *Angew. Chem., Int. Ed.*, 2018, **57**, 5797–5802.
43 A. Halder, M. Ghosh, A. Khayu M, S. Bera, M. Addicoat, H. S. Sasmal, S. Karak, S. Kurungot and R. Banerjee, *J. Am. Chem. Soc.*, 2018, **140**, 10941–10945.
44 L. M. Lanni, R. W. Tilford, M. Bharathy and J. J. Lavigne, *J. Am. Chem. Soc.*, 2011, **133**, 13975–13983.
45 X. Wu, X. Han, Y. Liu, Y. Liu and Y. Cui, *J. Am. Chem. Soc.*, 2018, **140**, 16124–16133.
46 F. J. Uribe-Romo, C. J. Doonan, H. Furukawa, K. Oisaki and O. M. Yaghi, *J. Am. Chem. Soc.*, 2011, **133**, 11478–11481.
47 S. Dalapati, S. Jin, J. Gao, Y. Xu, A. Nagai and D. Jiang, *J. Am. Chem. Soc.*, 2013, **135**, 17310–17313.
48 C. R. DeBlase, K. E. Silberstein, T.-T. Truong, H. D. Abruña and W. R. Dichtel, *J. Am. Chem. Soc.*, 2013, **135**, 16821–16824.
49 A. Nagai, X. Chen, X. Feng, X. Ding, Z. Guo and D. Jiang, *Angew. Chem., Int. Ed.*, 2013, **52**, 3770–3774.
50 Q. Fang, Z. Zhuang, S. Gu, R. B. Kaspar, J. Zheng, J. Wang, S. Qiu and Y. Yan, *Nat. Commun.*, 2014, **5**, 4503.
51 D. Stewart, D. Antypov, M. S. Dyer, M. J. Pitcher, A. P. Katsoulidis, P. A. Chater, F. Blanc and M. J. Rosseinsky, *Nat. Commun.*, 2017, **8**, 1102.
52 X. Zhuang, W. Zhao, F. Zhang, Y. Cao, F. Liu, S. Bi and X. Feng, *Polym. Chem.*, 2016, **7**, 4176–4181.
53 H. Lyu, C. S. Diercks, C. Zhu and O. M. Yaghi, *J. Am. Chem. Soc.*, 2019, **141**, 6848–6852.
54 A. Acharjya, P. Pachfule, J. Roeser, F.-J. Schmitt and A. Thomas, *Angew. Chem.*, 2019, **131**, 15007–15012.
55 D. L. Pastoetter, S. Xu, M. Borrelli, M. Addicoat, B. P. Biswal, S. Paasch, A. Dianat, H. Thomas, R. Berger, S. Reineke, E. Brunner, G. Cuniberti, M. Richter and X. Feng, *Angew. Chem., Int. Ed.*, 2020, **59**, 23620–23625.
56 X. Wu, L. Zong and N. Huang, *Chem. Commun.*, 2024, **60**, 320–323.
57 J. Guo, Y. Xu, S. Jin, L. Chen, T. Kaji, Y. Honsho, M. A. Addicoat, J. Kim, A. Saeki, H. Ihee, S. Seki, S. Irle, M. Hiramoto, J. Gao and D. Jiang, *Nat. Commun.*, 2013, **4**, 2736.
58 B. Zhang, M. Wei, H. Mo, X. Pei, S. A. Alshmimri, J. A. Reimer and O. M. Yaghi, *J. Am. Chem. Soc.*, 2018, **140**, 12715–12719.

59 P.-F. Wei, M.-Z. Qi, Z.-P. Wang, S.-Y. Ding, W. Yu, Q. Liu, L.-K. Wang, H.-Z. Wang, W.-K. An and W. Wang, *J. Am. Chem. Soc.*, 2018, **140**, 4623–4631.
60 K. C. Ranjeesh, R. Illathvalappil, S. D. Veer, J. Peter, V. C. Wakchaure, Goudappagouda, K. V. Raj, S. Kurungot and S. S. Babu, *J. Am. Chem. Soc.*, 2019, **141**, 14950–14954.
61 K. Wang, Z. Jia, Y. Bai, X. Wang, S. E. Hodgkiss, L. Chen, S. Y. Chong, X. Wang, H. Yang, Y. Xu, F. Feng, J. W. Ward and A. I. Cooper, *J. Am. Chem. Soc.*, 2020, **142**, 11131–11138.
62 Y. Meng, Y. Luo, J.-L. Shi, H. Ding, X. Lang, W. Chen, A. Zheng, J. Sun and C. Wang, *Angew. Chem., Int. Ed.*, 2020, **59**, 3624–3629.
63 K. Wang, X. Kang, C. Yuan, X. Han, Y. Liu and Y. Cui, *Angew. Chem., Int. Ed.*, 2021, **60**, 19466–19476.
64 P. Li, F. Ge, Y. Yang, T. Wang, X. Zhang, K. Zhang and J. Shen, *Angew. Chem., Int. Ed.*, 2024, **63**, e202319885.
65 C. Liu, D.-L. Ma, P.-J. Tian, C. Jia, Q.-Y. Qi, G.-F. Jiang and X. Zhao, *J. Mater. Chem. A*, 2024, **12**, 16063–16069.
66 X. Shen and B. Yan, *J. Mater. Chem. A*, 2024, **12**, 6455–6464.
67 K. Lin, J. Wang, S. Qiao and Z. Guo, *ACS Sustainable Chem. Eng.*, 2024, **12**, 6719–6727.
68 L. Song, W. Gao, S. Jiang, Y. Yang, W. Chu, X. Cao, B. Sun, L. Cui and C.-Y. Zhang, *Nano Lett.*, 2024, **24**, 6312–6319.
69 H. M. El-Kaderi, J. R. Hunt, J. L. Mendoza-Cortés, A. P. Côté, R. E. Taylor, M. O'Keeffe and O. M. Yaghi, *Science*, 2007, **316**, 268–272.
70 G. Lin, H. Ding, D. Yuan, B. Wang and C. Wang, *J. Am. Chem. Soc.*, 2016, **138**, 3302–3305.
71 Y. Zhang, J. Duan, D. Ma, P. Li, S. Li, H. Li, J. Zhou, X. Ma, X. Feng and B. Wang, *Angew. Chem., Int. Ed.*, 2017, **56**, 16313–16317.
72 T. Ma, E. A. Kapustin, S. X. Yin, L. Liang, Z. Zhou, J. Niu, L.-H. Li, Y. Wang, J. Su, J. Li, X. Wang, W. D. Wang, W. Wang, J. Sun and O. M. Yaghi, *Science*, 2018, **361**, 48–52.
73 Y. Xie, J. Li, C. Lin, B. Gui, C. Ji, D. Yuan, J. Sun and C. Wang, *J. Am. Chem. Soc.*, 2021, **143**, 7279–7284.
74 Y. Liu, J. Li, J. Lv, Z. Wang, J. Suo, J. Ren, J. Liu, D. Liu, Y. Wang, V. Valtchev, S. Qiu, D. Zhang and Q. Fang, *J. Am. Chem. Soc.*, 2023, **145**, 9679–9685.
75 X. Kang, X. Han, C. Yuan, C. Cheng, Y. Liu and Y. Cui, *J. Am. Chem. Soc.*, 2020, **142**, 16346–16356.
76 H. Li, J. Ding, X. Guan, F. Chen, C. Li, L. Zhu, M. Xue, D. Yuan, V. Valtchev, Y. Yan, S. Qiu and Q. Fang, *J. Am. Chem. Soc.*, 2020, **142**, 13334.
77 H. Li, F. Chen, X. Guan, J. Li, C. Li, B. Tang, V. Valtchev, Y. Yan, S. Qiu and Q. Fang, *J. Am. Chem. Soc.*, 2021, **143**, 2654–2659.
78 Z. Li, L. Sheng, C. Hsueh, X. Wang, H. Cui, H. Gao, Y. Wu, J. Wang, Y. Tang, H. Xu and X. He, *Chem. Mater.*, 2021, **33**, 9618–9623.
79 J. Chang, F. Chen, H. Li, J. Suo, H. Zheng, J. Zhang, Z. Wang, L. Zhu, V. Valtchev, S. Qiu and Q. Fang, *Nat. Commun.*, 2024, **15**, 813.
80 Y. Lan, X. Han, M. Tong, H. Huang, Q. Yang, D. Liu, X. Zhao and C. Zhong, *Nat. Commun.*, 2018, **9**, 5274.
81 H. L. Nguyen, C. Gropp, Y. Ma, C. Zhu and O. M. Yaghi, *J. Am. Chem. Soc.*, 2020, **142**, 20335–20339.
82 S. Das, T. Sekine, H. Mabuchi, T. Irie, J. Sakai, Y. Zhao, Q. Fang and Y. Negishi, *ACS Appl. Mater. Interfaces*, 2022, **14**, 48045–48051.
83 F. Jin, E. Lin, T. Wang, S. Geng, T. Wang, W. Liu, F. Xiong, Z. Wang, Y. Chen, P. Cheng and Z. Zhang, *J. Am. Chem. Soc.*, 2022, **144**, 5643–5652.
84 Z. Shan, M. Wu, D. Zhu, X. Wu, K. Zhang, R. Verduzco and G. Zhang, *J. Am. Chem. Soc.*, 2022, **144**, 5728–5733.
85 S. Das, H. Mabuchi, T. Irie, K. Sasaki, M. Nozaki, R. Tomioka, D. Wen, Y. Zhao, T. Ben and Y. Negishi, *Small*, 2024, **20**, 2307666.
86 W. Liu, K. Wang, X. Zhan, Z. Liu, X. Yang, Y. Jin, B. Yu, L. Gong, H. Wang, D. Qi, D. Yuan and J. Jiang, *J. Am. Chem. Soc.*, 2023, **145**, 8141–8149.
87 D. Zhu, Y. Zhu, Y. Chen, Q. Yan, H. Wu, C.-Y. Liu, X. Wang, L. B. Alemany, G. Gao, T. P. Senftle, Y. Peng, X. Wu and R. Verduzco, *Nat. Commun.*, 2023, **14**, 2865.
88 Y. Liu, P. Chen, Y. Wang, J. Suo, J. Ding, L. Zhu, V. Valtchev, Y. Yan, S. Qiu, J. Sun and Q. Fang, *Angew. Chem., Int. Ed.*, 2022, **61**, e202203584.
89 X. Wang, M. Bahri, Z. Fu, M. A. Little, L. Liu, H. Niu, N. D. Browning, S. Y. Chong, L. Chen, J. W. Ward and A. I. Cooper, *J. Am. Chem. Soc.*, 2021, **143**, 15011–15016.
90 O. Yahiaoui, A. N. Fitch, F. Hoffmann, M. Fröba, A. Thomas and J. Roeser, *J. Am. Chem. Soc.*, 2018, **140**, 5330–5333.
91 Y. Liu, Y. Ma, J. Yang, C. S. Diercks, N. Tamura, F. Jin and O. M. Yaghi, *J. Am. Chem. Soc.*, 2018, **140**, 16015–16019.
92 H.-S. Lu, W.-K. Han, X. Yan, C.-J. Chen, T. Niu and Z.-G. Gu, *Angew. Chem., Int. Ed.*, 2021, **60**, 17881–17886.
93 W.-K. Han, H.-S. Lu, J.-X. Fu, X. Liu, X. Zhu, X. Yan, J. Zhang, Y. Jiang, H. Dong and Z.-G. Gu, *Chem. Eng. J.*, 2022, **449**, 137802.
94 M. Martínez-Abadía, K. Strutyński, B. Lerma-Berlanga, C. T. Stoppiello, A. N. Khlobystov, C. Martí-Gastaldo, A. Saeki, M. Melle-Franco and A. Mateo-Alonso, *Angew. Chem., Int. Ed.*, 2021, **60**, 9941–9946.
95 X. Xu, P. Cai, H. Chen, H.-C. Zhou and N. Huang, *J. Am. Chem. Soc.*, 2022, **144**, 18511–18517.
96 F. Jin, H. L. Nguyen, Z. Zhong, X. Han, C. Zhu, X. Pei, Y. Ma and O. M. Yaghi, *J. Am. Chem. Soc.*, 2022, **144**, 1539–1544.
97 M. Wu, Z. Shan, J. Wang, T. Liu and G. Zhang, *Chem. Eng. J.*, 2023, **454**, 140121.
98 Reticular Chemistry Structure Resource Search 3-Periodic, **https://rcsr.net/nets**, accessed 6/30/2024.
99 Z. Guo, Z. Zhang and J. Sun, *Adv. Mater.*, 2024, **3**, e2312889.
100 R. Roy and A. M. Evans, *Commun. Mater.*, 2024, **5**, 102.
101 D. Zhu, J.-J. Zhang, X. Wu, Q. Yan, F. Liu, Y. Zhu, X. Gao, M. M. Rahman, B. I. Yakobson, P. M. Ajayan and R. Verduzco, *Chem. Sci.*, 2022, **13**, 9655–9667.

102 D. Zhu and R. Verduzco, *ACS Appl. Mater. Interfaces*, 2020, **12**, 33121–33127.
103 B. Diaz de Grenu, J. Torres, J. García-González, S. Muñoz-Pina, R. de Los Reyes, A. M. Costero, P. Amorós and J. V. Ros-Lis, *ChemSusChem*, 2021, **14**, 208–233.
104 A. de la Hoz, A. Díaz-Ortiz and P. Prieto, in *Alternative Energy Sources for Green Chemistry*, ed. G. Stefanidis and A. Stankiewicz, The Royal Society of Chemistry, Cambridge, 1st edn, 2016, ch. 1, pp. 1–33.
105 N. L. Campbell, R. Clowes, L. K. Ritchie and A. I. Cooper, *Chem. Mater.*, 2009, **21**, 204–206.
106 H. Wei, S. Chai, N. Hu, Z. Yang, L. Wei and L. Wang, *Chem. Commun.*, 2015, **51**, 12178–12181.
107 S.-T. Yang, J. Kim, H.-Y. Cho, S. Kim and W.-S. Ahn, *RSC Adv.*, 2012, **2**, 10179–10181.
108 J. Yoo, S. Lee, S. Hirata, C. Kim, C. K. Lee, T. Shiraki, N. Nakashima and J. K. Shim, *Chem. Lett.*, 2015, **44**, 560–562.
109 W. Zhao, P. Yan, H. Yang, M. Bahri, A. M. James, H. Chen, L. Liu, B. Li, Z. Pang, R. Clowes, N. D. Browning, J. W. Ward, Y. Wu and A. I. Cooper, *Nat. Synth.*, 2022, **1**, 87–95.
110 B. P. Biswal, S. Chandra, S. Kandambeth, B. Lukose, T. Heine and R. Banerjee, *J. Am. Chem. Soc.*, 2013, **135**, 5328–5331.
111 X. Wang, R. Ma, L. Hao, Q. Wu, C. Wang and Z. Wang, *J. Chromatogr. A*, 2018, **1551**, 1–9.
112 N. Brown, Z. Alsudairy, R. Behera, F. Akram, K. Chen, K. Smith-Petty, B. Motley, S. Williams, W. Huang, C. Ingrama and X. Li, *Green Chem.*, 2023, **25**, 6287–6296.
113 D. B. Shinde, H. B. Aiyappa, M. Bhadra, B. P. Biswal, P. Wadge, S. Kandambeth, B. Garai, T. Kundu, S. Kurungot and R. Banerjee, *J. Mater. Chem. A*, 2016, **4**, 2682–2690.
114 Y. Peng, G. Xu, Z. Hu, Y. Cheng, C. Chi, D. Yuan, H. Cheng and D. Zhao, *ACS Appl. Mater. Interfaces*, 2016, **8**, 18505–18512.
115 S. Kim and H. C. Choi, *Commun. Chem.*, 2019, **2**, 60.
116 P. Kuhn, M. Antonietti and A. Thomas, *Angew. Chem., Int. Ed.*, 2008, **47**, 3450–3453.
117 J. Maschita, T. Banerjee, G. Savasci, F. Haase, C. Ochsenfeld and B. V. Lotsch, *Angew. Chem., Int. Ed.*, 2020, **59**, 15750–15758.
118 K. S. Song, P. W. Fritz, D. F. Abbott, L. N. Poon, C. M. Caridade, F. Gándara, V. Mougel and A. Coskun, *Angew. Chem., Int. Ed.*, 2023, **62**, e202309775.
119 X. Guan, Y. Ma, H. Li, Y. Yusran, M. Xue, Q. Fang, Y. Yan, V. Valtchev and S. Qiu, *J. Am. Chem. Soc.*, 2018, **140**, 4494–4498.
120 M. Sawatzki-Park, S.-J. Wang, H. Kleemann and K. Leo, *Chem. Rev.*, 2023, **123**, 8232–8250.
121 T. Haggren, H. H. Tan and C. Jagadish, *Acc. Mater. Res.*, 2023, **4**, 1046–1056.
122 H. Wang, Z. Zeng, P. Xu, L. Li, G. Zeng, R. Xiao, Z. Tang, D. Huang, L. Tang, C. Lai, D. Jiang, Y. Liu, H. Yi, L. Qin, S. Ye, X. Ren and W. Tang, *Chem. Soc. Rev.*, 2019, **48**, 488–516.
123 K. Dey, M. Pal, K. C. Rout, H. S. Kunjattu, A. Das, R. Mukherjee, U. K. Kharul and R. Banerjee, *J. Am. Chem. Soc.*, 2017, **139**, 13083–13091.
124 M. Matsumoto, L. Valentino, G. M. Stiehl, H. B. Balch, A. R. Corcos, F. Wang, D. C. Ralph, B. J. Mariñas and W. R. Dichtel, *Chem*, 2018, **4**, 308–317.
125 Q. Hao, C. Zhao, B. Sun, C. Lu, J. Liu, M. Liu, L.-J. Wan and D. Wang, *J. Am. Chem. Soc.*, 2018, **140**, 12152–12158.
126 J. I. Feldblyum, C. H. McCreery, S. C. Andrews, T. Kurosawa, E. J. G. Santos, V. Duong, L. Fang, A. L. Ayzner and Z. N. Bao, *Chem. Commun.*, 2015, **51**, 13894–13897.
127 Z. Ou, B. Liang, Z. Liang, F. Tan, X. Dong, L. Gong, P. Zhao, H. Wang, Y. Zou, Y. Xia, X. Chen, W. Liu, H. Qi, U. Kaiser and Z. Zheng, *J. Am. Chem. Soc.*, 2022, **144**, 3233–3241.
128 Y. Yang, Y. Chen, F. Izquierdo-Ruiz, C. Schäfer, M. Rahm and K. Börjesson, *Nat. Commun.*, 2023, **14**, 220.
129 D. Wu, Q. Che, H. He, M. E. El-Khouly, S. Huang, X. Zhuang, B. Zhang and Y. Chen, *ACS Mater. Lett.*, 2023, **5**, 874–883.
130 X. Shi, D. Ma, F. Xu, Z. Zhang and Y. Wang, *Chem. Sci.*, 2020, **11**, 989–996.
131 Y. Qu, Y. Zha, X. Du, S. Xu, M. Zhang, L. Xu and H. Jia, *ACS Appl. Polym. Mater.*, 2022, **4**, 7528–7536.
132 Y.-B. Zhang, J. Su, H. Furukawa, Y. Yun, F. Gándara, A. Duong, X. Zou and O. M. Yaghi, *J. Am. Chem. Soc.*, 2013, **135**, 16336–16339.
133 D. Beaudoin, T. Maris and J. D. Wuest, *Nat. Chem.*, 2013, **5**, 830–834.
134 C. Kang, K. Yang, Z. Zhang, A. K. Usadi, D. C. Calabro, L. S. Baugh, Y. Wang, J. Jiang, X. Zou, Z. Huang and D. Zhao, *Nat. Commun.*, 2022, **13**, 1370.
135 L. Peng, Q. Guo, C. Song, S. Ghosh, H. Xu, L. Wang, D. Hu, L. Shi, L. Zhao, Q. Li, T. Sakurai, H. Yan, S. Seki, Y. Liu and D. Wei, *Nat. Commun.*, 2021, **12**, 5077.
136 Y. Yin, Y. Zhang, X. Zhou, B. Gui, G. Cai, J. Sun and C. Wang, *J. Am. Chem. Soc.*, 2023, **145**, 22329–22334.
137 L. Liang, Y. Qiu, W. D. Wang, J. Han, Y. Luo, W. Yu, G.-L. Yin, Z.-P. Wang, L. Zhang, J. Ni, J. Niu, J. Sun, T. Ma and W. Wang, *Angew. Chem., Int. Ed.*, 2020, **59**, 17991–17995.
138 H.-S. Xu, Y. Luo, X. Li, P. Z. See, Z. Chen, T. Ma, L. Liang, K. Leng, I. Abdelwahab, L. Wang, R. Li, X. Shi, Y. Zhou, X. F. Lu, X. Zhao, C. Liu, J. Sun and K. P. Loh, *Nat. Commun.*, 2020, **11**, 1434.
139 Z. Zhou, L. Zhang, Y. Yang, I. J. Vitorica-Yrezabal, H. Wang, F. Tan, L. Gong, Y. Li, P. Chen, X. Dong, Z. Liang, J. Yang, C. Wang, Y. Hong, Y. Qiu, A. Gölzhäuser, X. Chen, H. Qi, S. Yang, W. Liu, J. Sun and Z. Zheng, *Nat. Chem.*, 2023, **15**, 841–847.
140 A. M. Evans, L. R. Parent, N. C. Flanders, R. P. Bisbey, E. Vitaku, M. S. Kirschner, R. D. Schaller, L. X. Chen, N. C. Gianneschi and W. R. Dichtel, *Science*, 2018, **361**, 52–57.
141 B. Yu, R.-B. Lin, G. Xu, Z.-H. Fu, H. Wu, W. Zhou, S. Lu, Q.-W. Li, Y. Jin, J.-H. Li, Z. Zhang, H. Wang, Z. Yan, X. Liu,

K. Wang, B. Chen and J. Jiang, *Nat. Chem.*, 2024, **16**, 114–121.
142 J. Han, J. Feng, J. Kang, J.-M. Chen, X.-Y. Du, S.-Y. Ding, L. Liang and W. Wang, *Science*, 2024, **383**, 1014–1019.
143 N. A. Rejali, M. Dinari and Y. Wang, *Chem. Commun.*, 2023, **59**, 11631–11647.
144 J. L. Segura, S. Royuela and M. M. Ramos, *Chem. Soc. Rev.*, 2019, **48**, 3903–3945.
145 S.-Y. Ding, J. Gao, Q. Wang, Y. Zhang, W.-G. Song, C.-Y. Su and W. Wang, *J. Am. Chem. Soc.*, 2011, **133**, 19816–19822.
146 I. Romero-Muñiz, A. Mavrandonakis, P. Albacete, A. Vega, V. Briois, F. Zamora and A. E. Platero-Prats, *Angew. Chem., Int. Ed.*, 2020, **59**, 13013–13020.
147 J. Hu, H. Mehrabi, Y.-S. Meng, M. Taylor, J.-H. Zhan, Q. Yan, M. Benamara, R. H. Coridan and H. Beyzavi, *Chem. Sci.*, 2021, **12**, 7930–7936.
148 X. Han, J. Zhang, J. Huang, X. Wu, D. Yuan, Y. Liu and Y. Cui, *Nat. Commun.*, 2018, **9**, 1294.
149 P. Sarkar, A. Hazra Chowdhury, S. Biswas, A. Khan and S. M. Islam, *Mater. Today Chem.*, 2021, **21**, 100509.
150 Y. Li, X. Guo, X. Li, M. Zhang, Z. Jia, Y. Deng, Y. Tian, S. Li and L. Ma, *Angew. Chem., Int. Ed.*, 2020, **59**, 4168–4175.
151 G. Chen, H.-H. Lan, S.-L. Cai, B. Sun, X.-L. Li, Z.-H. He, S.-R. Zheng, J. Fan, Y. Liu and W.-G. Zhang, *ACS Appl. Mater. Interfaces*, 2019, **11**, 12830–12837.
152 X. Kan, J.-C. Wang, J.-L. Kan, J.-Y. Shang, H. Qiao and Y.-B. Dong, *Inorg. Chem.*, 2021, **60**, 3393–3400.
153 C. Qian, Q.-Y. Qi, G.-F. Jiang, F.-Z. Cui, Y. Tian and X. Zhao, *J. Am. Chem. Soc.*, 2017, **139**, 6736–6743.
154 J. Maschita, T. Banerjee and B. V. Lotsch, *Chem. Mater.*, 2022, **34**, 2249–2258.
155 Z.-B. Zhou, P.-J. Tian, J. Yao, Y. Lu, Q.-Y. Qi and X. Zhao, *Nat. Commun.*, 2022, **13**, 2180.
156 A. Nagai, Z. Guo, X. Feng, S. Jin, X. Chen, X. Ding and D. Jiang, *Nat. Commun.*, 2011, **2**, 536.
157 N. Huang, R. Krishna and D. Jiang, *J. Am. Chem. Soc.*, 2015, **137**, 7079–7082.
158 L. Chen, K. Furukawa, J. Gao, A. Nagai, T. Nakamura, Y. Dong and D. Jiang, *J. Am. Chem. Soc.*, 2014, **136**, 9806–9809.
159 D. N. Bunck and W. R. Dichtel, *Chem. Commun.*, 2013, **49**, 2457–2459.
160 Q. Sun, B. Aguila, J. Perman, L. D. Earl, C. W. Abney, Y. Cheng, H. Wei, N. Nguyen, L. Wojtas and S. Ma, *J. Am. Chem. Soc.*, 2017, **139**, 2786–2793.
161 Q. Sun, B. Aguila, J. A. Perman, T. Butts, F.-S. Xiao and S. Ma, *Chem*, 2018, **4**, 1726–1739.
162 N. Huang, X. Chen, R. Krishna and D. Jiang, *Angew. Chem., Int. Ed.*, 2015, **54**, 2986–2990.
163 B. Dong, L. Wang, S. Zhao, R. Ge, X. Song, Y. Wang and Y. Gao, *Chem. Commun.*, 2016, **52**, 7082–7085.
164 S. Rager, M. Dogru, V. Werner, A. Gavryushin, M. Götz, H. Engelke, D. D. Medina, P. Knochel and T. Bein, *CrystEngComm*, 2017, **19**, 4886–4891.
165 P. Nitschke, N. Lokesh and R. M. Gschwind, *Prog. Nucl. Magn. Reson. Spectrosc.*, 2019, **114–115**, 86–134.
166 C. Kranz and M. Wächtler, *Chem. Soc. Rev.*, 2021, **50**, 1407–1437.
167 G.-B. Wang, Y.-J. Wang, J.-L. Kan, K.-H. Xie, H.-P. Xu, F. Zhao, M.-C. Wang, Y. Geng and Y.-B. Dong, *J. Am. Chem. Soc.*, 2023, **145**, 4951–4956.
168 J. Ø. Duus, C. H. Gotfredsen and K. Bock, *Chem. Rev.*, 2000, **100**, 4589–4614.
169 M. W. Lodewyk, M. R. Siebert and D. J. Tantillo, *Chem. Rev.*, 2012, **112**, 1839–1862.
170 R. M. Maggio, N. L. Calvo, S. E. Vignaduzzo and T. S. Kaufman, *J. Pharm. Biomed. Anal.*, 2014, **101**, 102–122.
171 S. Singh, T. Handa, M. Narayanam, A. Sahu, M. Junwal and R. P. Shah, *J. Pharm. Biomed. Anal.*, 2012, **69**, 148–173.
172 S. K. Bharti and R. Roy, *TrAC, Trends Anal. Chem.*, 2012, **35**, 5–26.
173 U. Holzgrabe, *Prog. Nucl. Magn. Reson. Spectrosc.*, 2010, **57**, 229–240.
174 Y. Ben-Tal, P. J. Boaler, H. J. A. Dale, R. E. Dooley, N. A. Fohn, Y. Gao, A. García-Domínguez, K. M. Grant, A. M. R. Hall, H. L. D. Hayes, M. M. Kucharski, R. Wei and G. C. Lloyd-Jones, *Prog. Nucl. Magn. Reson. Spectrosc.*, 2022, **129**, 28–106.
175 T. Blasco, *Chem. Soc. Rev.*, 2010, **39**, 4685–4702.
176 C. Feldmeier, H. Bartling, E. Riedle and R. M. Gschwind, *J. Magn. Reson.*, 2013, **232**, 39–44.
177 A. Seegerer, P. Nitschke and R. M. Gschwind, *Angew. Chem., Int. Ed.*, 2018, **57**, 7493–7497.
178 D. Lehnherr, Y. Ji, A. J. Neel, R. D. Cohen, A. P. J. Brunskill, J. Yang and M. Reibarkh, *J. Am. Chem. Soc.*, 2018, **140**, 13843–13853.
179 Y. Ji, D. A. DiRocco, J. Kind, C. M. Thiele, R. M. Gschwind and M. Reibarkh, *ChemPhotoChem*, 2019, **3**, 984–992.
180 X. L. Wang, W. Liu, Y.-Y. Yu, Y. Song, W. Q. Fang, D. Wei, X.-Q. Gong, Y.-F. Yao and H. G. Yang, *Nat. Commun.*, 2016, **7**, 11918.
181 H. Parastar, J. R. Radovic, M. Jalali-Heravi, S. Diez, J. M. Bayona and R. Tauler, *Anal. Chem.*, 2011, **83**, 9289–9297.
182 P. Jonsson, A. I. Johansson, J. Gullberg, J. Trygg, J. A, B. Grung, S. Marklund, M. Sjöström, H. Antti and T. Moritz, *Anal. Chem.*, 2005, **77**, 5635–5642.
183 D. A. Lambropoulou, M. D. Hernando, I. K. Konstantinou, E. M. Thurman, I. Ferrer, T. A. Albanis and A. R. Fernandez-Alba, *J. Chromatogr. A*, 2008, **1183**, 38–48.
184 C. Sahoo and A. K. Gupta, *J. Environ. Sci. Health, Part A: Toxic/Hazard. Subst. Environ. Eng.*, 2015, **50**, 1333–1341.
185 B. R. Miller, R. F. Weiss, P. K. Salameh, T. Tanhua, B. R. Greally, J. Muhle and P. G. Simmonds, *Anal. Chem.*, 2008, **80**, 1536–1545.
186 J. Hong, W. Zhang, J. Rena and R. Xu, *Anal. Methods*, 2013, **5**, 1086–1097.
187 R. Zaffaroni, D. Ripepi, J. Middelkoop and F. M. Mulder, *ACS Energy Lett.*, 2020, **5**, 3773–3777.
188 J. Šťávová, D. C. Stahl, W. S. Seames and A. Kubátová, *J. Chromatogr. A*, 2012, **1224**, 79–88.

189 N. Ragunathan, K. A. Krock, C. Klawun, T. A. Sasaki and C. L. Wilkins, *J. Chromatogr. A*, 1999, **856**, 349–397.
190 C. F. Poole, *J. Chromatogr. A*, 2015, **1421**, 137–153.
191 E. D. Pellizzari, *J. Chromatogr. A*, 1974, **98**, 323–361.
192 M. B. Mitchell, in *Structure-Property Relations in Polymers*, ed. M. W. Urban and C. D. Craver, American Chemical Society, Washington, DC, 1993, ch. 13, vol. 236, pp. 351–375.
193 E. Groppo, S. Rojas-Buzo and S. Bordiga, *Chem. Rev.*, 2023, **123**, 12135–12169.
194 I. M. Hill, S. Hanspal, Z. D. Young and R. J. Davis, *J. Phys. Chem. C*, 2015, **119**, 9186–9197.
195 F. Zaera, *Chem. Soc. Rev.*, 2014, **43**, 7624–7663.
196 F. C. Meunier, *React. Chem. Eng.*, 2016, **1**, 134–141.
197 C. Lamberti, A. Zecchina, E. Groppo and S. Bordiga, *Chem. Soc. Rev.*, 2010, **39**, 4951–5001.
198 B. Hauchecorne, D. Terrens, S. Verbruggen, J. A. Martens, H. Van Langenhove, K. Demeestere and S. Lenaerts, *Appl. Catal., B*, 2011, **106**, 630–638.
199 Q. Zhang, S. Mo, J. Li, Y. Sun, M. Zhang, P. Chen, M. Fu, J. Wu, L. Chen and D. Ye, *Catal. Sci. Technol.*, 2019, **9**, 4538–4551.
200 B. N. Choi, J. Y. Seo, Z. An, P. J. Yoo and C.-H. Chung, *Chem. Eng. J.*, 2022, **430**, 132807.
201 Q. Li, Z.-h. Yue, M.-s. Shan, Y.-l. Li, Y. Liu, Y.-j. Hao and F.-t. Li, *Appl. Catal., B*, 2023, **330**, 122628.
202 Y. Fan, Y. Jiang, H. Lin, J. Li, Y. Xie, A. Chen, S. Li, D. Han, L. Niu and Z. Tang, *Nat. Commun.*, 2024, **15**, 4679.
203 J. T. Schneider, D. S. Firak, R. R. Ribeiro and P. Peralta-Zamora, *Phys. Chem. Chem. Phys.*, 2020, **22**, 15723–15733.
204 A. Trenczek-Zajac, M. Synowiec, K. Zakrzewska, K. Zazakowny, K. Kowalski, A. Dziedzic and M. Radecka, *ACS Appl. Mater. Interfaces*, 2022, **14**, 38255–38269.
205 C. Carlsson, B. Fégeant, E. Svensson, L. Wiklund and M. Jonsson, *J. Phys. Chem. C*, 2022, **126**, 12435–12440.
206 L. Ding, Y. Hou, H. Liu, J. Peng, Z. Cao, Y. Zhang, B. Wang, X. Cao, Y. Chang, T. Wang and G. Liu, *ACS ES&T Water*, 2023, **3**, 3534–3543.
207 L. Wang, B. Li, D. D. Dionysiou, B. Chen, J. Yang and J. Li, *Environ. Sci. Technol.*, 2022, **56**, 3386–3396.
208 Y. Du and J. Rabani, *J. Phys. Chem. B*, 2003, **107**, 11970–11978.
209 G. Žerjav, A. Albreht, I. Vovk and A. Pintar, *Appl. Catal., A*, 2020, **598**, 117566.
210 C. D. Georgiou, H. J. Sun, C. P. McKay, K. Grintzalis, I. Papapostolou, D. Zisimopoulos, K. Panagiotidis, G. Zhang, E. Koutsopoulou, G. E. Christidis and I. Margiolaki, *Nat. Commun.*, 2015, **6**, 7100.
211 O. A. Badary, R. A. Taha, A. M. G. El-Din and M. H. Abdel-Wahab, *Drug Chem. Toxicol.*, 2003, **26**, 87–98.
212 M. Iwamura and N. Inamoto, *Bull. Chem. Soc. Jpn.*, 1967, **40**, 703.
213 J. R. Harbour, V. Chew and J. R. Bolton, *Can. J. Chem.*, 1974, **52**, 3549–3553.
214 C. Ouannes and T. Wilson, *J. Am. Chem. Soc.*, 1968, **90**, 6527–6528.
215 J. R. Harbour and S. L. Issler, *J. Am. Chem. Soc.*, 1982, **104**, 903–905.
216 Y. Lion, M. Delmelle and A. Van De Vorst, *Nature*, 1976, **263**, 442–443.
217 Y. Pellegrin and F. Odobel, *C. R. Chim.*, 2017, **20**, 283–295.
218 J. Liu, Y. Zou, B. Jin, K. Zhang and J. H. Park, *ACS Energy Lett.*, 2019, **4**, 3018–3027.
219 X. Zhao and Y. Liu, *J. Am. Chem. Soc.*, 2021, **143**, 9423–9428.
220 W. Mtangi, F. Tassinari, K. Vankayala, A. V. Jentzsch, B. Adelizzi, A. R. A. Palmans, C. Fontanesi, E. W. Meijer and R. Naaman, *J. Am. Chem. Soc.*, 2017, **139**, 2794–2798.
221 K. Wenderich, W. Kwak, A. Grimm, G. J. Kramer, G. Mul and B. Mei, *Sustainable Energy Fuels*, 2020, **4**, 3143–3156.
222 S. R. Lingampalli, M. M. Ayyub and C. N. R. Rao, *ACS Omega*, 2017, **2**, 2740–2748.
223 J. Albero, Y. Peng and H. García, *ACS Catal.*, 2020, **10**, 5734–5749.
224 J. Wu, Y. Huang, W. Ye and Y. Li, *Adv. Sci.*, 2017, **4**, 1700194.
225 H. Hou, X. Zeng and X. Zhang, *Angew. Chem., Int. Ed.*, 2020, **59**, 17356–17376.
226 S. Goldstein, D. Aschengrau, Y. Diamant and J. Rabani, *Environ. Sci. Technol.*, 2007, **41**, 7486–7490.
227 K. Sahel, L. Elsellami, I. Mirali, F. Dappozze, M. Bouhent and C. Guillard, *Appl. Catal., B*, 2016, **188**, 106–112.
228 S. P. Pitre, C. D. McTiernan, H. Ismaili and J. C. Scaiano, *J. Am. Chem. Soc.*, 2013, **135**, 13286–13289.
229 Y.-Q. Zou, J.-R. Chen, X.-P. Liu, L.-Q. Lu, R. L. Davis, K. A. Jørgensen and W.-J. Xiao, *Angew. Chem.*, 2012, **124**, 808–812.
230 L. Wei, J. Zhang and L. Xu, *ACS Sustainable Chem. Eng.*, 2020, **8**, 13894–13899.
231 K. Sato, M. Hyodo, M. Aoki, X.-Q. Zheng and R. Noyori, *Tetrahedron*, 2001, **57**, 2469–2476.
232 M. Assis, A. F. Gouveia, L. K. Ribeiro, M. A. Ponce, M. S. Churio, O. N. Oliveira, Jr., L. H. Mascaro, E. Longo, R. Llusar, E. Guillamon and J. Andres, *Appl. Catal., A*, 2023, **652**, 119038.
233 C. Ye, Y. Zhang, A. Ding, Y. Hu and H. Guo, *Sci. Rep.*, 2018, **8**, 2205.
234 K. Ohkubo, K. Sugaa and S. Fukuzumi, *Chem. Commun.*, 2006, 2018–2020.
235 C. Zheng, G. He, X. Xiao, M. Lu, H. Zhong, X. Zuo and J. Nan, *Appl. Catal., B*, 2017, **205**, 201–210.
236 W. Huang, B. C. Ma, H. Lu, R. Li, L. Wang, K. Landfester and K. A. I. Zhang, *ACS Catal.*, 2017, **7**, 5438–5442.
237 J. D. Sitter and A. K. Vannucci, *J. Am. Chem. Soc.*, 2021, **143**, 2938–2943.
238 P. Bai, X. Tong, Y. Gao and P. Guo, *Catal. Sci. Technol.*, 2019, **9**, 5803–5811.
239 Z.-L. Chena and M. H. Huang, *J. Mater. Chem. A*, 2023, **11**, 22198–22205.
240 M. Pavel, C. Anastasescu, R.-N. State, A. Vasile, F. Papa and I. Balint, *Catalysts*, 2023, **13**, 380.
241 Y. Nosaka and A. Y. Nosaka, *Chem. Rev.*, 2017, **117**, 11302–11336.

242 E. Baur and C. Neuweiler, *Helv. Chim. Acta*, 1927, **10**, 901–907.
243 V. Diesen and M. Jonsson, *J. Phys. Chem. C*, 2014, **118**, 10083–10087.
244 H. Bader, V. Sturzenegger and A. J. Hoigne, *Water Res.*, 1988, **22**, 1109–1115.
245 T. Freese, J. T. Meijer, B. L. Feringa and S. B. Beil, *Nat. Catal.*, 2023, **6**, 553–558.
246 Y. Zhao, R. Shi, X. Bian, C. Zhou, Y. Zhao, S. Zhang, F. Wu, G. I. N. Waterhouse, L.-Z. Wu, C.-H. Tung and T. Zhang, *Adv. Sci.*, 2019, **6**, 1802109.
247 P.-W. Huang and M. C. Hatzell, *Nat. Commun.*, 2022, **13**, 7908.
248 A. P. Varghese, B. Neppolian and S. K. Lakhera, *Ind. Eng. Chem. Res.*, 2023, **62**, 12530–12537.
249 K. A. Othman, R. A. Omer, A. A. A. Mohammad and D. A. Safin, *J. Chem. Educ.*, 2024, **101**, 567–577.
250 R. Capelle, *Anal. Chim. Acta*, 1961, **24**, 555–572.
251 I. Alcón, R. Santiago, J. Ribas-Arino, M. Deumal, I. d. P. R. Moreira and S. T. Bromley, *Nat. Commun.*, 2021, **12**, 1705.
252 S. Thomas, H. Li, C. Zhong, M. Matsumoto, W. R. Dichtel and J.-L. Bredas, *Chem. Mater.*, 2019, **31**, 3051–3065.
253 E. Dautzenberg, M. Lam, T. Nikolaeva, W. M. J. Franssen, B. van Lagen, I. P. A. M. Gerrits-Benneheij, N. Kosinov, G. Li and L. C. P. M. de Smet, *J. Phys. Chem. C*, 2022, **126**, 21338–21347.
254 M. Deng, J. Sun, A. Laemont, C. Liu, L. Wang, L. Bourda, J. Chakraborty, K. V. Hecke, R. Morent, N. De Geyter, K. Leus, H. Chen and P. Van Der Voort, *Green Chem.*, 2023, **25**, 3069–3076.
255 Q. Lin, Y. Yusran, J. Xing, Y. Li, J. Zhang, T. Su, L. Yang, J. Suo, L. Zhang, Q. Li, H. Wang, Q. Fang, Z.-T. Li and D.-W. Zhang, *ACS Appl. Mater. Interfaces*, 2024, **16**, 5869–5880.
256 N. Singh, D. Yadav, S. V. Mulay, J. Y. Kim, N.-J. Park and J.-O. Baeg, *ACS Appl. Mater. Interfaces*, 2021, **13**, 14122–14131.
257 Y. Chen, X. Luo, J. Zhang, L. Hu, T. Xu, W. Li, L. Chen, M. Shen, S.-B. Ren, D.-M. Han, G.-H. Ning and D. Li, *J. Mater. Chem. A*, 2022, **10**, 24620–24627.
258 X.-R. Chen, W.-R. Cui, R.-P. Liang, C.-R. Zhang, R.-H. Xu, W. Jiang and J.-D. Qiu, *ACS Appl. Bio Mater.*, 2021, **4**, 6502–6511.
259 Z. Li, T. Deng, S. Ma, Z. Zhang, G. Wu, J. Wang, Q. Li, H. Xia, S.-W. Yang and X. Liu, *J. Am. Chem. Soc.*, 2023, **145**, 8364–8374.
260 G.-B. Wang, H.-P. Xu, K.-H. Xie, J.-L. Kan, J. Fan, Y.-J. Wang, Y. Geng and Y.-B. Dong, *J. Mater. Chem. A*, 2023, **11**, 4007–4012.
261 A. Das, Mohit and K. R. J. Thomas, *J. Org. Chem.*, 2023, **88**, 14065–14077.
262 R. Liu, Y. Chen, H. Yu, M. Položij, Y. Guo, T. C. Sum, T. Heine and D. Jiang, *Nat. Catal.*, 2024, **7**, 195–206.
263 J. Yang, S. Ghosh, J. Roeser, A. Acharjya, C. Penschke, Y. Tsutsui, J. Rabeah, T. Wang, S. Y. D. Tameu, M.-Y. Ye, J. Grüneberg, S. Li, C. Li, R. Schomäcker, R. Van De Krol, S. Seki, P. Saalfrank and A. Thomas, *Nat. Commun.*, 2022, **13**, 6317.
264 C. Michelin and N. Hoffmann, *ACS Catal.*, 2018, **8**, 12046–12055.
265 X. Tong, S. Gan, J. Wu, Y. Hu and A. Yuan, *Nanoscale*, 2020, **12**, 7376–7382.
266 C. Yang, H. Hu, C. Qian and Y. Liao, *J. Mater. Chem. A*, 2023, **11**, 25899–25909.
267 S.-Y. Ding, P.-L. Wang, G.-L. Yin, X. Zhang and G. Lu, *Int. J. Hydrogen Energy*, 2019, **44**, 11872–11876.
268 Q.-J. Wu, D.-H. Si, S. Ye, Y.-L. Dong, R. Cao and Y.-B. Huang, *J. Am. Chem. Soc.*, 2023, **145**, 19856–19865.
269 Y.-Q. Xing and S.-Y. Liu, *Chin. J. Struct. Chem.*, 2022, **41**, 2209056–2209068.
270 C. Hu, Z. Zhang, S. Liu, X. Liu and M. Pang, *ACS Appl. Mater. Interfaces*, 2019, **11**, 23072–23082.
271 C. Hu, L. Cai, S. Liu and M. Pang, *Chem. Commun.*, 2019, **55**, 9164–9167.
272 L. Li, W. Fang, P. Zhang, J. Bi, Y. He, J. Wang and W. Su, *J. Mater. Chem. A*, 2016, **4**, 12402–12406.
273 Y. He, J. Zhao, Y.-T. Sham, S. Gao, M. Pan, Q. Chen, G. Huang, P. K. Wong and J. Bi, *ACS Sustainable Chem. Eng.*, 2023, **11**, 17552–17563.
274 Y.-P. Zhang, H.-L. Tang, H. Dong, M.-Y. Gao, C.-C. Li, X.-J. Sun, J.-Z. Wei, Y. Qu, Z.-J. Li and F.-M. Zhang, *J. Mater. Chem. A*, 2020, **8**, 4334–4340.
275 Y. Zhang, Y. Hu, J. Zhao, E. Park, Y. Jin, Q. Liu and W. Zhang, *J. Mater. Chem. A*, 2019, **7**, 16364–16371.
276 P. Sarkar, I. H. Chowdhury, A. Chakraborty, M. Goswami, M. K. Naskar, A. Khan and S. M. Islam, *Ind. Eng. Chem. Res.*, 2024, **63**, 5591–5607.
277 Z. Liang, R. Shen, P. Zhang, Y. Li, N. Li and X. Li, *Chin. J. Catal.*, 2022, **43**, 2581–2591.
278 D. Lin, P. Duan, W. Yang, X. Huang, Y. Zhao, C. Wang and Q. Pan, *Chem. Eng. J.*, 2022, **430**, 132817.
279 Y.-N. Gong, J.-H. Mei, W.-J. Shi, J.-W. Liu, D.-C. Zhong and T.-B. Lu, *Angew. Chem., Int. Ed.*, 2024, **63**, e202318735.
280 H. Xue, Z. Bi, J. Cheng, S. Xiong and Y. Wang, *Ind. Eng. Chem. Res.*, 2021, **60**, 8687–8695.
281 Y. Peng, M. Zhao, B. Chen, Z. Zhang, Y. Huang, F. Dai, Z. Lai, X. Cui, C. Tan and H. Zhang, *Adv. Mater.*, 2018, **30**, 1705454.
282 D. Sun and D.-P. Kim, *ACS Appl. Mater. Interfaces*, 2020, **12**, 20589–20595.
283 M.-Y. Zhang, J.-K. Li, R. Wang, S.-N. Zhao, S.-Q. Zang and T. C. W. Mak, *Adv. Sci.*, 2021, **8**, 2101884.
284 G. Yuan, L. Tan, P. Wang, S. Feng, H. Tang, G. Wang, C. Wang and H. Yan, *Mater. Lett.*, 2022, **325**, 132863.
285 K. S. Fu, M. R. Allen and R. K. Archibald, *Sustainability*, 2015, **7**, 15284–15301.
286 S. Wang, W. Liao, H. Su, S. Pang, C. Yang, Y. Fu and Y. Zhang, *Energy Fuels*, 2023, **37**, 1633–1656.
287 K. C. Christoforidis and P. Fornasiero, *ChemCatChem*, 2017, **9**, 1523–1544.

288 R. S. Sprick, J. X. Jiang, B. Bonillo, S. Ren, T. Ratvijitvech, P. Guiglion, M. A. Zwijnenburg, D. J. Adams and A. I. Cooper, *J. Am. Chem. Soc.*, 2015, **137**, 3265–3270.
289 C. Gao, X. Zhang, M. Zhang, X. Wu, R. Chen, C. Zhang, C. Sun, Y. Du, Q. H. Xu and B. Hu, *ACS Appl. Energy Mater.*, 2023, **6**, 9427–9433.
290 Y. Xiao, K. Wang, W. Dong and L. Li, *Polymer*, 2024, **300**, 126980.
291 W. Dong, Y. Xiao, Z. Qin, B. Qiao and L. Li, *J. Mater. Chem. A*, 2023, **11**, 14760–14767.
292 L. Hao, R. Shen, C. Qin, N. Li, H. Hu, G. Liang and X. Li, *Sci. China Mater.*, 2024, **67**, 504–513.
293 S. Wang, T. Wu, S. Wu, J. Guo, T. He, Y. Wu, W. Yuan, Z. Zhang, Y. Hua and Y. Zhao, *Angew. Chem., Int. Ed.*, 2023, **62**, e202311082.
294 J. X. Guo, Z. Y. Wang, C. Q. Han, S. Sun, L. Wang, G. Lu and X. Y. Liu, *J. Mater. Chem. C*, 2024, **12**, 7741–7747.
295 X. Ren, M. Wen, X. Hou, J. Sun, F. Bai and Y. Li, *Chem. Commun.*, 2024, **60**, 4423–4426.
296 S. Li, R. Ma, S. Xu, T. Zheng, G. Fu, Y. Wu, Z. Liao, Y. Kuang, Y. Hou, D. Wang, P. S. Petkov, K. Simeonova, X. Feng, L. Z. Wu, X. B. Li and T. Zhang, *J. Am. Chem. Soc.*, 2022, **144**, 13953–13960.
297 Y. Zhong, W. Dong, S. Ren and L. Li, *Adv. Mater.*, 2024, **36**, 2308251.
298 H. He, R. Shen, P. Zhang, G. Liang and X. Li, *J. Mater. Chem. A*, 2023, **12**, 227–232.
299 G. Fu, D. Yang, S. Xu, S. Li, Y. Zhao, H. Yang, D. Wu, P. S. Petkov, Z. A. Lan, X. Wang and T. Zhang, *J. Am. Chem. Soc.*, 2024, **146**, 1318–1325.
300 L. Stegbauer, K. Schwinghammer and B. V. Lotsch, *Chem. Sci.*, 2014, **5**, 2789–2793.
301 J. Zhang, X. Chen, K. Takanabe, K. Maeda, K. Domen, J. D. Epping, X. Fu, M. Antonietti and X. Wang, *Angew. Chem., Int. Ed.*, 2010, **49**, 441–444.
302 Q. Gao, L. Bai, X. Zhang, P. Wang, P. Li, Y. Zeng, R. Zou and Y. Zhao, *Chin. J. Chem.*, 2015, **33**, 90–94.
303 R. Gomes and A. Bhaumik, *RSC Adv.*, 2016, **6**, 28047–28054.
304 W. Weng and J. Guo, *Nat. Commun.*, 2022, **13**, 5768.
305 R. Chen, Y. Wang, Y. Ma, A. Mal, X. Y. Gao, L. Gao, L. Qiao, X. B. Li, L. Z. Wu and C. Wang, *Nat. Commun.*, 2021, **12**, 1354.
306 Z. Li, T. Deng, S. Ma, Z. Zhang, G. Wu, J. Wang, Q. Li, H. Xia, S. W. Yang and X. Liu, *J. Am. Chem. Soc.*, 2023, **145**, 8364–8374.
307 G. B. Wang, H. P. Xu, K. H. Xie, J. L. Kan, J. Fan, Y. J. Wang, Y. Geng and Y. B. Dong, *J. Mater. Chem. A*, 2023, **11**, 4007–4012.
308 S. Ghosh, H. Küçükkeçeci, R. P. Paitandi, V. Weigelt, V. Dippold, S. Seki and A. Thomas, *J. Mater. Chem. A*, 2023, **12**, 247–255.
309 S. Ghosh, Y. Tsutsui, T. Kawaguchi, W. Matsuda, S. Nagano, K. Suzuki, H. Kaji and S. Seki, *Chem. Mater.*, 2022, **34**, 736–745.
310 Y. Wang, Z. Qiao, H. Li, R. Zhang, Z. Xiang, D. Cao and S. Wang, *Angew. Chem., Int. Ed.*, 2024, **63**, e202404726.
311 S. Wang, L. Da, J. Hao, J. Li, M. Wang, Y. Huang, Z. Li, Z. Liu and D. Cao, *Angew. Chem., Int. Ed.*, 2021, **60**, 9321–9325.
312 J. W. Tang, J. R. Durrant and D. R. Klug, *J. Am. Chem. Soc.*, 2008, **130**, 13885–13891.
313 R. Matheu, P. Garrido-Barros, M. Gil-Sepulcre, M. Z. Ertem, X. Sala, C. Gimbert-Suriñach and A. Llobet, *Nat. Rev. Chem.*, 2019, **3**, 331–341.
314 B. M. Hunter, H. B. Gray and A. M. Müller, *Chem. Rev.*, 2016, **116**, 14120–14136.
315 H. Chen, A. M. Gardner, G. Lin, W. Zhao, X. Wang, M. Bahri, N. D. Browning, X. Xu and X. Li, *J. Phys. Chem. C*, 2023, **127**, 14137–14145.
316 Z. Xiong, B. Sun, H. Zou, R. Wang, Q. Fang, Z. Zhang and S. Qiu, *J. Am. Chem. Soc.*, 2022, **144**, 6583–6593.
317 A. Giri, Y. Khakre, G. Shreeraj, T. K. Dutta, S. Kundu and A. Patra, *J. Mater. Chem. A*, 2022, **10**, 17077–17121.
318 S. Karak, V. Stepanenko, M. A. Addicoat, P. Keßler, S. Moser, F. Beuerle and F. Würthner, *J. Am. Chem. Soc.*, 2022, **144**, 17661–17670.
319 D. L. Ashford, B. D. Sherman, R. A. Binstead, J. L. Templeton and T. J. Meyer, *Angew. Chem., Int. Ed.*, 2015, **54**, 4778–4781.
320 F. Li, K. Fan, L. Wang, Q. Daniel, L. Duan and L. Sun, *ACS Catal.*, 2015, **5**, 3786–3790.
321 R. A. Borse, Y. X. Tan, J. Lin, E. Zhou, Y. Hui, D. Yuan and Y. Wang, *Angew. Chem., Int. Ed.*, 2024, **63**, e202318136.
322 W. Lin, J. Lin, X. Zhang, L. L. Zhang, R. A. Borse and Y. B. Wang, *J. Am. Chem. Soc.*, 2023, **145**, 18141–18147.
323 X. Yan, S. Lyu, X. Q. Xu, W. Chen, P. Shang, Z. Yang, G. Zhang, W. Chen, Y. Wang and L. Chen, *Angew. Chem., Int. Ed.*, 2022, **61**, e202201900.
324 X. Li, Q. Yang, Y. Yuan, Y. Shama and H. Yan, *Small*, 2024, 2401168.
325 E. Zhou, X. Zhang, L. Zhu, E. Chai, J. Chen, J. Li, D. Yuan, L. Kang, Q. Sun and Y. Wang, *Sci. Adv.*, 2024, **10**, eadk8564.
326 S. Chen, T. Takata and K. Domen, *Nat. Rev. Mater.*, 2017, **2**, 17050.
327 S. Nishioka, F. E. Osterloh, X. Wang, T. E. Mallouk and K. Maeda, *Nat. Rev. Methods Primers*, 2023, **3**, 42.
328 Z. Li, C. Liu, Q. Deng and W. Deng, *Adv. Funct. Mater.*, 2024, 2402676.
329 W. Chen, L. Wang, D. Mo, F. He, Z. Wen, X. Wu, H. Xu and L. Chen, *Angew. Chem., Int. Ed.*, 2020, **59**, 16902–16909.
330 W.-K. Han, W. Yuan, Z.-G. Gu and Y. Zhao, *ACS Mater. Lett.*, 2024, **6**, 2276–2294.
331 R. Shen, C. Qin, L. Hao, X. Li, P. Zhang and X. Li, *Adv. Mater.*, 2023, **35**, 2305397.
332 Y. Yang, X. Chu, H. Y. Zhang, R. Zhang, Y. H. Liu, F. M. Zhang, M. Lu, Z. Di Yang and Y. Lan, *Nat. Commun.*, 2023, **14**, 593.
333 J. Cheng, Y. Wu, W. Zhang, J. Zhang, L. Wang, M. Zhou, F. Fan, X. Wu and H. Xu, *Adv. Mater.*, 2024, **36**, 2305313.
334 M. W. Jones, G. P. Peters, T. Gasser, R. M. Andrew, C. Schwingshackl, J. Gütschow, R. A. Houghton,

P. Friedlingstein, J. Pongratz and C. Le Quéré, *Sci. Data*, 2023, **10**, 155.
335 A. L. Burrell, J. P. Evans and M. G. De Kauwe, *Nat. Commun.*, 2020, **11**, 3853.
336 G. AL-khulaidi, Y. Sun, A. G. Alareqi, A.-W. Ibrahim, A. Magaji and X. Zhang, *Energy Fuels*, 2024, **38**, 8355–8384.
337 B. Dutcher, M. Fan and A. G. Russell, *ACS Appl. Mater. Interfaces*, 2015, **7**, 2137–2148.
338 A. Babin, C. Vaneeckhaute and M. C. Iliuta, *Biomass Bioenergy*, 2021, **146**, 105968.
339 J. Lv, J. Xie, A. G. A. Mohamed, X. Zhang, Y. Feng, L. Jiao, E. Zhou, D. Yuan and Y. Wang, *Nat. Rev. Chem.*, 2022, **7**, 91–105.
340 H. Li, A. Dilipkumar, S. Abubakar and D. Zhao, *Chem. Soc. Rev.*, 2023, **52**, 6294–6329.
341 H. Lin, Y. Liu, Z. Wang, L. Ling, H. Huang, Q. Li, L. Cheng, Y. Li, J. Zhou, K. Wu, J. Zhang and T. Zhou, *Angew. Chem., Int. Ed.*, 2022, **61**, e202214142.
342 W. Zhou, X. Wang, W. Zhao, N. Lu, D. Cong, Z. Li, P. Han, G. Ren, L. Sun, C. Liu and W.-Q. Deng, *Nat. Commun.*, 2023, **14**, 6971.
343 T. Skorjanc, D. Shetty, M. E. Mahmoud, F. Gandara, J. I. Martinez, A. K. Mohammed, S. Boutros, A. Merhi, E. O. Shehayeb, C. A. Sharabati, P. Damacet, J. Raya, S. Gardonio, M. Hmadeh, B. R. Kaafarani and A. Trabolsi, *ACS Appl. Mater. Interfaces*, 2022, **14**, 2015–2022.
344 Y.-N. Gong, W. Zhong, Y. Li, Y. Qiu, L. Zheng, J. Jiang and H.-L. Jiang, *J. Am. Chem. Soc.*, 2020, **142**, 16723–16731.
345 S. Yang, W. Hu, X. Zhang, P. He, B. Pattengale, C. Liu, M. Cendejas, I. Hermans, X. Zhang, J. Zhang and J. Huang, *J. Am. Chem. Soc.*, 2018, **140**, 14614–14618.
346 Q. Pan, M. Abdellah, Y. Cao, W. Lin, Y. Liu, J. Meng, Q. Zhou, Q. Zhao, X. Yan, Z. Li, H. Cui, H. Cao, W. Fang, D. A. Tanner, M. Abdel-Hafiez, Y. Zhou, T. Pullerits, S. E. Canton, H. Xu and K. Zheng, *Nat. Commun.*, 2022, **13**, 845.
347 Q. Zhang, S. Gao, Y. Guo, H. Wang, J. Wei, X. Su, H. Zhang, Z. Liu and J. Wang, *Nat. Commun.*, 2023, **14**, 1147.
348 Z. Fu, X. Wang, A. M. Gardner, X. Wang, S. Y. Chong, G. Neri, A. J. Cowan, L. Liu, X. Li, A. Vogel, R. Clowes, M. Bilton, L. Chen, R. S. Sprick and A. I. Cooper, *Chem. Sci.*, 2020, **11**, 543–550.
349 P. Sarkar, A. Hazra Chowdhury, S. Riyajuddin, S. Ghosh and S. M. Islam, *React. Chem. Eng.*, 2023, **8**, 365–376.
350 Y. Lan, W. Yan, N. Yang, G. Wang, Y. Bi, C. Tian, H. Liu and X. Zhu, *Small*, 2023, **19**, 2208118.
351 K. Lei, D. Wang, L. Ye, M. Kou, Y. Deng, Z. Ma, L. Wang and Y. Kong, *ChemSusChem*, 2020, **13**, 1725–1729.
352 Y. Fu, X. Zhu, L. Huang, X. Zhang, F. Zhang and W. Zhu, *Appl. Catal., B*, 2018, **239**, 46–51.
353 J. X. Cui, L. J. Wang, L. Feng, B. Meng, Z. Y. Zhou, Z. M. Su, K. Wang and S. Liu, *J. Mater. Chem. A*, 2021, **9**, 24895–24902.
354 S. Kandambeth, A. Mallick, B. Lukose, M. V. Mane, R. Banerjee and T. Heine, *J. Am. Chem. Soc.*, 2012, **134**, 19524–19527.
355 J. Zhou, W. C. Chen, C. Y. Sun, L. Han, C. Qin, M. M. Chen, M. X. L. Wang, E. B. Wang and Z. M. Su, *J. Mater. Chem. A*, 2018, **6**, 21596–21604.
356 X. Yu, K. Gong, S. Tian, G. Gao, J. Xie and X. Jin, *J. Mater. Chem. A*, 2023, **11**, 5627–5635.
357 Z. Shan, M. Wu, D. Zhu, X. Wu, K. Zhang, R. Verduzco and G. Zhang, *J. Am. Chem. Soc.*, 2022, **144**, 5728–5733.
358 G. Goor, J. Glenneberg and S. Jacobi, *Ullmann's Encyclopedia of Industrial Chemistry*, Wiley-VCH, Weinheim, 7th edn, 2012, pp. 393–427.
359 L. Xie, X. Wang, Z. Zhang, Y. Ma, T. Du, R. Wang and J. Wang, *Small*, 2023, **19**, 2301007.
360 W. Chu, W. Wang, Y. Deng and C. Peng, *Environ. Sci.: Water Res. Technol.*, 2022, **8**, 2819–2842.
361 Q. Miao, M. Liu, Y.-Y. Mou, Y.-F. Zhang, Q. Li, Z.-J. Cao and W. Jiang, *ACS Sustainable Chem. Eng.*, 2024, **12**, 5596–5607.
362 T. Liu, Z. Pan, J. J. M. Vequizo, K. Kato, B. Wu, A. Yamakata, K. Katayama, B. Chen, C. Chu and K. Domen, *Nat. Commun.*, 2022, **13**, 1034.
363 Z. Yong and T. Ma, *Angew. Chem., Int. Ed.*, 2023, **62**, e202308980.
364 C. Krishnaraj, H. S. Jena, L. Bourda, A. Laemont, P. Pachfule, J. Roeser, C. V. Chandran, S. Borgmans, S. M. J. Rogge, K. Leus, C. V. Stevens, J. A. Martens, V. Van Speybroeck, E. Breynaert, A. Thomas and P. Van Der Voort, *J. Am. Chem. Soc.*, 2020, **142**, 20107–20116.
365 J. Sun, H. S. Jena, C. Krishnaraj, K. S. Rawat, S. Abednatanzi, J. Chakraborty, A. Laemont, W. Liu, H. Chen, Y.-Y. Liu, K. Leus, H. Vrielinck, V. Van Speybroeck and P. Van Der Voort, *Angew. Chem., Int. Ed.*, 2023, **62**, e202216719.
366 C. Qin, X. Wu, L. Tang, X. Chen, M. Li, Y. Mou, B. Su, S. Wang, C. Feng, J. Liu, X. Yuan, Y. Zhao and H. Wang, *Nat. Commun.*, 2023, **14**, 5238.
367 F. Liu, P. Zhou, Y. Hou, H. Tan, Y. Liang, J. Liang, Q. Zhang, S. Guo, M. Tong and J. Ni, *Nat. Commun.*, 2023, **14**, 4344.
368 Z. Zhou, M. Sun, Y. Zhu, P. Li, Y. Zhang, M. Wang and Y. Shen, *Appl. Catal., B*, 2023, **334**, 122862.
369 E. Zhou, F. Wang, X. Zhang, Y. Hui and Y. Wang, *Angew. Chem., Int. Ed.*, 2024, **63**, e202400999.
370 J.-P. Liao, M. Zhang, P. Huang, L.-Z. Dong, T.-T. Ma, G.-Z. Huang, Y.-F. Liu, M. Lu, S.-L. Li and Y.-Q. Lan, *ACS Catal.*, 2024, **14**, 3778–3787.
371 P. Li, H. Zhao, R. Ji, W. Chi, X. Sun, Y. Dong and Y. Zhu, *Catal. Sci. Technol.*, 2024, **14**, 2470–2478.
372 H. Yu, F. Zhang, Q. Chen, P.-K. Zhou, W. Xing, S. Wang, G. Zhang, Y. Jiang and X. Chen, *Angew. Chem., Int. Ed.*, 2024, **63**, e202402297.
373 T. Yang, D. Zhang, A. Kong, Y. Zou, L. Yuan, C. Liu, S. Luo, G. Wei and C. Yu, *Angew. Chem., Int. Ed.*, 2024, **63**, e202404077.

374 T. Xu, Z. Wang, W. Zhang, S. An, L. Wei, S. Guo, Y. Huang, S. Jiang, M. Zhu, Y.-B. Zhang and W.-H. Zhu, *J. Am. Chem. Soc.*, 2024, **146**, 20107–20115.
375 K. A. Scott, P. B. Cox and J. T. Njardarson, *J. Med. Chem.*, 2022, **65**, 7044–7072.
376 F. Shahidi and C.-T. Ho, *Phenolic Compounds in Foods and Natural Health Products*, ACS Symposium Series, American Chemical Society, Washington, DC, 2005.
377 Y.-Q. Zou, J.-R. Chen, X.-P. Liu, L.-Q. Lu, R. L. Davis, K. A. Jørgensen and W.-J. Xiao, *Angew. Chem., Int. Ed.*, 2012, **51**, 784–788.
378 D. A. Nicewicz and T. M. Nguyen, *ACS Catal.*, 2014, **4**, 355–360.
379 J. A. Johnson, J. Luo, X. Zhang, Y.-S. Chen, M. D. Morton, E. Echeverría, F. E. Torres and J. Zhang, *ACS Catal.*, 2015, **5**, 5283–5291.
380 H.-P. Liang, Q. Chen and B.-H. Han, *ACS Catal.*, 2018, **8**, 5313–5322.
381 M. H. Muhammad, X.-L. Chen, Y. Liu, T. Shi, Y. Peng, L. Qu and B. Yu, *ACS Sustainable Chem. Eng.*, 2020, **8**, 2682–2687.
382 S. Bi, P. Thiruvengadam, S. Wei, W. Zhang, F. Zhang, L. Gao, J. Xu, D. Wu, J.-S. Chen and F. Zhang, *J. Am. Chem. Soc.*, 2020, **142**, 11893–11900.
383 Y. Qian, D. Li, Y. Han and H.-L. Jiang, *J. Am. Chem. Soc.*, 2020, **142**, 20763–20771.
384 R. Paul, S. C. Shit, H. Mandal, J. Rabeah, S. S. Kashyap, Y. Nailwal, D. B. Shinde, Z. Lai and J. Mondal, *ACS Appl. Nano Mater.*, 2021, **4**, 11732–11742.
385 G. Xiao, W. Li, T. Chen, W.-B. Hu, H. Yang, Y. A. Liu and K. Wen, *Eur. J. Org. Chem.*, 2021, 3986–3991.
386 B. Luo, Y. Zhang, Y. Chen and J. Huo, *Mater. Adv.*, 2022, **3**, 4699–4706.
387 K. Verma, M. A. Addicoat and K. R. J. Thomas, *ACS Appl. Polym. Mater.*, 2024, **6**, 3909–3917.
388 A. Zadehnazari, A. Khosropour, A. A. Altaf, A. S. Rosen and A. Abbaspourrad, *Adv. Mater.*, 2024, **36**, 2311042.
389 A. S. Surur, L. Schulig and A. Link, *Arch. Pharm. Chem. Life Sci.*, 2019, **352**, e1800248.
390 E. Wojaczyńska and J. Wojaczyńsk, *Curr. Opin. Chem. Biol.*, 2023, **76**, 102340.
391 X. Yu, Y. Liu, Y. Li and Q. Wang, *J. Agric. Food Chem.*, 2016, **64**, 3034–3040.
392 P. Li, L. Wang and X. Wang, *J. Heterocycl. Chem.*, 2021, **58**, 28–39.
393 B. Smolkin, N. Levi, N. Karton-Lifshin, L. Yehezkel, Y. Zafrani and I. Columbus, *J. Org. Chem.*, 2018, **83**, 13949–13955.
394 S. Zhao, Y. Zhu, H. Xi, M. Han, D. Li, Y. Li and H. Zhao, *J. Environ. Chem. Eng.*, 2020, **8**, 104221.
395 B. Tanriover, S. M. S. Subasinghe and N. P. Mankad, *ACS Catal.*, 2024, **14**, 9323–9327.
396 F. Lina, Y. Zhang, L. Wang, Y. Zhang, D. Wang, M. Yang, J. Yang, B. Zhang, Z. Jiang and C. Li, *Appl. Catal., B*, 2012, **127**, 363–370.
397 H. Wang, G. W. Wagner, A. X. Lu, D. L. Nguyen, J. H. Buchanan, P. M. McNutt and C. J. Karwacki, *ACS Appl. Mater. Interfaces*, 2018, **10**, 18771–18777.
398 A. Samokhvalov, *ChemPhysChem*, 2011, **12**, 2870–2885.
399 Q. Li, X. Lan, G. An, L. Ricardez-Sandoval, Z. Wang and G. Bai, *ACS Catal.*, 2020, **10**, 6664–6675.
400 X. Wang, S. Zhang, X. Li, Z. Zhan, B. Tan, X. Lang and S. Jin, *J. Mater. Chem. A*, 2021, **9**, 16405–16410.
401 Y. Li, T.-X. Luan, K. Cheng, D. Zhang, W. Fan, P.-Z. Li and Y. Zhao, *ACS Mater. Lett.*, 2022, **4**, 1160–1167.
402 X. Kan, J.-C. Wang, Z. Chen, J.-Q. Du, J.-L. Kan, W.-Y. Li and Y.-B. Dong, *J. Am. Chem. Soc.*, 2022, **144**, 6681–6686.
403 M. Xu, J. Zhang, L. Liu, X. Cheng, J. Hu, Y. Sha, Z. Su and Y. Wang, *Chem. Commun.*, 2022, **58**, 6324–6327.
404 Y. Wang, F. Huang, W. Sheng, X. Miao, X. Li, X.-K. Gu and X. Lang, *Appl. Catal., B*, 2023, **338**, 123070.
405 F. Zhang, Y. Wang, H. Zhao, X. Dong, X.-K. Gu and X. Lang, *ACS Appl. Mater. Interfaces*, 2024, **16**, 8772–8782.
406 Y. Chen, J. Zhang, M. Zhang and X. Wang, *Chem. Sci.*, 2013, **4**, 3244–3248.
407 C. Parmeggiani and F. Cardona, *Green Chem.*, 2012, **14**, 547–564.
408 T. Mallat and A. Baiker, *Chem. Rev.*, 2004, **104**, 3037–3058.
409 Z. Guo, B. Liu, Q. Zhang, W. Deng, Y. Wang and Y. Yang, *Chem. Soc. Rev.*, 2014, **43**, 3480–3524.
410 Z. Shen, Y. Hu, B. Li, Y. Zou, S. Li, G. W. Busser, X. Wang, G. Zhao and M. Muhler, *J. Energy Chem.*, 2021, **62**, 338–350.
411 G. Lu, X. Huang, Y. Li, G. Zhao, G. Pang and G. Wang, *J. Energy Chem.*, 2020, **43**, 8–15.
412 S. Trenker, L. Grunenberg, T. Banerjee, G. Savasci, L. M. Poller, K. I. M. Muggli, F. Haase, C. Ochsenfeld and B. V. Lotsch, *Chem. Sci.*, 2021, **12**, 15143–15150.
413 L. Liao, D. Ditz, F. Zeng, M. Alves Favaro, A. Iemhoff, K. Gupta, H. Hartmann, C. Szczuka, P. Jakes, P. J. C. Hausoul, J. Artz and R. Palkovits, *ChemistrySelect*, 2020, **5**, 14438–14446.
414 P. L. Wang, S. Y. Ding, Z. C. Zhang, Z. P. Wang and W. Wang, *J. Am. Chem. Soc.*, 2019, **141**, 18004–18008.
415 K. Zhang, G. Lu, Z. Xi, Y. Li, Q. Luan and X. Huang, *Chin. Chem. Lett.*, 2021, **32**, 2207–2211.
416 H. Dai, H. Li and Q. Yang, *Microporous Mesoporous Mater.*, 2022, **342**, 112121.
417 H. Li, H. Liu, C. Li, J. Liu, J. Liu and Q. Yang, *J. Mater. Chem. A*, 2020, **8**, 18745–18754.
418 S. Murahashi, *Angew. Chem., Int. Ed. Engl.*, 1995, **34**, 2443–2465.
419 M. Damaceanu, C. Constantin and L. Marin, *Dyes Pigm.*, 2016, **134**, 382–396.
420 K.-i. Yamada and K. Tomioka, *Chem. Rev.*, 2008, **108**, 2874–2886.
421 J.-H. Xie, S.-F. Zhu and Q.-L. Zhou, *Chem. Rev.*, 2011, **111**, 1713–1760.
422 C. S. Marques and A. J. Burke, *ChemCatChem*, 2011, **3**, 635–645.

423 J. Feng, J. Cheng, J. Pang, M. Tang, Z. Liu, C. Rong and R. Tan, *Catal. Sci. Technol.*, 2022, **12**, 6865–6874.
424 S. Li, L. Li, Y. Li, L. Dai, C. Liu, Y. Liu, J. Li, J. Lv, P. Li and B. Wang, *ACS Catal.*, 2020, **10**, 8717–8726.
425 S. Liu, Q. Su, W. Qi, K. Luo, X. Sun, H. Ren and Q. Wu, *Catal. Sci. Technol.*, 2022, **12**, 2837–2845.
426 H. He, X. Fang, D. Zhai, W. Zhou, Y. Li, W. Zhao, C. Liu, Z. Li and W. Deng, *Chem. – Eur. J.*, 2021, **27**, 14390–14395.
427 P. Li, X. Dong, Y. Zhang, X. Lang and C. Wang, *Mater. Today Chem.*, 2022, **25**, 100953.
428 R. Chen, J. L. Shi, Y. Ma, G. Lin, X. Lang and C. Wang, *Angew. Chem., Int. Ed.*, 2019, **58**, 6430–6434.
429 L. Wang, J. Chakraborty, M. Deng, J. Sun and P. Van Der Voort, *ChemCatChem*, 2024, e202400200.
430 S. Wu, Y. F. Zhang, H. Ding, X. Li and X. Lang, *J. Colloid Interface Sci.*, 2022, **610**, 446–454.
431 N. Sun, Y. Jin, H. Wang, B. Yu, R. Wang, H. Wu, W. Zhou and J. Jiang, *Chem. Mater.*, 2022, **34**, 1956–1964.
432 F. Chu, G. Hai, D. Zhao, S. Liu, Y. Hu, G. Zhao, B. Peng, G. Wang and X. Huang, *ACS Catal.*, 2023, **13**, 13167–13180.
433 X. Li, S. Yang, F. Zhang, L. Zheng and X. Lang, *Appl. Catal., B*, 2022, **303**, 120846.
434 K. Xiong, Y. Wang, F. Zhang, X. Li and X. Lang, *Appl. Catal., B*, 2023, **322**, 122135.
435 L. Y. Yin, Y. N. Zhao, Y. M. Xing, H. Q. Tan, Z. L. Lang, W. K. Ho, Y. H. Wang and Y. G. Li, *Chem. Eng. J.*, 2021, **419**, 129984.
436 Y. Fang, Y. Liu, H. Huang, J. Sun, J. Hong, F. Zhang, X. Wei, W. Gao, M. Shao, Y. Guo, Q. Tang and Y. Liu, *Nat. Commun.*, 2024, **15**, 4856.
437 T. Dalton, T. Faber and F. Glorius, *ACS Cent. Sci.*, 2021, **7**, 245–261.
438 K. M. Altus and J. A. Love, *Commun. Chem.*, 2021, **4**, 173.
439 H. M. L. Davies and D. Morton, *J. Org. Chem.*, 2016, **81**, 343–350.
440 B. Chen, L.-Z. Wu and C.-H. Tung, *Acc. Chem. Res.*, 2018, **51**, 2512–2523.
441 D. Mazzarella, G. E. M. Crisenza and P. Melchiorre, *J. Am. Chem. Soc.*, 2018, **140**, 8439–8443.
442 C. L. Baumberger, V. Z. Valley and M. B. Chambers, *Chem. Commun.*, 2024, **60**, 6901–6904.
443 Z. Chai, *Angew. Chem., Int. Ed.*, 2024, **63**, e202316444.
444 M. Tian, S. Liu, X. Bu, J. Yu and X. Yang, *Chem. – Eur. J.*, 2020, **26**, 369–373.
445 K. Cai, W. Wang, J. Zhang, L. Chen, L. Wang, X. Zhu, Z. Yu, Z. Wu and H. Zhou, *J. Mater. Chem. A*, 2022, **10**, 7165–7172.
446 G. Kumara, R. S. Pillaic, N.-u. H. Khan and S. Neogi, *Appl. Catal., B*, 2021, **292**, 120149.
447 B. Ma, X. Yang, J. Yuan, X. Yang, D. Han, K. Zhao, C. Lin, L. Wang, G. Liu and L. Mi, *Appl. Catal., A*, 2023, **666**, 119403.
448 F. Yang, C. Li, C. Xu, J. Kan, B. Tian, H. Qu, Y. Guo, Y. Geng and Y. Dong, *Chem. Commun.*, 2022, **58**, 1530–1533.
449 M. Tian, Y. Wang, X. Bu, Y. Wang and X. Yang, *Catal. Sci. Technol.*, 2021, **11**, 4272–4279.
450 Z. Wang, P. Yeary, Y. Fan and W. Lin, *Chem. Sci.*, 2024, **15**, 4920–4925.
451 X. Kang, X. Wu, X. Han, C. Yuan, Y. Liu and Y. Cui, *Chem. Sci.*, 2020, **11**, 1494–1502.
452 H. Pang, G. Liu, D. Huang, Y. Zhu, X. Zhao, W. Wang and Y. Xiang, *Angew. Chem., Int. Ed.*, 2023, **62**, e202313520.
453 S. Li, W. Wei, K. Chi, C. T. J. Ferguson, Y. Zhao and K. A. I. Zhang, *J. Am. Chem. Soc.*, 2024, **146**, 12386–12394.
454 A. Basak, S. Karak and R. Banerjee, *J. Am. Chem. Soc.*, 2023, **145**, 7592–7599.
455 R. Emadi, A. B. Nekoo, F. Molaverdi, Z. Khorsandi, R. Sheibani and H. Sadeghi-Aliabadi, *RSC Adv.*, 2023, **13**, 18715–18733.
456 J. Bariwal and E. Van der Eycken, *Chem. Soc. Rev.*, 2013, **42**, 9283–9303.
457 P. Ruiz-Castillo and S. L. Buchwald, *Chem. Rev.*, 2016, **116**, 12564–12649.
458 J. Rayadurgam, S. Sana, M. Sasikumar and Q. Gu, *Org. Chem. Front.*, 2021, **8**, 384–414.
459 C.-H. Lim, M. Kudisch, B. Liu and G. M. Miyake, *J. Am. Chem. Soc.*, 2018, **140**, 7667–7673.
460 A. Vijeta, C. Casadevall and E. Reisner, *Angew. Chem., Int. Ed.*, 2022, **61**, e202203176.
461 T. Gandini, L. Dolcini, L. Di Leo, M. Fornara, A. Bossi, M. Penconi, A. Dal Corso, C. Gennari and L. Pignataro, *ChemCatChem*, 2022, **14**, e202200990.
462 J. Li, C.-Y. Huang and C.-J. Li, *Chem*, 2022, **8**, 2419–2431.
463 M. Kuai, Z. Jia, L. Chen, S. Gao and W. Fang, *Eur. J. Org. Chem.*, 2024, e202300933.
464 A. Jati, K. Dey, M. Nurhuda, M. A. Addicoat, R. Banerjee and B. Maji, *J. Am. Chem. Soc.*, 2022, **144**, 7822–7833.
465 M. Traxler, S. Gisbertz, P. Pachfule, J. Schmidt, J. Roeser, S. Reischauer, J. Rabeah, B. Pieber and A. Thomas, *Angew. Chem., Int. Ed.*, 2022, **61**, e202117738.
466 Y.-L. Li, F. Wang, J. J. Vittal, P. Jin, S.-L. Huang and G.-Y. Yang, *J. Mater. Chem. A*, 2024, **12**, 9164–9172.
467 Z. Li, S. Qiu, Y. Song, S. Huang, J. Gao, L. Sun and J. Hou, *Sci. Bull.*, 2022, **67**, 1971–1981.
468 C. Song, T. Yan, X. Cui, H. Chen, R. Ye and X. Zhang, *Appl. Catal., A*, 2023, **661**, 119245.
469 M. Traxler, S. Reischauer, S. Vogl, J. Roeser, J. Rabeah, C. Penschke, P. Saalfrank, B. Pieber and A. Thomas, *Chem. – Eur. J.*, 2023, **29**, e202202967.
470 T. Zhou and M. Szostak, *Catal. Sci. Technol.*, 2020, **10**, 5702–5739.
471 H. Zhang, P. Ruiz-Castillo, A. W. Schuppe and S. L. Buchwald, *Org. Lett.*, 2020, **22**, 5369–5374.
472 H. Zhang, P. Ruiz-Castillo and S. L. Buchwald, *Org. Lett.*, 2018, **20**, 1580–1583.
473 K. Dong, C. Pezzetta, Q.-C. Chen, A. Kaushansky, A. Agosti, G. Bergamini, R. Davidson and L. Amirav, *ChemCatChem*, 2022, **14**, e202200477.

474 H.-C. Hu, Z.-P. Wang, L. Liang, X.-Y. Du, T. Li, J. Feng, T.-T. Xiao, Z.-M. Jin, S.-Y. Ding, Q. Liu, L.-Q. Lu, W.-J. Xiao and W. Wang, *Chem. – Eur. J.*, 2024, **30**, e202303476.
475 W. Dong, Y. Yang, Y. Xiang, S. Wang, P. Wang, J. Hu, L. Rao and H. Chen, *Green Chem.*, 2021, **23**, 5797–5805.
476 Q. Lin, Y. Yusran, J. Xing, Y. Li, J. Zhang, T. Su, L. Yang, J. Suo, L. Zhang, Q. Li, H. Wang, Q. Fang, Z.-T. Li and D.-W. Zhang, *ACS Appl. Mater. Interfaces*, 2024, **16**, 5869–5880.
477 K. Wang, H. Jiang, H. Liu, H. Chen and F. Zhang, *ACS Catal.*, 2022, **12**, 6068–6080.
478 Q. Yang, Y. Zhao and D. Ma, *Org. Process Res. Dev.*, 2022, **26**, 1690–1750.
479 L.-J. Cheng and N. P. Mankad, *Chem. Soc. Rev.*, 2020, **49**, 8036–8064.
480 M. Busch, M. D. Wodrich and C. Corminboeuf, *ACS Catal.*, 2017, **7**, 5643–5653.
481 A. Chen, Y. Han, R. Wu, B. Yang, L. Zhu and F. Zhu, *Nat. Commun.*, 2024, **15**, 5228.
482 J. Khamrai, I. Ghosh, A. Savateev, M. Antonietti and B. König, *ACS Catal.*, 2020, **10**, 3526–3532.
483 X. Zhou, X. Gao, M. Liu, Z. Gao, X. Qin, W. Xu, S. Ye, W. Zhou, H. Fan, J. Li, S. Fan, L. Yang, J. Fu, D. Xiao, L. Lin, D. Ma and S. Yao, *Nat. Commun.*, 2022, **13**, 4379.
484 S. Okumura, T. Takahashi, K. Torii and Y. Uozumi, *Chem. – Eur. J.*, 2023, **29**, e202300840.
485 T. Wan, L. Capaldo, J. Djossou, A. Staffa, F. J. de Zwart, B. de Bruin and T. Noël, *Nat. Commun.*, 2024, **15**, 4028.
486 Y. Yang, H. Niu, W. Zhao, L. Xu, H. Zhang and Y. Cai, *RSC Adv.*, 2020, **10**, 29402–29407.
487 P. Chakrabortty, A. Das, A. H. Chowdhury, S. Ghosh, A. Khan and S. M. Islam, *New J. Chem.*, 2021, **45**, 4738–4745.
488 A. López-Magano, B. Ortín-Rubio, I. Imaz, D. Maspoch, J. Alemán and R. Mas-Ballesté, *ACS Catal.*, 2021, **11**, 12344–12354.
489 A. Jati, S. Dam, S. Kumar, K. Kumar and B. Maji, *Chem. Sci.*, 2023, **14**, 8624–8634.
490 S. Sharma and A. Bhattacharya, *Appl. Water Sci.*, 2017, **7**, 1043–1067.
491 R. Kumar, M. Qureshi, D. K. Vishwakarma, N. Al-Ansari, A. Kuriqi, A. Elbeltagi and A. Saraswat, *Case Stud. Chem. Environ. Eng.*, 2022, **6**, 100219.
492 A. Saravanan, P. S. Kumar, S. Jeevanantham, S. Karishma, B. Tajsabreen, P. R. Yaashikaa and B. Reshma, *Chemosphere*, 2021, **280**, 130595.
493 Water Treatment, **https://www.cdc.gov/healthywater/drinking/public/water_treatment.html**, accessed June 2024.
494 Y. Hou, F. Liu, B. Zhang and M. Tong, *Environ. Sci. Technol.*, 2022, **56**, 16303–16314.
495 S. Ruidas, A. Chowdhury, A. Ghosh, A. Ghosh, S. Mondal, A. D. D. Wonanke, M. Addicoat, A. K. Das, A. Modak and A. Bhaumik, *Langmuir*, 2023, **39**, 4071–4081.
496 X. Li, X. Chen, C. Li, Z. Xu and B. Jiang, *New J. Chem.*, 2023, **47**, 2659–2665.
497 W. Lu, C. Wang, Y. Bai, C. Xie, Z. Zhang, W. Song and J. Wang, *Environ. Sci.: Nano*, 2024, **11**, 229–240.
498 M. Deng, L. Wang, Z. Wen, J. Chakraborty, J. Sun, G. Wang and P. Van Der Voort, *Green Chem.*, 2024, **26**, 3239–3248.
499 X. Ren, M. Wen, X. Hou, J. Sun, F. Bai and Y. Li, *Chem. Commun.*, 2024, **60**, 4423–4426.
500 H. Xu, Y. Xu, Y. Wang, Q. Wang, Y. Zhang, Q. Liao and K. Xi, *ACS Appl. Nano Mater.*, 2024, **7**, 3071–3081.
501 J. H. Wang, A. E. Hassan, A. M. Elewa and A. F. M. El-Mahdy, *J. Mater. Chem. A*, 2024, **12**, 14005–14021.
502 M. Bhadra, S. Kandambeth, M. K. Sahoo, M. Addicoat, E. Balaraman and R. Banerjee, *J. Am. Chem. Soc.*, 2019, **141**, 6152–6156.
503 Y.-X. Chen, M. Zhang, S.-Z. Zhang, Z.-Q. Hao and Z.-H. Zhang, *Green Chem.*, 2022, **24**, 4071–4081.
504 D. Chen, W. Chen, G. Zhang, S. Li, W. Chen, G. Xing and L. Chen, *ACS Catal.*, 2022, **12**, 616–623.
505 T. He, Z. Zhao, R. Liu, X. Liu, B. Ni, Y. Wei, Y. Wu, W. Yuan, H. Peng, Z. Jiang and Y. Zhao, *J. Am. Chem. Soc.*, 2023, **145**, 6057–6066.
506 Y. Liu, X. Jiang, L. Chen, Y. Cui, Q.-Y. Li, X. Zhao, X. Han, Y.-C. Zheng and X.-J. Wang, *J. Mater. Chem. A*, 2023, **11**, 1208–1215.
507 K.-K. Niu, T.-X. Luan, J. Cui, H. Liu, L.-B. Xing and P.-Z. Li, *ACS Catal.*, 2024, **14**, 2631–2641.
508 J.-R. Wang, K. Song, T.-X. Luan, K. Cheng, Q. Wang, Y. Wang, W. W. Yu, P.-Z. Li and Y. Zhao, *Nat. Commun.*, 2024, **15**, 1267.
509 X. Yang, Q. An, X. Li, Y. Fu, S. Yang, M. Liu, Q. Xu and G. Zeng, *Nat. Commun.*, 2024, **15**, 1889.